

DESIGN OF WIRELESS POWER TRANSFER SYSTEM  
FOR THE ELDERLY ELECTRIC VEHICLE



Zheng Junlong

A THESIS SUBMITTED IN PARTIAL FULFILLMENT  
OF THE REQUIREMENT FOR THE DEGREE OF  
DOCTOR OF ENGINEERING IN ELECTRICAL ENGINEERING  
SCHOOL OF ENGINEERING  
KING MONGKUT'S INSTITUTE OF TECHNOLOGY LADKRABANG  
2024  
KMITL-2024-EN-D-018-192

This material is reserved for educational use only, not allowed for commercial use.

Forbidden to modify the content, and cite the document when use.



**COPYRIGHT 2024**

**SCHOOL OF ENGINEERING**

**KING MONGKUT'S INSTITUTE OF TECHNOLOGY LADKRABANG**

This material is reserved for educational use only, not allowed for commercial use.

Forbidden to modify the content, and cite the document when use.

Thesis Title DESIGN OF WIRELESS POWER TRANSFER  
SYSTEM FOR THE ELDERLY ELECTRIC VEHICLE  
Student Zheng Junlong  
Student ID. 63601014  
Degree Doctor of Engineering  
Program Electrical Engineering  
Year 2024  
Thesis Advisor Assoc.Prof.Dr. Chaiyan Jettanasen

### ABSTRACT IN THAI

งานวิจัยปริญญาเอกนี้ เน้นการออกแบบระบบถ่ายโอนพลังงานแบบไร้สาย (WPT) พร้อมอุปกรณ์จัดตำแหน่งอัตโนมัติ (AAD) สำหรับยานยนต์ไฟฟ้า (EV) ที่ใช้สำหรับผู้สูงอายุเป็นหลัก ในการศึกษาและออกแบบ เริ่มต้นด้วยสูตรสำหรับการคำนวณโดยละเอียดและการวิเคราะห์เกี่ยวกับพารามิเตอร์กำลัง พารามิเตอร์พื้นฐานของมอเตอร์ขับเคลื่อน และความจุของแบตเตอรี่กำลังของรถยนต์ไฟฟ้าสำหรับผู้สูงอายุ จากนั้นได้ทำการวิเคราะห์โดยละเอียดเกี่ยวกับการวิเคราะห์สนามแม่เหล็กของระบบ WPT สำหรับรถยนต์ไฟฟ้าของผู้สูงอายุ ในเวลาเดียวกัน เมื่อตำแหน่งสัมพัทธ์ของคอยล์ส่งและคอยล์รับใน WPT เปลี่ยนแปลง เราก็ได้ทำการคำนวณและวิเคราะห์โดยละเอียดตามขนาดและการกระจายของค่าสัมประสิทธิ์การเหนี่ยวนำร่วมระหว่างคอยล์ทั้งสอง เพื่อให้บรรลุการจัดตำแหน่งอัตโนมัติระหว่างคอยล์ส่งและคอยล์รับใน WPT และเพื่อให้ได้ประสิทธิภาพการส่งผ่านพลังงานที่ดีที่สุด โดยในงานวิจัยนี้ได้เสนออัลกอริธึมการปรับให้เหมาะสมใหม่ชื่อ Maritime Search and Rescue Algorithm (MSRA) ซึ่งอัลกอริธึมนี้ไม่เพียงแต่มีประสิทธิภาพในการเพิ่มประสิทธิภาพที่ดีขึ้นเท่านั้น แต่ยังมีความสามารถในการวางแผนเส้นทางไปยังไซต์ที่ดีที่สุดอีกด้วย สำหรับอัลกอริธึมการเพิ่มประสิทธิภาพอัจฉริยะอื่นๆ ที่มีอยู่ ไม่เคยพบว่ามีประสิทธิภาพทั้งสองอย่างนี้เลย ยิ่งไปกว่านั้นแบบจำลองทางคณิตศาสตร์ของ MSRA ได้ถูกสร้างขึ้น และสร้างรหัสเทียมของโปรแกรมคอมพิวเตอร์ขึ้น สุดท้ายได้ออกแบบระบบฮาร์ดแวร์และซอฟต์แวร์ทั้งหมดของ WPT-AAD และได้สร้างชุดทดลองเพื่อตรวจสอบการวิเคราะห์ทางทฤษฎีและการออกแบบก่อนหน้านี้นี้ทั้งหมดด้วยการทดลองจริง เพื่อให้บรรลุประสิทธิภาพตามที่กำหนดไว้

**คำสำคัญ :** รถยนต์ไฟฟ้าสำหรับผู้สูงอายุ, ยานพาหนะไฟฟ้า, อัลกอริธึมการค้นหาและช่วยเหลือทางทะเล (MSRA), การถ่ายโอนพลังงานแบบไร้สาย

Thesis Title        DESIGN OF WIRELESS POWER TRANSFER  
                              SYSTEM FOR THE ELDERLY ELECTRIC VEHICLE

Student                Zheng Junlong

Student ID.         63601014

Degree                Doctor of Engineering

Program             Electrical Engineering

Year                  2024

Thesis Advisor     Assoc.Prof. Dr. Chaiyan Jettanasen

### ABSTRACT IN ENGLISH

This research focuses on how to design a wireless power transfer (WPT) system with automatic alignment device (AAD) for an electric vehicle (EV) mainly used for elderly people. To study and design, we started with the formulas for detailed calculations and analysis on the power parameters, basic parameters of the driving motor, and the capacity of the power battery of an elderly EV. Next, we conducted a detailed analysis of the magnetic field analysis of the WPT system for an elderly EV. At the same time, when the relative positions of the transmitting coil and the receiving coil in the WPT change, we have also made detailed calculations and analysis corresponding to the size and distribution of the mutual inductance coefficient between the two coils. In order to achieve automatic alignment between the transmitting coil and the receiving coil in WPT, and to obtain the best power transmission efficiency, we innovatively proposed a new optimization algorithm named the Maritime Search and Rescue Algorithm (MSRA). The algorithm not only has better optimization performance, but also has the ability to plan the path to the best site. For other existing intelligent optimization algorithms, it has never been found that they have both of these performances. Moreover, the mathematical model of the MSRA was established, and the computer program pseudo-code was created. Finally, we designed the entire hardware system and software system of WPT-AAD, and we built an experimental bench to experimentally verify all the previous theoretical analysis and designs to achieve the determined efficiency.

**Keywords:** Elderly cars, Electric vehicle, Maritime search and rescue algorithm (MSRA), Wireless power transfer

This material is reserved for educational use only, not allowed for commercial use.

Forbidden to modify the content, and cite the document when use.

## ACKNOWLEDGEMENT

I would like to acknowledge and give my warmest thanks to my supervisor Associate Professor Dr. Chaiyan Jettanasen who made this work possible. His guidance and advice carried me through all the stages of conducting my research and writing my thesis. I would also like to thank my committee members for letting my defense be an enjoyable moment, and for your brilliant comments and suggestions, thanks to you.

I would also like to give special thanks to my wife (Xie ShaoLing), and my family as a whole for their continuous support and understanding when undertaking my research and writing my thesis. It was a hard and memorable period for me in my life. Your prayer for me was what sustained me this far.

Finally, I would like to thank everyone or everything for letting me through all the difficulties. I have experienced guidance day by day. I also gained more expertise for my research area that will allow me to contribute more to my university in China.

Zheng Junlong

# TABLE OF CONTENTS

ABSTRACT IN THAI.....	VI
ABSTRACT IN ENGLISH .....	VII
ACKNOWLEDGEMENT.....	VIII
TABLE OF CONTENTS.....	IX
LIST OF TABLES.....	XI
LIST OF FIGURES .....	XII
LIST OF ABBREVIATIONS AND SYMBOLS.....	XV
<b>Chapter 1 Introduction.....</b>	<b>1</b>
1.1 Introduction.....	1
1.2 Research status about the wireless charging technology for EV.....	5
1.3 Objective.....	8
1.4 Scope of study .....	8
1.5 Thesis outline.....	8
<b>Chapter 2 The Overall Design of The Elderly EV.....</b>	<b>11</b>
2.1 The selection of various parameters.....	11
2.2 Design of elderly EV chassis.....	13
2.3 Analysis of the driving force for elderly EV .....	14
2.3.1 Rolling resistance.....	14
2.3.2 Air resistance.....	15
2.3.3 Climbing resistance.....	16
2.3.4 Acceleration resistance.....	16
2.3.5 The balance equation of car driving force and resistance.....	17
2.4 Main parameters of the driving motor .....	17
2.4.1 Rated power.....	18
2.4.2 Rated speed and driving power of straight road.....	19
2.4.3 Peak power.....	19
2.4.4 Peak torque.....	20
2.4.5 Maximum rotation speed and rated rotation speed.....	22
2.4.6 Rated torque of the motor.....	22
2.5 Selection of power battery.....	23

This material is reserved for educational use only, not allowed for commercial use.

Forbidden to modify the content, and cite the document when use.

<b>Chapter 3 Analysis of WPT Magnetic Field Distribution .....</b>	<b>26</b>
3.1 The Problems in WPT system of EV.....	27
3.2 The working principle for WPT system.....	28
3.3 mathematical model of magnetic field for transmitting coil.....	32
3.4 Magnetic field distribution diagram for transmitting coil .....	35
3.5 Analysis range of WPT magnetic field.....	40
3.6 Mathematical analysis of mutual inductance.....	43
3.7 Calculation of mutual inductance.....	46
<b>Chapter 4 Algorithm for Finding Maximum Mutual Inductance .....</b>	<b>50</b>
4.1 Algorithm overview.....	50
4.2 Principle of MSRA.....	54
4.3 Introduction to optimization algorithm test functions.....	58
4.4 Performance comparison between MSRA and other two algorithms.....	61
4.5 MSRA is applied to find the maximum mutual inductance.....	72
<b>Chapter 5 WPT-AAD of Design and Experiment.....</b>	<b>74</b>
5.1 Structural design for WPT-AAD.....	74
5.2 Design of MCU control program.....	78
5.3 Setup of WPT-AAD experimen bench.....	80
5.4 Analysis of MCR-WPT experimental data.....	91
5.5 Analysis of mutual inductance experimental data.....	98
5.6 Analysis of WPT- AAD experimental data .....	101
<b>Chapter 6 Conclusion and Suggestion .....</b>	<b>103</b>
<b>References.....</b>	<b>106</b>
<b>Related Publications.....</b>	<b>112</b>
<b>AUTHOR BIOGRAPHY AND PROCEDURES FOR THESIS WRITING .....</b>	<b>115</b>

This material is reserved for educational use only, not allowed for commercial use.

Forbidden to modify the content, and cite the document when use.

## LIST OF TABLES

Table 2-1-1 Main parameters and design goals of vehicles[19].....	13
Table 2-4-1 Basic parameters of driving motor .....	23
Table4-4-1 5000 iterations error analysis table (5 functions).....	65
Table4-4-2 20000 iterations error analysis table (5 functions).....	65
Table4-4-3 Error and optimization target point location (Schwefe function).....	68
Table4-4-4 Error and optimization target point location (Schaffer function).....	69
Table5-4-1. MCR-WPT experiment 1.....	92
Table5-4-2. MCR-WPT experiment 2.....	93
Table5-4-3. MCR-WPT experiment 3.....	93
Table5-4-4. MCR-WPT experiment 4.....	95
Table5-4-5. MCR-WPT experiment 5.....	97
Table5-5-1. Mutual induction distribution experiment.....	99
Table5-6-1 MSRA be applied to WPT-AAD for finding the position of the maximum mutual inductance.....	101

# LIST OF FIGURES

Fig.1-1-1 Classification of electric walking tools for the elderly by appearance [1].	2
Fig.1-1-2 Classification of electric walking tools for the elderly the number of wheels. [1].....	2
Fig.1-1-3 Classification of electric walking tools for the elderly the number of seats. [1].....	2
Fig.1-1-4 Walking aids for the elderly. [1] .....	3
Fig.1-1-5 Other means of transportation for the elderly. [1] .....	3
Fig.1-2-1 MIT lab bench [3].....	6
Fig.1-2-2 Abridged view of EV wireless power transmission [9].....	7
Fig. 2-1-1 Baojun E100 [19] .....	12
Fig.3-2-1 MCR-WPT system composition structure diagram [27].....	29
Fig.3-3-1 The magnetic induction intensity produced by an electrified wire at any point around it [32].....	33
Fig.3-3-2 The magnetic induction intensity of an electrified straight wire at any point around it.....	33
Fig.3-3-3 The magnetic induction intensity produced by an electrified quadrilateral at any point around it.[32].....	34
Fig.3-4-1 planar graph of transmitting coil [31].....	36
Fig.3-4-2 Bz distribution map (Z=0.20 I=20). .....	37
Fig.3-4-3 Bz distribution contour map. (Z=0.20 I=20).....	37
Fig.3-4-4 Bz distribution map (Z=0.20 I=-20).....	38
Fig.3-4-5 Bz distribution contour map (Z=0.20 I=-20) .....	38
Fig.3-4-6 Bz distribution map (Z=0.15 I=20) .....	38
Fig.3-4-7 Bz distribution contour map (Z=0.15 I=20).....	38
Fig.3-4-8 Bz distribution map (Z=0.10 I=20) .....	39
Fig.3-4-9 Bz distribution contour map (Z=0.10 I=20).....	39
Fig.3-5-1 Schematic diagram of the EV parking at the limit position in the upper right corner.....	41
Fig.3-5-2 Schematic diagram of active range of transmitting coil .....	42
Fig.3-6-1 planar graph of receiving coil [31] .....	44

This material is reserved for educational use only, not allowed for commercial use.

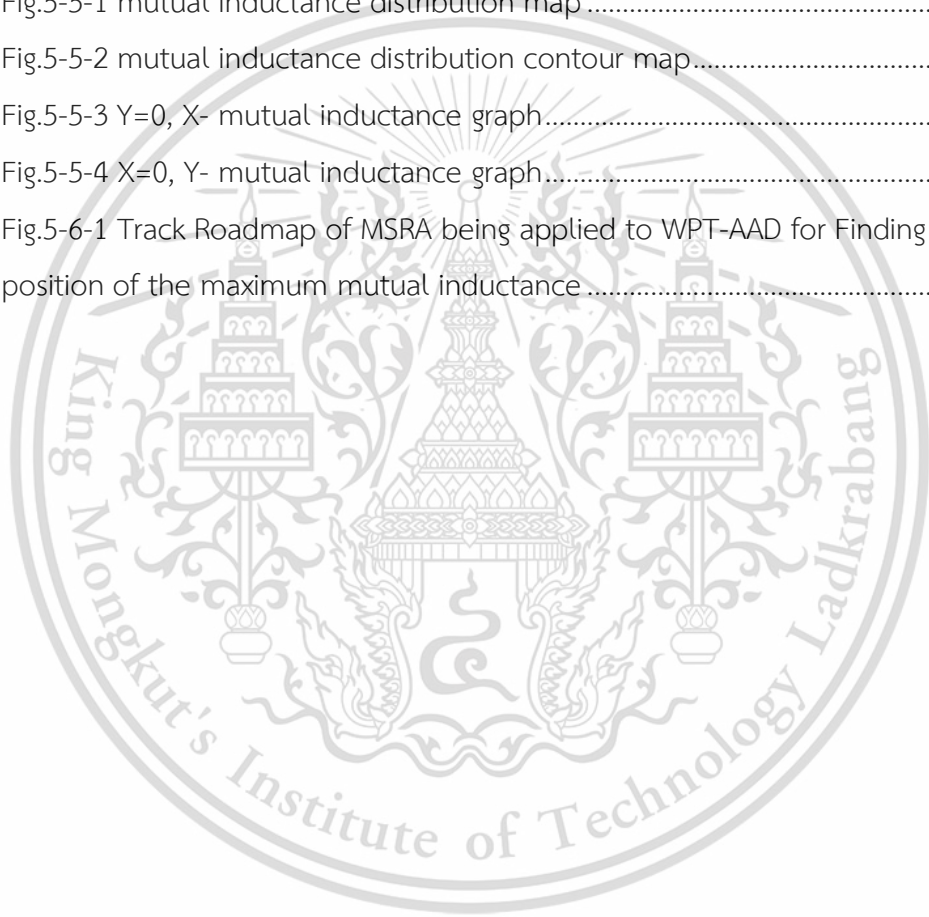
Forbidden to modify the content, and cite the document when use.

Fig.3-6-2 Illustration of calculation parameters.....	46
Fig.3-7-1 mutual inductance distribution map .....	48
Fig.3-7-2 mutual inductance distribution contour map.....	48
Fig.3-7-3 Y=0, X- mutual inductance graph.....	48
Fig.3-7-4 X=0, Y- mutual inductance graph.....	48
Fig.4-1-1 SMA trajectory route of optimization operation.....	52
Fig.4-1-2 The path planning base on GWA [43].....	53
Fig.4-2-1 Scenario diagram of maritime search rescue [46] .....	54
Fig.4-2-2 Schematic diagram of MSRA (The objective function is the Schwefe).....	55
Fig.4-3-1 Ackley function.....	59
Fig.4-3-2 Rastrigin function.....	59
Fig.4-3-3 Sphere function.....	60
Fig.4-3-4 Schwefe function.....	61
Fig.4-3-5 Schaffer function .....	61
Fig.4-4-1 Algorithm iteration curve ( Ackley function ) .....	63
Fig.4-4-2 Algorithm iteration curve ( Rastrigin function ) .....	63
Fig.4-4-3 Algorithm iteration curve ( Sphere function ) .....	63
Fig.4-4-4 Algorithm iteration curve ( Schwefe function ) .....	64
Fig.4-4-5 Algorithm iteration curve ( Schaffer function ) .....	64
Fig.4-4-6 MSRA and SMA Search track (Schwefe function).....	67
Fig.4-4-7 MSRA and SMA Search track (Schaffer function) .....	68
Fig.4-4-8. MSRA trajectory to find the optimal value (Sphere function). .....	71
Fig.4-5-1 Trajectory diagram of MSRA search the maximun mutual inductance.....	73
Fig.5-1-1 Diagram of the WPT-AAD .....	75
Fig.5-1-2 Overall installation layout of the WPT-AAD .....	77
Fig.5-2-1 Main program flow chart of MCU.....	78
Fig.5-2-2 X-direction subprogram flow chart of MCU .....	79
Fig.5-2-3 Y-direction subprogram flow chart of MCU .....	80
Fig.5-3-1 MCR-WPT System circuit diagram .....	82
Fig.5-3-2 Detailed diagram of main circuit ②.....	83
Fig.5-3-3 Detailed diagram of driving circuit ①.....	85
Fig.5-3-4 Structure diagram of transmitting coil [31] .....	86

This material is reserved for educational use only, not allowed for commercial use.

Forbidden to modify the content, and cite the document when use.

Fig.5-3-5 Structure diagram of transmitting coil [31] .....	87
Fig.5-3-6 Photos of the WPT-AAD experimental bench .....	88
Fig.5-3-7 Partial detail of the WPT-AAD experimental bench .....	89
Fig.5-3-8 L1 inductance measurement.....	91
Fig.5-3-9 L2 inductance measurement.....	91
Fig.5-4-1 Diagram for WPT drive frequency, input voltage and efficiency .....	94
Fig.5-4-2 Diagram for input voltage and efficiency .....	96
Fig.5-4-3 Diagram for Distance between two coils and efficiency .....	98
Fig.5-5-1 mutual inductance distribution map .....	100
Fig.5-5-2 mutual inductance distribution contour map.....	100
Fig.5-5-3 $Y=0$ , X- mutual inductance graph.....	100
Fig.5-5-4 $X=0$ , Y- mutual inductance graph.....	100
Fig.5-6-1 Track Roadmap of MSRA being applied to WPT-AAD for Finding the position of the maximum mutual inductance .....	102



## LIST OF ABBREVIATIONS AND SYMBOLS

WPT	Wireless Power Transfer
MCR-WPT	Magnetically Coupled Resonant Wireless Power Transfer
WPT-AAD	Wireless Power Transmission Automatic Alignment Device
L1	Transmitting coil
L2	Receiving coil
MSRA	Maritime Search and Rescue Algorithm
SMA	Slime Mold Algorithm
GeneticA	Genetic Algorithm
$M$	Mutual inductance coefficient
$R_L$	Equivalent load at the output
$\eta$	Efficiency of the whole MCR-WPT system
$U_i$	Input voltage
$I_i$	Input current
$U_o$	Output Voltage

# Chapter 1

## Introduction

### 1.1 Introduction

Population aging is a global issue and a shared challenge for the advancement of human society. The aging process of China's population is advancing rapidly, characterized by a large population and a high degree of aging. The problem of the aging population is increasing. How to help individuals spend their old age better and improve their happiness is a problem that our society needs to pay attention to. Traveling is an important way for the elderly to maintain their daily activities and connect with society. It is also an important aspect of enhancing the happiness of the elderly.

In recent years, with the continuous development of society, the growth of urban population, and the rise in traffic pressure, many existing transportation methods are not suitable for the elderly. Many elderly individuals refrain from traveling due to travel challenges. There is limited research in this area globally, and the transportation issues of the elderly need to be addressed urgently.

The purposes of elderly travel are roughly divided into exercise, leisure and entertainment, shopping, picking up children, visiting a doctor, visiting relatives and friends, and handling personal affairs. Among them, exercise and leisure activities are the most common. In terms of travel mode, due to the current transportation and traffic environment restrictions, most of the time the elderly is limited to walking and public transportation, and the travel distance is mainly short. Therefore, the purpose and significance of this research are to design a car that is suitable for the elderly to drive independently within the city, covering a total round-trip distance of approximately 100 kilometers, in order to provide more convenient transportation options for the elderly.

There are currently existing mobility aids for the elderly available on the market, including mobility scooters, as depicted in the figure below:



Fig.1-1-1 Classification of electric walking tools for the elderly by appearance [1]



Fig.1-1-2 Classification of electric walking tools for the elderly the number of wheels. [1]



Fig.1-1-3 Classification of electric walking tools for the elderly the number of seats. [1]

This material is reserved for educational use only, not allowed for commercial use.

Forbidden to modify the content, and cite the document when use.



Fig.1-1-4 Walking aids for the elderly. [1]

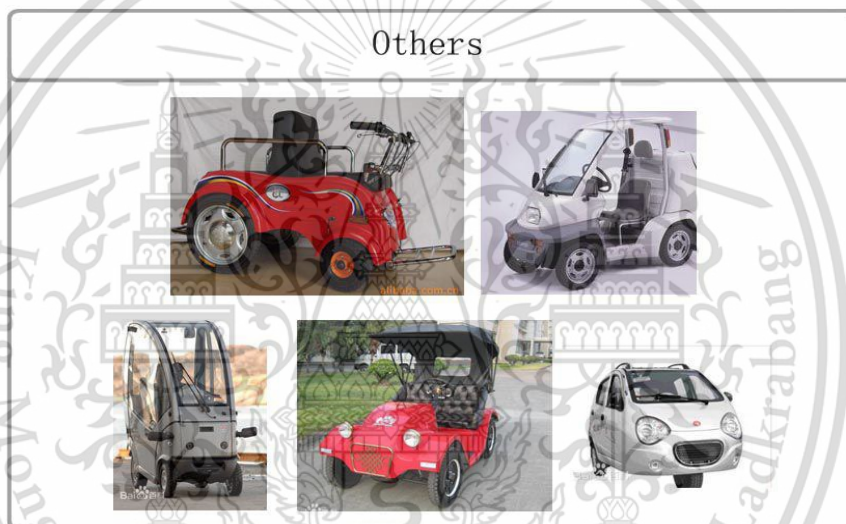


Fig.1-1-5 Other means of transportation for the elderly. [1]

The advantages of mobility tools for the elderly currently on the market are:

1. Low cost and low market price, which solves the short-distance travel problem of the elderly within 2 km;
2. The weight and volume are relatively small, compact and light.

Existing problems:

1. Long-distance travel, such as travel within a city, these means of transportation are not enough;
2. The comfort performance is too poor. There is no air conditioning, and there is no good audio system; most types do not have a complete car box, and lack the function of rain and wind.

3. The driving speed is slow, and the maximum speed of most models is only

This material is reserved for educational use only, not allowed for commercial use.

Forbidden to modify the content, and cite the document when use.

20 km/h, which does not meet the travel needs of the elderly well.

4. The safety performance is poor, and the safety systems such as airbags and ABS on elderly cars are lacking.

5. The performance of passing obstacles is poor.

6. The charging method for these elderly cars are all the plug-in charging method, and there is no convenient wireless charging method. Of course, the wireless charging technology is not yet mature in the charging of automotive power batteries, and large-scale commercial use has not been found worldwide.

From the analysis of the market products of elderly cars, it is urgent necessities to design an elderly car that can go back and forth in a city and a set of convenient wireless charging system for it

At present, there are two main ways to charge an electric car: wired charging and wireless charging. The wired charging method for electric vehicles involves charging the vehicle through the charging gun connected to the charging station. This method is less flexible and can lead to wear and tear on the charging interface, potentially causing sparks and reducing safety. If you encounter severe weather conditions such as rain and snow, there is a higher likelihood of experiencing an electric shock due to factors such as the aging of the charging gun or cable, leakage, etc. In contrast, the application of wireless charging technology can effectively avoid the above-mentioned shortcomings. Wireless charging technology offers greater advantages in terms of convenience and security. The wireless charging transmitter is buried underground and transfers energy through an electromagnetic field. It does not produce sparks, experience wear and tear, and resolves security and maintenance issues. Wireless charging enables electric vehicles to charge while in motion and while at rest using a ground transmitter disk and an in-car receiver disk. In addition, wireless charging for electric vehicles can be performed without manual operation, significantly enhancing the user experience.

The wireless charging technology for electric vehicles has been extensively researched and implemented. However, due to the high manufacturing costs and lack of market support, wireless charging vehicles have not yet been widely adopted for commercial use. The research adapts wireless charging technology to elderly electric vehicles, aiming to enhance the convenience of charging and address the security risks associated with charging these vehicles.

This material is reserved for educational use only, not allowed for commercial use.

Forbidden to modify the content, and cite the document when use.

Based on the current research internationally, this thesis focuses on studying and designing an electric vehicle tailored for elderly individuals to commute within a city. Additionally, it designs a supporting wireless charging system that can automatically align. This research is of great significance in addressing the transportation challenges faced by the elderly in urban areas and improving the convenience of charging.

At present, the wireless charging technology that can automatically align is being applied to electric vehicles for the elderly worldwide, and no research in this field has been found. Therefore, this thesis focuses on the automatic alignment device for wireless charging.

## **1.2 Research status about the wireless charging technology for EV.**

Transmission of power without wires for supplying power to electrical devices and equipment, and for charging has been contemplated since the times of Tesla. However, this was not possible at that time because associated enabling technologies were not available[2]. A breakthrough to this end was achieved in 2007. In June 2007, the experimental team at the Massachusetts Institute of Technology (MIT) made a major discovery. Under the leadership of Professor Marin Soljačić, they discovered magnetic field resonance technology and used it to successfully light an electric bulb located 2 meters away from the experimental bench. Moreover, a safety test was conducted, and it was found that this type of power transmission would not endanger the people nearby [3].

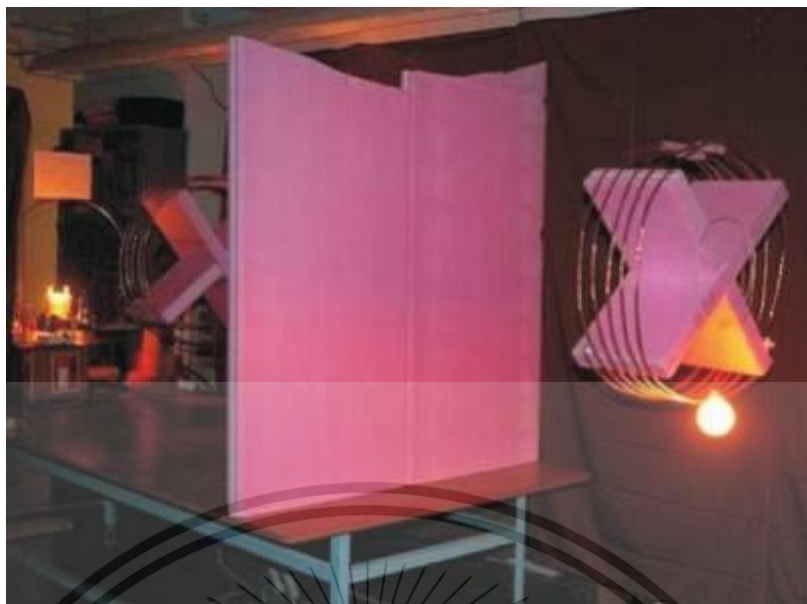


Fig.1-2-1 MIT lab bench [3]

Wireless Power Transfer (WPT) and its practical implementations are being widely investigated due to their potential use in a variety of industrial and engineering applications [2]. Some of the applications where WPT can be used include EVs, electronic gadgets [4], [5], industrial plants [6], implanted medical devices [7], and so on.

Reference [8] summarizes several forms of wireless charging technology: Microwave WPT, laser WPT, electromagnetic induction WPT, electric field coupling WPT, and Magnetically-Coupled Resonant WPT. Among them, Magnetically Coupled Resonant Wireless Power Transfer (MCR-WPT) technology utilizes a non-radiated magnetic field to transmit energy, resulting in less external electromagnetic interference and improved safety. This technology is particularly well-suited for ground-based applications. Compared with electromagnetic induction WPT and electric field coupling WPT, MCR-WPT technology offers a longer transmission distance (up to several meters) and greater flexibility. It can be used for wirelessly charging moving objects. Due to the unique advantages mentioned above, MCR-WPT technology is the most suitable option for automotive wireless charging compared to other WPT technologies. It has a broad range of applications and significant commercial value. Fig.1-2-2 shows the structural diagram of MCR-WPT.

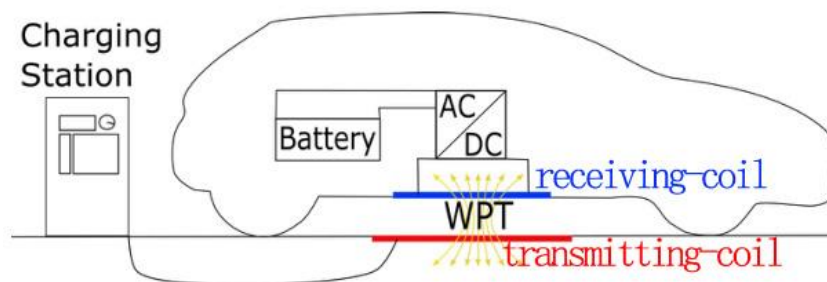


Fig.1-2-2 Abridged view of EV wireless power transmission [9]

For the MCR-WPT system research, Lionel Pichon [10] made a detailed analysis of the magnetic induction strength. Rui Feng et al [11] detailed analyzed of magnetic field distribution. Yang Yang et al [12], optimized the shape and structure of transmitting and receiving coils. Kafeel Ahmed Kalwar, et al [13], proposed a new coil design qad D quadrature. Sangwook Park [14] maded electromagnetic exposure assessment and analyzed the impact of different exposure scenes on human body. Haris Gulzar, et al [15], made a comprehensive electromagnetic design for MCR-WPT, and experiments verified that MCR-WPT can transmit power wirelessly with an efficiency of more than 85%. Rupesh Kumar Jha et al [16] analyzed the unit resonant topology used for WPT, and the performance of the topology is comprehensively evaluated and compared. Ihssen Jabri et al [17] analyzed the influence of transverse misalignment and separation distance between primary and secondary coils. Metaheuristic algorithm and genetic algorithm were used to optimize the design of primary and secondary coils.

Literature[18], in 2019 by Wings, J. et al. Carried out multi-objective optimization on the transmission efficiency and output power of the MCR-WPT system from various perspectives, including the physical structure of the system and its components, as well as voltage and current values in the circuit. The study yielded optimal research results: when the resonant frequency is 85 kHz, the transmission distance ranges from 0.8 to 1.6 times the maximum coil radius, and the maximum power output is between 4 kW and 9 kW. The system demonstrates an efficiency of over 90% in transmission.

To sum up, research on wireless charging technology for electric vehicles has accumulated significantly, providing a foundation for the integration of this technology into vehicles used by the elderly.

### 1.3 Objective

The objectives of this research are as follows:

- 1) To design a convenient wireless charging system for elderly individuals' cars.
- 2) To enhance the convenience of the wireless power transfer (WPT) system, the automatic alignment device (AAD) for WPT is thoroughly researched.
- 3) A new optimization algorithm, the Maritime Search and Rescue Algorithm (MSRA), has been proposed and implemented to enable the WPT-AAD to automatically find the optimal charging position.

### 1.4 Scope of study

- 1) The wireless charging system designed in this thesis for the elderly electric vehicle utilizes magnetic coupling resonance wireless power transfer.
2. The WPT-AAD control unit studied in this thesis is the Microcontroller Unit (MCU), not other control components such as a programmable controller.

### 1.5 Thesis outline

Chapter 1 elaborates on the current market situation of the elderly electric vehicle (EV) industry. It is understood that the current electric vehicle (EV) products designed for elderly individuals in the market do not adequately cater to their city travel needs. Moreover, the process of charging these vehicles poses safety risks and inconvenience for elderly users. It is proposed to research and design an elderly-friendly car with an automatic alignment wireless charging system that can travel within a city. This thesis discusses the current research status of wireless charging and automatic alignment devices for electric vehicles both domestically and internationally. It suggests that studying elderly cars with automatic alignment wireless charging systems is necessary, feasible, and innovative. At the same time, it is proposed that the focus of this thesis is Wireless Power Transfer with Automatic Alignment Device (WPT-AAD).

Chapter 2, the fundamental parameters of the chassis for an elderly electric vehicle (EV) are initially chosen. This selection serves as a guide for the intricate design

This material is reserved for educational use only, not allowed for commercial use.

Forbidden to modify the content, and cite the document when use.

of an EV tailored to meet the transportation requirements of elderly individuals in urban areas. Subsequently, a detailed calculation is conducted to determine the driving force, motor selection, and power battery capacity for the elderly EV. These calculations lay the groundwork for designing a wireless charging system with an automatic alignment function.

Chapter 3 briefly introduces the structure and working principle of the electric vehicle magnetic coupling resonant radio energy transmission system. According to Biot-Savart's law, the magnetic field generated by the energy-transmitting coil in the wireless charging system is analyzed and calculated in detail. The mathematical expression for the magnetic induction intensity generated by the transmitting coil at any point in space is derived. Then, the distribution map of the magnetic induction intensity in the magnetic field space is created using the computer software Python. This map serves as the foundation for analyzing the mutual inductance between the transmitting coil and the receiving coil. Then, the mutual inductance distribution between the transmitting coil and the receiving coil is calculated in detail as the relative position of the transmitting coil and the receiving coil changes within this range. Finally, the distribution position of the maximum mutual inductance is derived. The research on the distribution of mutual inductance between the transmitting coil and receiving coil in space provides a theoretical basis for the design of MCR-WPT system.

Chapter 4 introduces a new optimization algorithm called the Marine Search and Rescue Algorithm (MSRA). Together with SMA and GeneticA, the algorithm is applied to five well-known optimization algorithm test functions (Ackley, Rastrigin, sphere, Schaffer, Schwefel), and the results are compared and analyzed. The conclusion that MSRA has excellent performance is supported. The thesis then discusses the application of MSRA to WPT-AAD to determine the position of the maximum mutual inductance coefficient and achieve automatic alignment for wireless charging.

Chapter 5 discusses the hardware system design of WPT-AAD, and the control program developed by MSRA for WPT-AAD is described. Then, the WPT-AAD experimental bench was built, and five experiments with different parameters of MCR-WPT were conducted on the bench. Subsequently, WPT-AAD experiments were performed using appropriate parameters of MCR-WPT. In each experiment, the experimental data were recorded in detail and analyzed to verify that all theoretical

This material is reserved for educational use only, not allowed for commercial use.

analyses and designs in this thesis are completely correct and feasible.

Chapter 6: Conclusion and Suggestions.



This material is reserved for educational use only, not allowed for commercial use.

Forbidden to modify the content, and cite the document when use.

## Chapter 2

### The Overall Design of The Elderly EV

In this chapter, the fundamental parameters of the chassis of an elderly electric vehicle (elderly EV) are preliminarily selected. This serves as a reference for the detailed design of an elderly EV to meet the travel needs of the elderly in a city. Subsequently, the driving force, selection of the driving motor, and power battery capacity of the elderly EV are calculated in detail. This forms the basic groundwork for the design of a wireless charging system with an automatic alignment function.

This chapter is structured as follows. In section 2.1, the fundamental parameters of the chassis for the elderly EV are preliminarily selected. In Section 2.2, A basic design for the elderly EV chassis is provided. In Section 2.3, we analyzed and calculated the driving force for elderly EV. In Section 2.4, we calculated and analyzed the main parameters of the driving motor. In section 2.5, we calculate and analyze the capacity of the power battery.

#### 2.1 The selection of various parameters

The elderly car is designed for elderly individuals' travel needs. According to market research, there are currently two types of transportation vehicles available for the elderly: electric tricycles and electric four-wheel mini-cars.

Electric tricycles are compact in size, have a small footprint, and offer flexibility in driving and turning. However, they lack body balance, making them prone to overturning during emergency braking. These tricycles have a limited cruising range, suitable only for short-distance trips for the elderly (within 10 kilometers). The anti-theft mechanism for the car battery is inadequate, making it vulnerable to theft, causing inconvenience for the elderly. According to China's traffic laws, this model is classified as a power-assisted transportation tool, not a motor vehicle, and is not permitted on highways. It is inconvenient to use in cities.

Electric four-wheeled mini-cars overcome many of the shortcomings of electric tricycles and significantly enhance the travel convenience for the elderly. However, the current electric four-wheeled mini-cars still have some shortcomings. They exhibit poor driving performance, are unsuitable for navigating uneven terrains, and struggle

This material is reserved for educational use only, not allowed for commercial use.

Forbidden to modify the content, and cite the document when use.

to traverse small steps onto sidewalks. Additionally, there is a lack of adequate safety protection equipment for the elderly. Therefore, it is necessary to design a brand-new electric vehicle suitable for the travel needs of the elderly in the city.



Fig. 2-1-1 Baojun E100 [19]

In cities, traffic congestion is common, and parking spaces in ground parking lots are very limited. Most cars can only be parked in underground parking lots in urban areas, or they can find parking spaces away from shopping malls, parks, and other crowded places. Due to their advanced age, elderly individuals move slowly, making parking in underground lots or distant locations particularly inconvenient for them. Therefore, the compact car for the elderly should be small in size and able to be parked in the designated bicycle parking space next to the sidewalk. With reference to existing cars, it is found that the size of the "Baojun E100" [19] model produced by Chinese SAIC-GM-Wuling is more suitable. Therefore, the size, axle moment, front wheel moment, and rear wheel moment of the elderly car in this study are all based on the "Baojun E100" model. Other parameters should be adjusted according to the specific requirements of the elderly car, as outlined in the table below.

Table 2-1-1 Main parameters and design goals of vehicles[19]

Parameter name	Value	Parameter name	Value
Length, width and height; (mm)	2488*1506*1670	Maximum cruising mileage; (km)	200
Axle moment, (mm)	1600	$M_o$ , vehicle mass (kg)	840
Front wheel moment, (mm)	1310	$M_L$ , load mass (kg)	150
g, gravitational acceleration, (m/s <sup>2</sup> ).	9.8	$M_a$ , full load mass (kg)	990
Rear wheel moment, (mm)	1320	$G$ , the total gravity of the full load car (N)	9702
Minimum ground clearance; (mm)	180	$i_t$ , total speed ratio	16.3
$u_{max1}$ , maximum speed (km/h)	80	$A$ , windward area (m <sup>2</sup> )	2.244
$u_{max2}$ , highest lasting Speed (km/h)	60	$\eta_t$ , transmission efficiency	0.9
$u_c$ , conventional cruising speed (km/h)	40	$R_t$ ; tire radius (m)	0.306
$f$ , Rolling resistance coefficient	0.016	$\alpha_{max}$ , maximum climbing slope	20% 11.3°
$t_1$ , 0-40 km/h acceleration time (s)	10	$t_2$ , 40-80 km/h acceleration time (s)	10
$C_D$ ; wind resistance coefficient	0.8	$\delta$ , rotating mass conversion factor	1.06

## 2.2 Design of elderly EV chassis

Focusing on the Baojun E100 [19] electric vehicle, its chassis structures are as follows: single motor, front electric motor, front-wheel drive, single-speed transmission for electric vehicles, front suspension is a person independent suspension, rear This material is reserved for educational use only, not allowed for commercial use.

Forbidden to modify the content, and cite the document when use.

suspension is a single-arm independent suspension, both front and rear brakes are disc brakes, and the parking brake is a hand brake. The elderly EV in this thesis also adopted the chassis structure of this car. The wheel tire size of the Baojun E100 is 145/70 R12 [19]. According to the marking method of automobile tire model specification [20], the wheel radius can be calculated as follows:

$$145 \times 70\% + 12 \times 25.4/2 = 253.9 \quad (\text{mm}) \quad (2-2-1)$$

The Baojun E100 equipped with these wheels has a minimum ground clearance of only 130 mm [19]. So, it can be considered that the highest obstacle that the car chassis can pass, is only 130mm higher than the wheels. Referring to Huang Chaosheng's analysis of wheeled vehicles passing vertical obstacles [21], it can be estimated that the maximum size of wheels with a radius of 253.9 mm that can climb over vertical obstacles is 200 mm.

In order for the elderly EV designed in this thesis to be able to climb into a bicycle parking space on an urban sidewalk with a vertical height of 250 mm [22] for parking, the wheel radius needs to be increased by 50 mm ( $250 - 200 = 50$  mm). Check the car tire standards and choose 145/80 R15 [23]. According to the marking method of automobile tire model specification [20], the wheel radius of the elderly EV can be calculated as follows.

$$145 \times 80\% + 15 \times 25.4/2 = 306.5 \quad \text{mm} \quad (2-2-2)$$

That is, the wheel radius is 306.5 mm. Only considering the wheel radius design, referring to Huang Chaosheng's analysis of wheeled vehicles passing vertical obstacles [21], it can be estimated that the wheels with a radius of 306.5 mm, can climb over the maximum size of vertical obstacles is 250 mm.

## 2.3 Analysis of the driving force for elderly EV

### 2.3.1 Rolling resistance

Calculation formula of automobile rolling resistance [20]

This material is reserved for educational use only, not allowed for commercial use.

Forbidden to modify the content, and cite the document when use.

$$F_f = G \times f \quad (\text{N}) \quad (2-3-1)$$

where,

$G$ , is the total gravity of the car.

$f$ , the rolling resistance coefficient, which is related to the type of road surface, driving speed, and tire structure, material, and air pressure. When the vehicle speed is less than 50 km/h,  $f=0.0165$ , When the speed is greater than 50 km/h, it can be calculated using the following formula.[20]:

$$f = 0.016 \times [1 + 0.01 \times (V - 50)] \quad (2-3-3)$$

The driving speed of the elderly EV in this thesis is designed based on Table 2-1-1, which includes the maximum driving speed. In the table,  $U_c=40$  km/h. This indicates that the vehicle speed is below 50 km/h in most cases. To simplify the calculation of  $f$ , a uniform value of 0.016 is used, and the above value is substituted for calculation. The result is:  $F_f= 160.1$  N.

### 2.3.2 Air resistance

Car air resistance calculation formula [20]

$$F_w = \frac{C_D A u_a^2}{21.25} \quad (\text{N}) \quad (2-3-4)$$

where,

$F_w$ , car air resistance

$C_D$ , air resistance coefficient, as shown in Table 2-1-1,  $C_D=0.8$ .

$A$ , the windward area of the car, as shown in Table 2-1-1,  $A=2.244$  m<sup>2</sup>.

$u_a$ , car speed, unit km/h, the accurate calculation should be the speed of the car relative to the air. When there is no wind, it is the driving speed of the vehicle. In most cases, the normal cruising speed of the car speed is directly used. As shown in Table 2-1-1,  $u_a=u_c=40$  km/h.

Substitute relevant parameters for calculation, and get:  $F_w=10.43$  N.

This material is reserved for educational use only, not allowed for commercial use.

Forbidden to modify the content, and cite the document when use.

### 2.3.3 Climbing resistance

Vehicle climbing resistance, when the vehicle is driving uphill. The component force of the vehicle's gravity along the direction of the slope is expressed as the vehicle climbing resistance. The calculation formula is:[20]

$$F_i = G \sin(\beta) \quad (2-3-5)$$

where,

$F_i$ , climbing resistance, (N).

$G$ , is the total gravity of the car (N).

$\beta$ , the acute angle formed by the ramp and the horizontal line. As shown in Table 2-1-1, the maximum climbing slope is 20%, then  $\sin(\beta)=0.1961$ .

Substitute the relevant parameters for calculation, and get:  $F_i=194.139$  N

### 2.3.4 Acceleration resistance

When the vehicle is accelerating, the inertial force generated by the mass is the acceleration resistance, denoted as  $F_J$ . For the inertial force, the mass of the vehicle is divided into two parts: translational mass and rotational mass. When accelerating, the translational mass produces inertial force, and the rotating mass produces moment of inertia. In order to simplify the calculation, the inertia moment produced by the rotating mass is typically transformed into the inertial force of the translational mass. The coefficient  $\delta$  is the conversion coefficient of vehicle rotation mass. Then, the acceleration resistance of the vehicle  $F_J$  can be written as:[20]

$$F_J = \delta M_a \frac{dv}{dt} \quad (\text{N}) \quad (2-3-6)$$

where,

$\delta$ , the conversion coefficient of vehicle rotation mass.

$M_a$ , the mass of the vehicle, (kg).

$dv/dt$ , the acceleration of the vehicle, (m/s<sup>2</sup>).

This material is reserved for educational use only, not allowed for commercial use.

Forbidden to modify the content, and cite the document when use.

Refers to Table 2-1-1 and substitute the relevant parameters for calculation, when the car accelerates uniformly from 0 to 40 km/h on a flat road in 10 seconds,  $F_J=1165.88$  N.

### 2.3.5 The balance equation of car driving force and resistance

In order to analyze the dynamic performance index of the automobile, the mechanical model of the automobile is established. According to automobile theory, the balance equation of automobile driving mechanics is:[20]

$$F_t = \sum F = F_f + F_W + F_i + F_J \quad (\text{N}) \quad (2-3-8)$$

Where:

$F_t$ , the driving force of the car, (N).

$F_f$ , the air resistance of the car, (N);

$F_i$ , the climbing resistance of the car, (N);

$F_J$ , the acceleration resistance of the car, (N);

In this thesis, refers to Table 2-1-1, when a car is driving on a flat road at a normal speed  $v_c=40$  km/h,  $F_i = F_J = 0$ , and the value is substituted into the calculation to be  $F_t=170.53$  N;

When driving at a constant speed on a slope of 20% of the road, and the value is calculated as  $F_t=356.85$  N;

When the car is uniformly accelerating from 0 to 40 km/h on a flat road in 10 seconds,  $F_t = 1328.587$  N.

### 2.4 Main parameters of the driving motor

In order to ensure that the elderly EV has good power and cost efficiency, it is necessary to carry out reasonable calculation and matching selection of the motor. The matching of EV driving motor mainly considers the performance indexes such as power, torque and speed. Referring to the knowledge of automobile theory [20], the performance indexes are calculated and analyzed as follows:

### 2.4.1 Rated power

Rated power: refers to the maximum power required under the condition of continuous operation of the equipment and ensuring the specified indicators.

(1) The rated power must meet the maximum stable speed [20]. As shown in Table 2-1-1, the maximum stable speed is 60 km/h.

According to the driving requirements of EVs, the rated power of the motor is generally selected according to the maximum stable speed of the vehicle during uniform driving on a flat road [20].

$$P_e = \frac{u_{max}}{3600\eta_t} (M_a g f + \frac{C_D A u_{max}^2}{21.25}) \quad (2-4-1)$$

Where:

$P_e$ , rated power of motor, (kW).

$u_{max}$ , maximum speed, (km/h).

$M_a$ , total mass of vehicle under full load, (kg).

$g$ , gravitational acceleration, (m/s<sup>2</sup>).

$f$ , rolling resistance coefficient;

$C_D$ , air drag coefficient;

$A$ , windward area, (m<sup>2</sup>).

$\eta_t$ , transmission efficiency.

Substitute the values from Table 2-1-1 into the above formula for calculation:

$$P_e = \frac{60}{3600 \times 0.9} \left( 990 \times 9.8 \times 0.016 + \frac{0.8 \times 2.244 \times 60^2}{21.25} \right) = 8.533 \text{ kW}$$

(2) The rated power must meet the stable climbing speed [20].

$$P_a = \frac{u_{cl}}{3600\eta_t} (M_a g f \cos \beta + \frac{C_D A u_{cl}^2}{21.25} + M_a g \sin \beta) \quad (2-4-2)$$

where,

$P_a$ , rated power of motor (kW).

$u_{cl}$ , climbing speed (km/h).

This material is reserved for educational use only, not allowed for commercial use.

Forbidden to modify the content, and cite the document when use.

$\beta$ , climbing slope.

The acute angle formed by the ramp and the horizontal line. When the car climbs a slope at a steady speed, the slope is usually calculated as 12% (6.8°) [20].

Substitute the values from Table 2-1-1 into the above formula for calculation.

$$P_a = \frac{40}{3600 \times 0.9} (990 \times 9.8 \times 0.016 \cos 6.8^\circ + \frac{0.8 \times 2.224 \times 40^2}{21.15} + 990 \times 9.8 \sin 6.8^\circ) = 17.747 \text{ kW}$$

Through the calculation of the above two items, the rated power  $P_a$  is taken the maximum value 17.747 kW.

#### 2.4.2 Rated speed and driving power of straight road

Minimum normal driving power, refers to the working condition that the vehicle runs in a straight line at a constant speed of rated speed (40 km/h, as shown in Table 2-1-1) on a straight road ( $\beta=0$ ). Required motor output power  $P_e$ . The formula (2-4-1) can be used for calculation:

$$P_e = \frac{40}{3600 \times 0.9} \left( 990 \times 9.8 \times 0.016 + \frac{0.8 \times 2.224 \times 40^2}{21.15} \right) = 3.578 \text{ kW}$$

#### 2.4.3 Peak power

Peak power refers to the maximum power that can be achieved on a straight road in a short time, as long as the basic functions are met, regardless of whether other quality indexes of the equipment can be achieved [20].

(1) The peak power should match the maximum power at the maximum speed (80 km/h, as shown in Table 2-1-1), which can be calculated by substituting the values from Table 2-1-1 into the formula (2-4-1).

$$P_{max1} = \frac{80}{3600 \times 0.9} \left( 990 \times 9.8 \times 0.016 + \frac{0.8 \times 2.244 \times 80^2}{21.15} \right) = 17.126 \text{ kW}$$

This material is reserved for educational use only, not allowed for commercial use.

Forbidden to modify the content, and cite the document when use.

(2) The peak power shall meet the maximum climbing gradient (20%, 11.3°, as shown in Table 2-1-1), which can be calculated by substituting the values from Table 2-1-1 into the formula (2-4-2).

$$P_{max2} = \frac{40}{3600 \times 0.9} [990 \times 9.8 \times 0.016 \cos(11.3^\circ) + \frac{0.8 \times 2.224 \times 40^2}{21.15} + 990 \times 9.8 \sin(11.3^\circ)] = 27.011 \text{ kW}$$

(3) The peak power needs to meet the power required for the acceleration time from the normal speed of 40 km/h to the maximum speed of 80 km/h within the limited time of  $t$  ( $t=t_2=10$  s, as shown in Table). It can be calculated according to the following formula [20].

$$P_{max t} = \frac{u_t}{3600 \eta_t} (m g f + \frac{C_d A u_t^2}{21.15} + \delta \cdot \frac{u_1 - u_0}{3.6 t}) \quad (2-4-3)$$

By substituting the values from Table 2-1-1, the calculation result is as follows.

$$P_{max t} = \frac{80}{3600 \times 0.9} (990 \times 9.8 \times 0.016 + \frac{0.8 \times 2.224 \times 80^2}{21.15} + 1.06 \times \frac{80 - 40}{3.6 \times 10}) = 17.155 \text{ kW}$$

The maximum value among  $P_{max1}$ ,  $P_{max2}$ ,  $P_{max t}$  (17.126 kW, 27.011 kW, 17.155 kW) is 27.011 kW, and this maximum value is multiplied by a safety factor of 2 to obtain the peak power ( $P_{max}$ ) [20], which is 54.022 kW.

#### 2.4.4 Peak torque

(1) The peak torque shall meet the requirements of the maximum climbing gradient [20] (the maximum gradient is 20%, 11.3°, as shown in Table 2-1-1):

$$T_{amax} \geq \frac{1}{\eta_t} \frac{[Gf \cos(\alpha_{max}) + G \sin(\alpha_{max})] R_t}{i_t} \quad (2-4-4)$$

where,

$T_{amax}$ , peak torque, (N-m).

$R_t$ , wheel radius, (m).

$i_t$ , total speed ratio.

$\eta_t$ , transmission efficiency.

$\alpha_{max}$ , the maximum climbing gradient.

By substituting the values from Table 2-1-1, the calculation result is as follows.

$$T_{amax} \geq \frac{1}{0.9} \times \frac{[990 \times 9.8 \times 0.016 \cos(11.3^\circ) + 990 \times 9.8 \sin(11.3^\circ)] \times 0.306}{16.3} = 50.388 \text{ N-m}$$

(2) The peak torque should meet the acceleration time, the speed from 0 to 40 km/h is uniform acceleration[20], and the time required is 10 seconds (as shown in Table 2-1-1).

$$T_{umax} \geq \frac{(Gft_1 + \delta mu_m + \frac{C_D A u_m^2}{21.15} \times \frac{t_1}{2}) \cdot R_t}{i_t \eta_t t_1} \quad (2-4-5)$$

where,

$t_1$ , 0-40 km/h acceleration time (s).

$\delta$ , Conversion coefficient of rotating mass;

$u_m$ , acceleration target speed (km/h);

$R_t$ , wheel radius, (m);

$i_t$ , total speed ratio;

$\eta_t$ , transmission efficiency.

Substitute the values from Table 2-1-1 for calculation:

$$T_{umax} \geq (990 \times 9.8 \times 0.016 \times 10 + 1.06 \times 990 \times 40$$

$$+ \frac{0.8 \times 2.224 \times 40^2}{21.15} \times \frac{10}{2}) \times \frac{0.306}{16.3 \times 0.9 \times 10} = 92.199 \text{ N-m}$$

After calculation, the peak torque  $T_{max}$  is taken the maximum value in  $T_{amax}$ ,  $T_{umax}$ , which is 92.199 N-m.

#### 2.4.5 Maximum rotation speed and rated rotation speed

The maximum rotation speed and rated rotation speed of the motor are determined according to the maximum speed of the vehicle and the normal speed respectively [20].

$$u_a = \frac{0.77 \times N \times R_t}{i_t} \quad (2-4-6)$$

where,

$u_a$ , vehicle running speed (km/h);

$N$ , motor speed (rpm);

$R_t$ , wheel radius (m);

$i_t$ , total speed ratio;

Substitute the value in Table 2-1-1 for calculation:

$$40 = \frac{0.77 \times N_e \times 0.306}{16.3}, \quad 80 = \frac{0.77 \times N_{max}}{16.3}$$

Rated rotation speed:  $N_e = 2794.565$  rpm

Maximum rotation speed:  $N_{max} = 5589.130$  rpm

#### 2.4.6 Rated torque of the motor

Rated torque, the rated torque is determined according to the rated power and rated speed of the motor [24]

$$T_e = \frac{9550 P_e}{N_e} \quad (\text{N-m}) \quad (2-4-7)$$

where,

$T_e$ , rated torque of motor, (N-m);

$P_e$ , rated power of motor, (kW);

$N_e$  rated speed of motor, (rpm).

Substituting into the numerical calculation, the rated torque is:

$$T_e = \frac{9550 \times 17.8}{2794.565} = 63.377 \text{ N-m}$$

Summarize the above calculations to the following table.

Table 2-4-1 Basic parameters of driving motor

Parameters of driving motor	Calculation results	Get value
$P_e$ , Rated power, (kW)	17.747	20
$P_c$ , rated speed and driving power of straight road, (kW)	3.578	3.6
$P_{max}$ , peak power, (kW)	54.022	55
$T_e$ , Rated torque, (N-m)	63.377	65
$T_{max}$ , Peak torque, (N-m)	92.199	100
$N_e$ , Rated speed, (rpm)	2794.565	3000
$N_{max}$ , Maximum speed, (rpm)	5589.130	6000

## 2.5 Selection of power battery

- 1). Maximum power output of battery.

During the operation of an EV, the output power of the power battery must be greater than or equal to the combined input power of the power motor and the on-board electrical equipment. From the parameter calculation and analysis of the motor in the previous section, the peak power of the motor is 55 kW. Generally, the total power consumption of the entire vehicle's electrical equipment (including air conditioning) is about 1.5 Kw [25]. It can be calculated that the peak power demand

This material is reserved for educational use only, not allowed for commercial use.

Forbidden to modify the content, and cite the document when use.

of the power battery output is 56.5 kW, which represents the maximum power output of the battery.

## 2). Total storage capacity of power battery

The total storage capacity of the power battery is directly related to the vehicle's maximum mileage once fully charged. If the total storage capacity of the battery is designed to be too small, it will result in limited mileage, thereby affecting the vehicle's performance. Conversely, if the total storage capacity of the battery is designed to be too large, it will lead to increased manufacturing costs and overall vehicle weight. The EV designed for the elderly in this thesis is primarily intended for use on urban roads, catering to the transportation needs of the elderly to and from the city. Therefore, the designed comprehensive mileage of the vehicle is 100 km.

According to the calculations in the previous section, the power of the driving motor is 3.578 kW when the vehicle runs at the rated speed of 40 km/h on a straight road. The power of the driving motor is 17.747 kW when the vehicle is climbing a slope of 12% (6.8°) at the rated speed of 40 km/h. The total power of electrical equipment, including the air conditioner, of the whole vehicle is approximately 1.5 kW. From the perspective of parameter conservation, the total storage capacity of a power battery can be calculated using the following formula [25].

$$E\xi\eta_q\eta_t\eta_m = (P_{motor} + P_{divice}) \cdot \frac{S}{u_e} \quad (2-4-7)$$

where,

$E$  represents the total energy of the power battery (kWh).

$\xi$  represents the discharge depth of the battery. In order to protect the power battery and avoid excessive discharge,  $\xi$  take 0.8 [25].

$\eta_q$  represents the battery discharge efficiency (0.95) [25].

$\eta_t$  is the transmission efficiency of the vehicle power system in Table 2-1-1.

$\eta_m$  is the efficiency of the motor in converting electric energy into mechanical energy (0.9) [25].

$P_{motor}$  is the power of the driving motor (kW).

This material is reserved for educational use only, not allowed for commercial use.

Forbidden to modify the content, and cite the document when use.

$P_{device}$  is the total power consumption of electrical equipment of the whole vehicle (kW)

$S$  is the endurance mileage of the vehicle under rated working conditions (km).

$u_e$  is the rated speed (km/h).

When estimating the overall city driving endurance mileage of an automobile, it can be roughly calculated based on the assumption that straight roads make up 70% and other complex road conditions make up 30% [25]. In order to simplify the calculation, the power consumption of these 30% complex road conditions is calculated based on the power consumption of an automobile at the rated speed of 40 km/h and a climbing slope of 12% [25]. The detailed calculation is as follows.

$$E \times 0.8 \times 0.95 \times 0.9 \times 0.9 = [(3.578 + 1.5) + (17.747 + 1.5)] \times \frac{100 \times 30\%}{40} \Rightarrow E = 37.885 \text{ kWh}$$

Through the above calculation, it can be seen that the total storage capacity of the designed power battery should be 38 kWh.

The parameter calculations in this chapter have laid the groundwork for the subsequent research.

## Chapter 3

### Analysis of WPT Magnetic Field Distribution

This chapter briefly introduces the structure and working principle of the magnetic coupling resonance radio energy transmission system for electric vehicles. According to Biot-Savart's Law, the magnetic field generated by the energy transmitting coil in the wireless charging system is reasoned, analyzed, and calculated in detail. The mathematical expression of the magnetic induction intensity generated by the transmitting coil at any point in space is derived. Then, a distribution map of the magnetic induction intensity in the magnetic field space is generated using the computer software Python. This map serves as a foundation for analyzing the mutual inductance coefficient between the transmitting coil and the receiving coil. It offers a theoretical reference for determining the positioning requirements between the transmitting coil and the receiving coil in the wireless charging system for electric vehicles.

Then, the mutual inductance system is analyzed and calculated. It can be observed that the maximum mutual inductance coefficient ( $M$ ) between the transmitting coil and the receiving coil of the EV wireless charging system is highest near the center point of the transmitting coil, taken as the coordinate origin. The displacement of the two coils along the x-axis within 0.1 m still results in the maximum value of  $M$ . Similarly, a displacement along the y-axis within 0.01 m also yields the maximum value of  $M$ . However, when the horizontal displacement of the two coils exceeds the range of  $X \in [-0.1, +0.1]$ ,  $Y \in [-0.01, +0.01]$ , the  $M$  between the two coils decreases rapidly. Therefore, to achieve efficient wireless power transmission in the entire MCR-WPT system, it is essential to maximize the mutual inductance between the transmitting coil and the receiving coil.

Later, this chapter analyzes the random parking positions of elderly EV in the parking space to determine the range of random positions of the MCR-WPT receiving coil. It also calculates the distribution diagram of the mutual inductance coefficient between the transmitting coil and the receiving coil in detail as the relative positions of the transmitting coil and the receiving coil change within this range. Finally, the distribution position of the maximum mutual inductance coefficient is deduced.

This material is reserved for educational use only, not allowed for commercial use.

Forbidden to modify the content, and cite the document when use.

This chapter is structured as follows. In Section 3.1, we analyzed the problem of alignment between the transmitting coil and receiving coil in the existing WPT system. In section 3.2, we explained the working principle of the WPT system. In Section 3.3, we analyzed and established the mathematical model of the magnetic field for the transmitting coil. In Section 3.4, we analyzed the magnetic field distribution diagram for the transmitting coil. In Section 3.5, we analyzed the range of WPT magnetic field. In Section 3.6, we analyzed and established the mathematical analysis of mutual inductance. In section 3.7, we theoretically calculated the mutual inductance corresponding to the scenario where the receiving coil randomly falls at any point in the magnetic field.

### 3.1 The Problems in WPT system of EV

In the previous chapter, the fundamental dynamic parameters of the elderly EV, along with the essential parameters of driving motors and power batteries, have been analyzed. This analysis lays the groundwork for the subsequent design of a wireless charging system and a wireless charging automatic alignment device for electric vehicles intended for the elderly.

The wireless charging technology for electric vehicles transmits power to the power pick-up mechanism located at the receiving end of the vehicle, which operates within a specific range above the ground. This is achieved through a power transmission coil buried or installed on the ground, in the form of a high-frequency alternating magnetic field. This process supplies power to the vehicle's energy storage equipment. The energy transfer efficiency of the wireless charging system for electric vehicles is highly dependent on the positioning relationship between the radiation ring and the receiving coil. When the centers of the two are aligned, the system can achieve the highest transmission power and efficiency. When the offset exceeds a certain range, the transmission power and efficiency of the system will be significantly reduced [26].

However, the current wireless charging technology for electric vehicles is not perfect, leading to breakthroughs in key charging capacity parameters, such as the automatic alignment of the primary and secondary coils. Currently, the solution to this technical issue involves continuously moving the vehicle with the receiving coil to achieve optimal alignment with the transmitting coil. This approach reduces the

This material is reserved for educational use only, not allowed for commercial use.

Forbidden to modify the content, and cite the document when use.

distance of power transmission, enhances power, and improves efficiency. In the case of elderly electric vehicles, users, particularly the elderly, may need to move and adjust the vehicle multiple times to align the receiving coil on the vehicle with the underground power transmission coil. This method is very complicated, especially for the elderly.

The next problem to be solved is the automatic alignment of the transmitting coil and receiving coil for electric vehicle wireless charging. Finally, after the electric vehicle enters the charging parking space, the power supply transmitting coil under the ground and the receiving coil installed on the vehicle can automatically adjust to the optimal charging position without the need for repeated adjustments to the vehicle's position. That is, we need to design a wireless power transfer automatic alignment device, abbreviated as WPT-AAD. This is also the focus of this research.

### 3.2 The working principle for WPT system

The wireless charging system designed in this thesis for the elderly EV is a magnetic coupling resonance wireless power transmission system (MCR-WPT). The overall system composition is shown in Figure 3-2-1. The working principle of the system involves several components: a rectifier filter circuit, a high-frequency inverter circuit, a driving circuit, a control circuit, a signal feedback mutual inductor, a resonant capacitor, transmission coil, receiving coil, high-frequency rectifier, and load. These components work together to convert municipal power into direct current. Among them, the 220V municipal power input is filtered by a rectifier to obtain DC voltage. Subsequently, the full bridge inverting circuit is utilized to generate specific frequency AC for the launch coil. The launch coil and the receiving coil form two LC resonant circuits with their respective resonant capacitances. By designing the physical parameters and the resonant capacitance values of the two coils, the inherent frequency of the coils matches the operating frequency of the system, enabling the system to operate in a resonant state. Magnetic field coupling resonance occurs between the transmitting coil and the receiving coil, generating a high-frequency alternating magnetic field. The alternating magnetic field radiates to the receiving coil, which generates an inductive current, enabling wireless transmission of energy. [27].

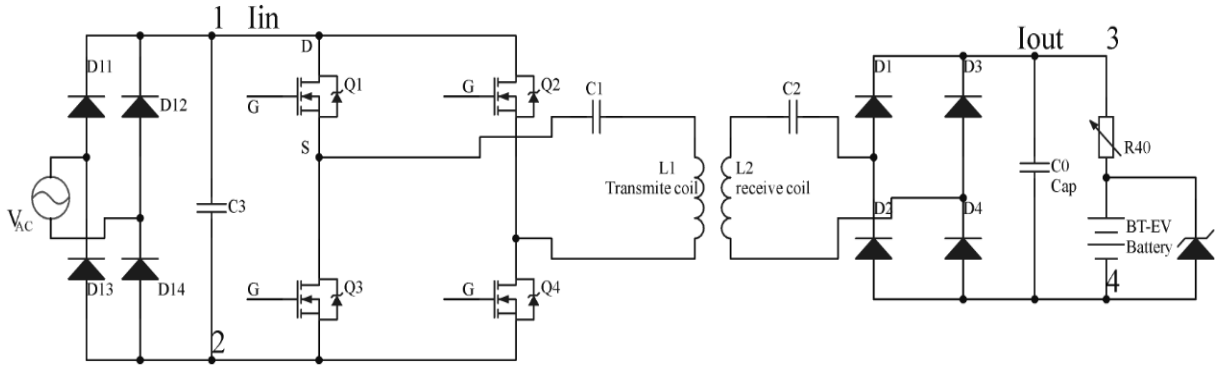


Fig.3-2-1 MCR-WPT system composition structure diagram [27]

As shown in the figure above, the circuit diagram illustrates the composition of the MCR-WPT system. In order to facilitate measurement and system control, the power loss from the mains  $V_{ac}$  to the rectifying and filtering part is very small, and it is ignored in this thesis. Therefore, the total input power ( $P_{in}$ ) of the system can be calculated by measuring the voltage ( $U_i$ ) between points "1" and "2" and the current ( $I_i$ ) flowing through "1".

$$P_{in} = U_i \times I_i \quad (3-2-1)$$

The total output power ( $P_{out}$ ) of an MCR-WPT system can be calculated by measuring the voltage ( $U_o$ ) between points "3" and "4" and the current ( $I_o$ ) flowing through "3".

$$P_{out} = U_o \times I_o \quad (3-2-2)$$

From the perspective of energy conservation, considering the loss power  $P_{inverter}$  of the high-frequency inverter circuit and the loss power  $P_{rectifier}$  of the high-frequency rectifier filter circuit, the total output power formula of the MCR-WPT system can be obtained.

$$P_{out} = (P_{in} - P_{inverter} - P_{rectifier}) \cdot \eta_{coil} \quad (3-2-3)$$

where,

$P_{out}$ , is the total output power of MCR-WPT system, (kW);

$P_{in}$ , is the total input power of MCR-WPT system, (kW)

This material is reserved for educational use only, not allowed for commercial use.

Forbidden to modify the content, and cite the document when use.

$P_{inverter}$ , refers to the power loss in the high-frequency inverter circuit, (kW), primarily, associated with the factory parameters, current, voltage, and frequency of the MOSFET.

$P_{rectifier}$ , It refers to the power loss in the high-frequency rectifier filter circuit, which is primarily associated with the factory parameters, current, voltage, and frequency of the rectifier diode, (kW).

$\eta_{coil}$ , Is the efficiency of the resonance unit

Since the proportion of  $P_{inverter}$  and  $P_{rectifier}$  is very small and changes little during system operation, they can be ignored for accurate calculations. Therefore, the following formula can be obtained. [28]

$$\eta_{coil} \approx \frac{P_{out}}{P_{in}} = \frac{U_o I_o}{U_i I_i} = \eta \quad (3-2-4)$$

When the MCR-WPT system operates in the fully resonant state, the efficiency  $\eta$  of MCR-WPT can be expressed as follows.

$$\eta \approx \eta_{coil} = \frac{\omega_d^2 M^2 R_L}{(R_2 + R_L)(\omega_d^2 M^2 + R_1 R_L + R_1 R_2)} \quad (3-2-5) [28]$$

where,

$M$ , mutual inductance coefficient between transmitting coil and receiving coil;

$R_L$ , equivalent load at the output end of the resonance unit at the receiving end;

$R_1$ , represents the series equivalent resistance of the equivalent resistance of the transmitting coil and the AC equivalent resistance of the compensation capacitor;

$R_2$ , represents the series equivalent resistance of the equivalent resistance of the receiving coil and the AC equivalent resistance of the compensation capacitor

$\omega_d$ , is the driving angular frequency of the high-frequency inverter when the system operates in the fully resonant state;

$\eta_{coil}$ , Is the efficiency of the whole resonance unit

$\eta$ , efficiency of the whole MCR-WPT system; Since  $\eta_{coil} \approx \eta$ , In the following,  $\eta$  and  $\eta_{coil}$  are not distinguished.

It can be inferred from the above formula that the input and output power of the resonance unit are closely interrelated. They are directly proportional to the input

DC voltage of the high-frequency inverter and are influenced by the coil mutual

This material is reserved for educational use only, not allowed for commercial use.

Forbidden to modify the content, and cite the document when use.

inductance, equivalent resistance, load resistance, and driving frequency. The ratio of the output power to the input power of the resonance unit determines the efficiency of the resonance unit. Efficiency is a crucial indicator of the radio energy transmission system and energy utilization rate. It is independent of the input DC voltage and is related to the coil's mutual inductance, equivalent resistance, load resistance, and driving frequency.

The equivalent resistance and driving frequency are determined by the design of the resonant unit. The load resistance is determined by the charged battery. The mutual inductance coefficient of the coil is related to the structural shape of the coil and the relative position of the two coils [11]. In order to more easily see the relationship between  $\eta$  and mutual inductance  $M$ , the expression of  $\eta$  is transformed into the following formula:

$$\frac{1}{\eta} = 1 + \frac{R_2}{R_L} + \frac{(R_2 + R_L)(R_1 R_L + R_1 R_2)}{\omega_d^2 M^2 R_L} \quad (3-2-6)$$

From the above formula, it can be seen that  $\eta$  is positively related to coil mutual inductance  $M$  and angular frequency  $\omega_d$ . When  $M$  or  $\omega_d$  increases,  $\eta$  also increases.

From the introduction in Chapter 1, despite the fact that researchers and specialists from all over the world have conducted extensive research on MCR-WPT, we discovered no precise analysis of the  $M$  between the transmitting and receiving coils, nor a particularly specific mathematical model. As a result, it is vital to study the  $M$ .

From the above analysis, it can be seen that when the total input power  $P_{in}$  of the MCR-WPT system is determined, the efficiency  $\eta$  of the MCR-WPT system must be improved to improve the total output power  $P_{out}$  of the MCR-WPT system; To improve the  $\eta$ , we can consider the improvement of the coil mutual inductance  $M$  and the angular frequency  $\omega_d$ ; However, the angular frequency  $\omega_d$  is determined by the natural frequency of the resonance unit and is directly related to the parameters of the coil inductance coefficient, resonance capacitance and other electrical components of the resonance unit. When these electrical parameters are determined, the resonance frequency is also determined; Therefore, only the coil mutual

inductance ( $M$ ) is left to be the direction of efforts to improve the efficiency  $\eta$  of the resonance unit and thus to improve the total output power  $P_{out}$  of the entire MCR-WPT system [29].

It can be seen that the  $M$  is one of the main factors affecting the overall efficiency of the MCR-WPT system. The mathematical expression of  $M$  can be obtained from its definition as follows:

$$M = \frac{\Phi}{I} \quad (3-2-7) [30]$$

where,

$I$ , is the current passing through the transmitting coil;

$M$ , is the mutual inductance coefficient between the transmitting coil and the receiving coil;

$\Phi$ , is the magnetic flux generated by the transmitting coil surrounded by the receiving coil;

The magnetic flux ( $\Phi$ ) is affected by factors such as the relative position between the two coils, the shape of the coil [30], which in turn affects the  $M$ . In order to improve the efficiency of the WTP system, the  $\Phi$  must be increased. In this thesis, the coil's shape is designed with reference to [31], and this influencing factor is determined. Therefore, it is necessary to study the impact of the relative position between the two coils.

### 3.3 mathematical model of magnetic field for transmitting coil

As shown in the figure, according to formula (3-3-1), Biot Savart law [32], through geometric analysis and mathematical operation, as shown in Fig.3-3-2, the magnetic induction intensity generated by a section of current carrying straight wire AB at any point P (x, y, z) in its magnetic field space is as shown in formula (3-3-2).

$$d\vec{B} = \frac{\mu_0}{4\pi} \frac{Id\vec{l} \times \hat{r}}{r^2} \quad (3-3-1)$$

$$B = \frac{\mu_0 I}{4\pi r} (\cos \alpha_1 - \cos \alpha_2) \quad (3-3-2)$$

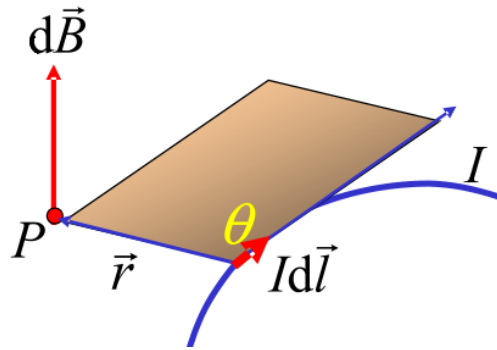


Fig.3-3-1 The magnetic induction intensity produced by an electrified wire at any point around it [32]

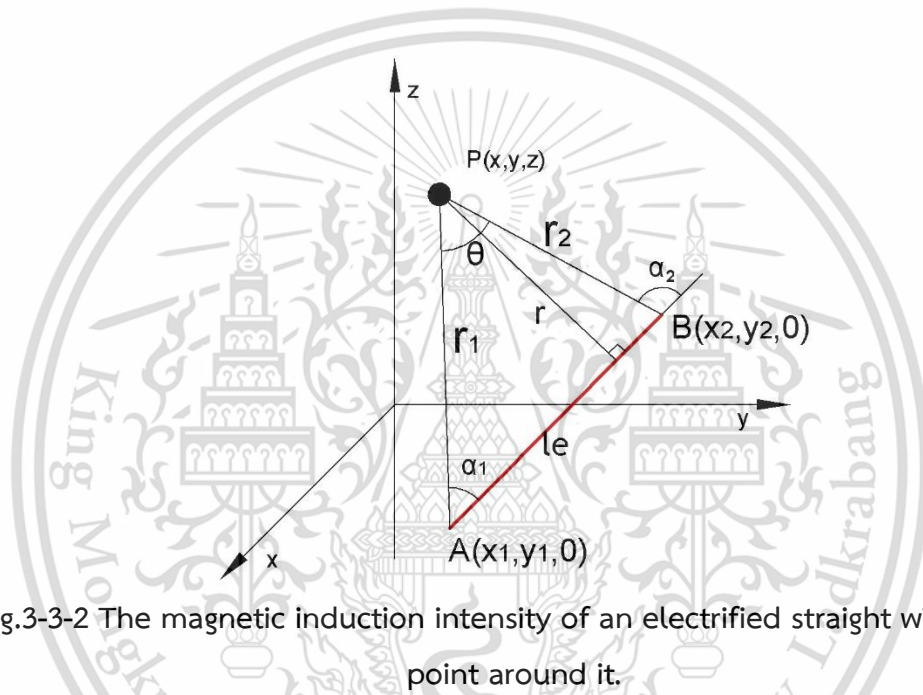


Fig.3-3-2 The magnetic induction intensity of an electrified straight wire at any point around it.

Where, the length of the current-carrying conductor AB is " $l_e$ ," and the vectors from point P to both ends of the conductor A and B are " $r_1$ " and " $r_2$ ," respectively. The direction of the magnetic induction intensity at point P and the cross product of " $r_1$ " and " $r_2$ " is the same, following the right-hand rule for vector multiplication.

After mathematical calculations, the three components of magnetic induction intensity at point P in the X, Y, and Z directions can be obtained. [32]:

$$B_{x-AB} = \frac{\mu_0 I z (y_2 - y_1)}{4\pi r} \left( \frac{D_1}{r_1} + \frac{D_2}{r_2} \right) \quad (3-3-3)$$

$$B_{y-AB} = \frac{\mu_0 I z (x_1 - x_2)}{4\pi r} \left( \frac{D_1}{r_1} + \frac{D_2}{r_2} \right) \quad (3-3-4)$$

$$B_{z-AB} = \frac{\mu_0 I (x_1 y_2 - x_2 y_1 + x y_1 - x_1 y + x_2 y - x y_2)}{4\pi r} \left( \frac{D_1}{r_1} + \frac{D_2}{r_2} \right) \quad (3-3-5)$$

This material is reserved for educational use only, not allowed for commercial use.

Forbidden to modify the content, and cite the document when use.

where,  $r$ ,  $D_1$  and  $D_2$  are respectively calculated by the following formula:

$$r = [(x_1 - x_2)^2 + (y_1 - y_2)^2]z^2 + [(y_1 - y_2)x - (x_1 - x_2)y + (x_1y_2 - x_2y_1)]^2$$

$$D_1 = [(x_1^2 + y_1^2) - (x_1 - x_2)x - (y_1 - y_2)y - (x_1x_2 + y_1y_2)]$$

$$D_2 = [(x_2^2 + y_2^2) - (x_2 - x_1)x - (y_2 - y_1)y - (x_1x_2 + y_1y_2)]$$

For the rectangular coil, as shown in Fig. 3-3-3, the current-carrying rectangular coil with length  $a$  and width  $b$  can be considered as the vector superposition of the magnetic field generated by four sections of wires. The component  $B_{z-rectangle}$  of the magnetic induction intensity generated by any point  $P(x, y, z)$  in the magnetic field space in the  $Z$  direction is expressed as. [32]

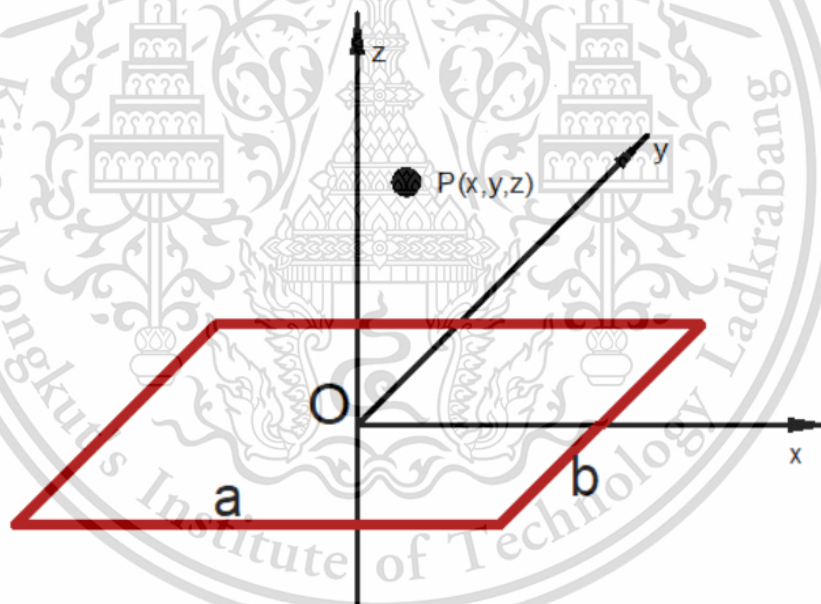


Fig.3-3-3 The magnetic induction intensity produced by an electrified quadrilateral at any point around it.[32]

$$B_{z-rectangle} = \frac{\mu_0 I (b-y)}{4\pi [z^2 + (b-y)^2]} \left( \frac{a-x}{\sqrt{(x-a)^2 + (y-b)^2 + z^2}} + \frac{a+x}{\sqrt{(x+a)^2 + (y-b)^2 + z^2}} \right) + \frac{\mu_0 I (a+x)}{4\pi [z^2 + (a+x)^2]} \left( \frac{b-y}{\sqrt{(x+a)^2 + (y-b)^2 + z^2}} + \frac{b+y}{\sqrt{(x+a)^2 + (y+b)^2 + z^2}} \right) + \frac{\mu_0 I (b+y)}{4\pi [z^2 + (b+y)^2]} \left( \frac{a+x}{\sqrt{(x+a)^2 + (y+b)^2 + z^2}} + \frac{a-x}{\sqrt{(x-a)^2 + (y+b)^2 + z^2}} \right)$$

This material is reserved for educational use only, not allowed for commercial use.

Forbidden to modify the content, and cite the document when use.

$$+ \frac{\mu_0 I (a-x)}{4\pi [z^2 + (a-x)^2]} \left( \frac{b+y}{\sqrt{(x-a)^2 + (y+b)^2 + z^2}} + \frac{b-y}{\sqrt{(x-a)^2 + (y-b)^2 + z^2}} \right) \quad (3-3-6)$$

where,

$\mu_0$  is the permeability in vacuum,  $\mu_0 = 4\pi \times 10^{-7}$ , unit: T-m/A;

The permeability in the air is close to the vacuum permeability, and the vacuum permeability can often be directly used in the calculation[33];

$I$  is the current intensity passing through the coil, unit A;

$a, b$  is the length and width of the coil, unit m;

$B_{z-rectangle}$  is the magnetic induction intensity of point P in space in the Z direction, unit T;

### 3.4 Magnetic field distribution diagram for transmitting coil

The elderly EV wireless charging system studied in this thesis is the MCR-WPT system. The magnetic coupling resonance mechanism of the system mainly consists of a transmitting coil and a receiving coil. The transmitting coil generates a magnetic field due to the exciting current, while the receiving coil produces induced electromotive force in response to the changing magnetic field. [10]

The transmitting coil is installed on the ground, and the receiving coil is installed under the vehicle chassis. When working, the two are approximately parallel. According to the principle of induced electromotive force generation, only the component  $B_z$  perpendicular to the plane of the receiving coil can form the effective magnetic flux.

As shown in Fig.3-4-1, the shape of the coil is similar to that of the rectangular coil, which is designed with a circumference of 8. The coil measures 650×500 mm, with an inner space size of about 350×200 mm. The average width of each turn is approximately 37.5 mm (0.0375 m). It is equivalent to the magnetic field formed by vector superposition in space of 8 rectangular coils of different sizes carrying the same current. The coil is wound with two wires, and both wires collectively carry the current intensity. For the convenience of calculation, first calculate according to the single wire, and then multiply the calculation result by 2 to obtain the total magnetic induction intensity generated by the transmitting coil at any point in space.

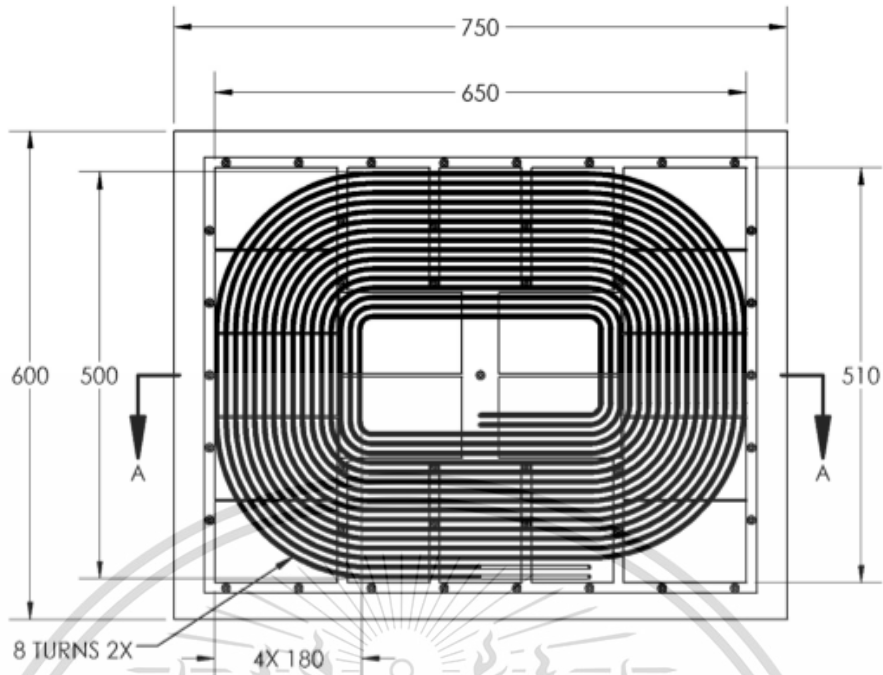


Fig.3-4-1 planar graph of transmitting coil [31]

According to the calculation method of the magnetic induction intensity of the rectangular coil described in the previous section, the formula for calculating the magnetic induction intensity component  $B_z$  generated in space by the WPT transmitting coil wound with 8 turns in the above figure is as follows.

$$\begin{aligned}
 B_z = 2 \times \sum_{i=0}^7 \left\{ \frac{\mu_0 I ((W-gi)-y)}{4\pi [z^2 + ((W-gi)-y)^2]} \left( \frac{(L-gi)-x}{\sqrt{(x-(L-gi))^2 + (y-(W-gi))^2 + z^2}} \right. \right. \\
 + \left. \left. \frac{L-gi+x}{\sqrt{(x+(L-gi))^2 + (y-(W-gi))^2 + z^2}} \right) \right. \\
 + \frac{\mu_0 I (L-gi+x)}{4\pi [z^2 + (L-gi+x)^2]} \left( \frac{W-gi-y}{\sqrt{(x+L-gi)^2 + (y-(W-gi))^2 + z^2}} \right. \\
 + \left. \left. \frac{W-gi+y}{\sqrt{(x+L-gi)^2 + (y+W-gi)^2 + z^2}} \right) \right. \\
 + \frac{\mu_0 I (W-gi+y)}{4\pi [z^2 + (W-gi+y)^2]} \left( \frac{L-gi+x}{\sqrt{(x+L-gi)^2 + (y+W-gi)^2 + z^2}} \right. \\
 + \left. \left. \frac{L-gi-x}{\sqrt{(x-(L-gi))^2 + (y+W-gi)^2 + z^2}} \right) \right. \\
 + \left. \frac{\mu_0 I (L-gi-x)}{4\pi [z^2 + (L-gi-x)^2]} \left( \frac{W-gi+y}{\sqrt{(x-(L-gi))^2 + (y+W-gi)^2 + z^2}} \right. \right. \\
 + \left. \left. \frac{W-gi-y}{\sqrt{(x-(L-gi))^2 + (y-(W-gi))^2 + z^2}} \right) \right\} \quad (3-4-1)
 \end{aligned}$$

This material is reserved for educational use only, not allowed for commercial use.

Forbidden to modify the content, and cite the document when use.

where,

$\mu_0$  is the permeability in vacuum,  $\mu_0=4\pi\times 10^{-7}$ , unit: T-m/A;

The permeability in air is close to vacuum permeability, so vacuum permeability can be directly used in calculation; [33].

" $I$ " is the current intensity passing through the coil, unit A;

$L$ 、 $W$ , are the length and width of the transmitting coil, unit m; In this thesis, calculated from Figure 3-4-1, 0.65m and 0.50m are taken respectively;

$g$  is the average line width of each cycle of the coil, calculated from Figure 3-4-1, taken as 0.0375m in this thesis;

$i$  is the cumulative ordinal number; calculated from Figure 3-4-1, Initial value  $i=0$ ,  $i=i+1\leq 7$ ;

$B_z$  is the magnetic induction intensity of point P in space in the Z direction, unit T; For the positioning research of WPT, we focus on the spatial distribution of the effective magnetic induction component  $B_z$  of the magnetic field generated by the transmitting coil.

If a 20 A current is applied to the coil, formula (3-4-1) can be used to calculate a specific value for the magnetic induction intensity at any point P in the magnetic field space. In this thesis, the magnetic field distribution generated by the transmitting coil is estimated to facilitate the identification of the optimal position of the receiving coil. The magnetic induction intensity distribution in multiple planes parallel to the transmitting coil is plotted using the computer programming language Python, with reference to formula (3-4-1).

magnetic intensity in XY plane with Z=0.20 I=20

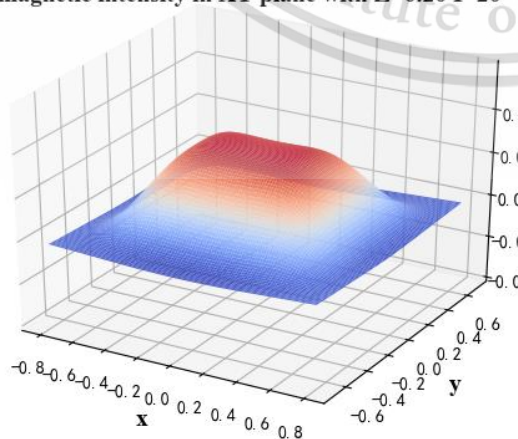


Fig.3-4-2  $B_z$  distribution map

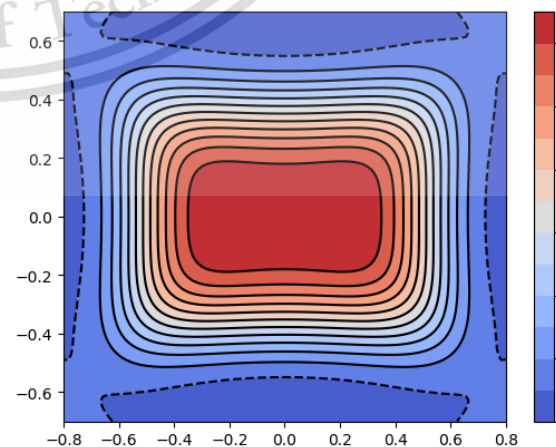


Fig.3-4-3  $B_z$  distribution contour map.

(Z=0.20 I=20).

(Z=0.20 I=20).

magnetic intensity in XY plane with Z=0.20 I=-20

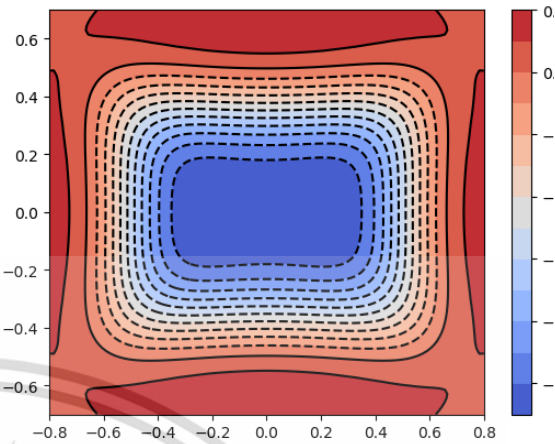
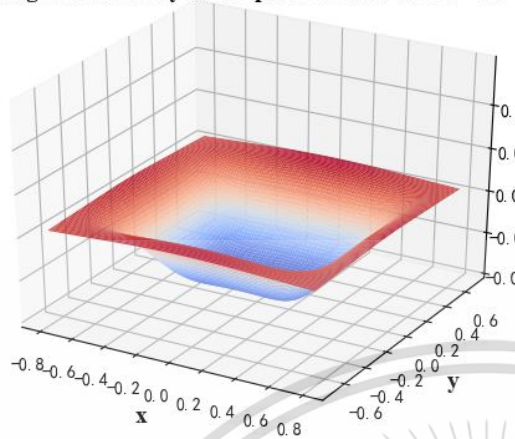


Fig.3-4-4 Bz distribution map

Fig.3-4-5 Bz distribution contour map

(Z=0.20 I=-20)

(Z=0.20 I=-20)

magnetic intensity in XY plane with Z=0.15 I=20

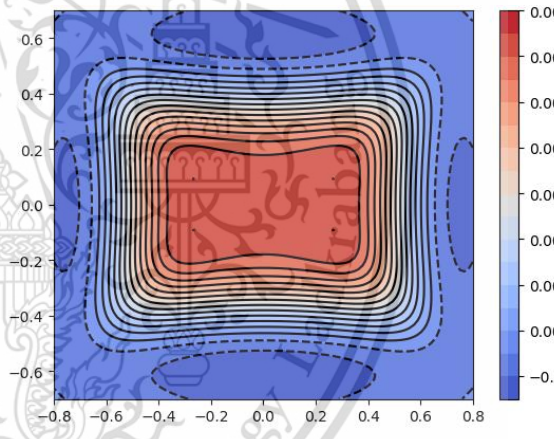
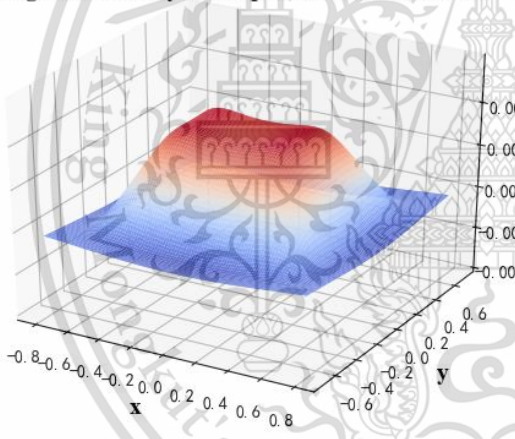
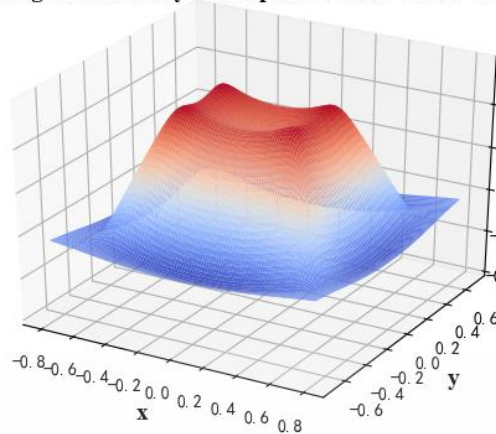
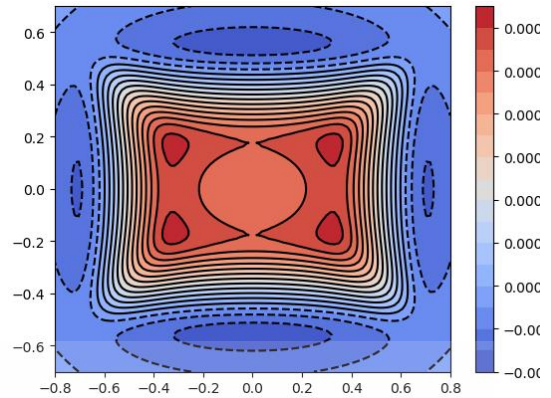


Fig.3-4-6 Bz distribution map

Fig.3-4-7 Bz distribution contour map

(Z=0.15 I=20)

(Z=0.15 I=20)

magnetic intensity in XY plane with  $Z=0.10$   $I=20$ Fig.3-4-8  $B_z$  distribution map  
( $Z=0.10$   $I=20$ )Fig.3-4-9  $B_z$  distribution contour map  
( $Z=0.10$   $I=20$ )

As shown in Fig. 3-4-2, Fig. 3-4-3 displays the distribution diagram of the effective magnetic induction intensity  $B_z$  in the XY plane directly above 20 cm from the transmitting coil and parallel to the transmitting coil when the transmitting coil carries 20 A forward current.

As shown in Fig. 3-4-4, Fig. 3-4-5 depicts the distribution diagram of the effective magnetic induction intensity  $B_z$  in the XY plane directly above 20 cm from the transmitting coil and parallel to the transmitting coil when the transmitting coil carries a reverse current of -20 A.

As shown in Fig. 3-4-6, Fig. 3-4-7 displays the distribution diagram of the effective magnetic induction intensity  $B_z$  in the XY plane directly above 15 cm and parallel to the transmitting coil when the transmitting coil is connected to 20 A forward current.

As shown in Fig. 3-4-8, Fig. 3-4-9 displays the distribution diagram of the effective magnetic induction intensity  $B_z$  in the XY plane directly above 10 cm and parallel to the transmitting coil when the transmitting coil is connected to 20 A forward current.

From the analysis of the above figures, it can be seen that the effective magnetic induction intensity  $B_z$  is mainly concentrated directly above the transmitting coil.  $B_z$  decreases rapidly outside the area deviated from the upper part of the opening. When a reverse current is applied to the transmitting coil, the direction of  $B_z$  is also reversed. As the distance between the receiving coil and the transmitting coil decreases from 20 cm to 15 cm and 10 cm, the magnitude of  $B_z$  increases rapidly. However, the uniformity of effective magnetic induction intensity distribution on the same plane

decreases.

By analyzing the distribution of effective magnetic induction  $B_z$  in space, it can be estimated that the receiving coil of a WPT system should be positioned directly above the transmitting coil and coaxial with the center line of the transmitting coil to receive the maximum effective magnetic flux. Additionally, the effective magnetic induction  $B_z$  increases as the receiving coil gets closer to the transmitting coil. The research on the spatial distribution of effective magnetic induction  $B_z$  provides a theoretical basis for the design of WPT system positioning.

### 3.5 Analysis range of WPT magnetic field

In the previous section, the magnetic field distribution generated by the transmitting coil of the WPT system has been analyzed. It is clearly known that the receiving coil should be positioned directly above the transmitting coil and coaxial with the center line of the transmitting coil to receive the maximum effective magnetic flux. However, aligning the transmitting coil by adjusting the vehicle position poses a significant challenge for elderly drivers in parking technology.

The following is a set of automatic alignment devices designed to solve this problem. The driver only needs to park the car in the designated parking space for it to be charged. The charging alignment device can automatically align the transmitting coil with the receiving coil, eliminating the need for the driver to repeatedly adjust the position of the car.

According to the analysis in the second chapter, the dimensions of the elderly car designed in this thesis are  $2488 \times 1506$  mm. According to the standard parking space size design method, the length and width are increased by 1000 mm and 800 mm respectively based on the size of the car, and rounded to the nearest integer. Therefore, the parking space size designed for this specific elderly car in this study is  $3480 \times 2300$  mm.

The transmitting coil designed in this thesis is shown in Fig. 3-4-1. The shape of the coil is approximately rectangular, with dimensions of  $650 \times 500$  mm. The receiving coil designed in this thesis is shown in Fig. 4-2-1. The coil shape is approximately square, with dimensions of  $350 \times 350$  mm.

This material is reserved for educational use only, not allowed for commercial use.

Forbidden to modify the content, and cite the document when use.

As depicted in the figure, it shows a schematic diagram of the EV parking at the limit position in the upper right corner. This diagram can indicate the limit position in the upper right corner relative to the center point of the on-board receiving coil. Similarly, when the vehicle is parked at the lower left corner limit position, the lower left corner limit position of the center point of the on-board receiving coil can be identified. By using this drawing method, the active range for the center point of the receiving coil can be illustrated.

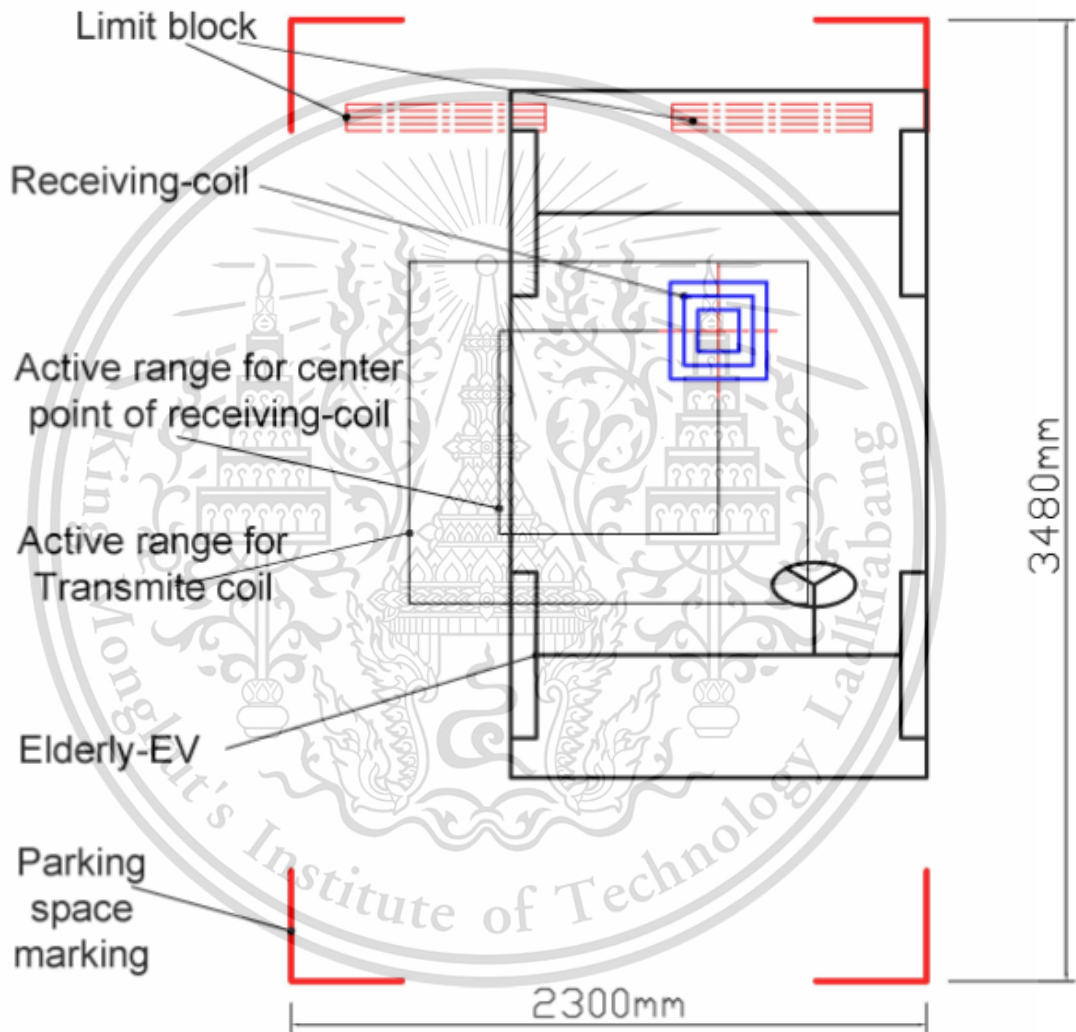


Fig.3-5-1 Schematic diagram of the EV parking at the limit position in the upper right corner

From the above analysis of the distribution range of the magnetic field generated by the transmitting coil, it can be estimated that the optimal position for wireless charging occurs when the transmitting coil is aligned with the center of the receiving coil. Therefore, the active range for the center point of the receiving coil

This material is reserved for educational use only, not allowed for commercial use.

depicted in the above figure is also the active range for the center point of the transmitting coil. Based on this active range, expand it to accommodate the volume of the transmitting coil, resulting in an active range for the entire transmitting coil of 1444mm × 1236 mm, as illustrated in the figure below.

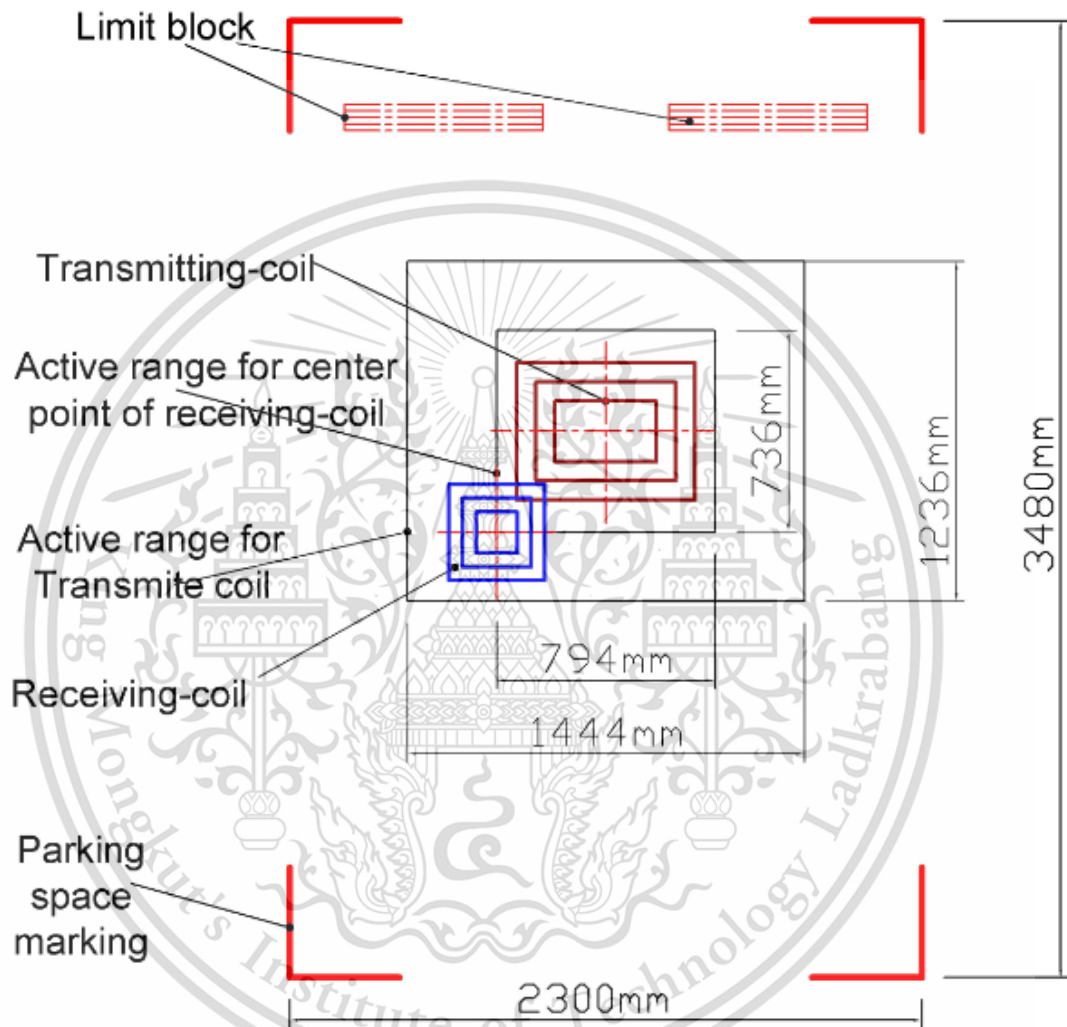


Fig.3-5-2 Schematic diagram of active range of transmitting coil

When the elderly EV parks randomly in a parking space marked with the center point of the receiving coil, the center point of the receiving coil falls randomly into the active range, as shown in the figure. The transmitting coil is initially positioned at the center point, which serves as the origin of the marking system. The limit position of the random situation is as shown in the figure above. The receiving coil is positioned at one of the four corners, and the value range of the coordinates  $(x_0, y_0)$  of the central point of the receiving coil is.

$$x_0 \in [-794/2, +794/2], y_0 \in [-736/2, +736/2] \quad (3-5-1)$$

This material is reserved for educational use only, not allowed for commercial use.

Forbidden to modify the content, and cite the document when use.

Unit: mm

After calculation, it is obtained that,  $x_0 \in [-397,+397]$ ,  $y_0 \in [-368,+368]$ .

### 3.6 Mathematical analysis of mutual inductance

This chapter focuses solely on the positioning design of WPT. Therefore, it is essential to pay attention only to the effective magnetic flux of the receiving coil, rather than voltage, current, excitation frequency, etc.

In order to simplify the writing and calculations, start by calculating the effective magnetic flux enclosed by the outermost perimeter of the receiving coil. This can be achieved through a double integration of equation (3-4-1).

$$\Phi = \iint_D f(x, y) dx dy \quad (3-6-1)$$

where,

$f(x, y) = B_z$ , as seen in formul (3-4-1).

$\Phi$  Is the effective magnetic flux formed by the magnetic induction component in the z-axis direction (Wb,  $1\text{Wb}=1\text{T}\cdot\text{m}^2$ ).

$D$  is an integral closed region:

$$x_0 - \frac{l}{2} \leq x \leq x_0 + \frac{l}{2} \quad ; \quad y_0 - \frac{h}{2} \leq y \leq y_0 + \frac{h}{2}$$

$l, h$ , are the length and width of the receiving coil (m).

$a, b$ , are the length and width of the transmitting coil respectively;

$$-a/2 < X_0 < a/2 \quad \quad \quad -b/2 < Y_0 < b/2$$

The receiving coil designed in this thesis is shown in the figure below. Since the area surrounded by the coil decreases uniformly from the outer to the inner side, the integral area of each loop is successively reduced for integration. By summing these reductions, the total effective magnetic flux within all the coils wound for  $n$  cycles of the receiving coil can be accurately calculated.

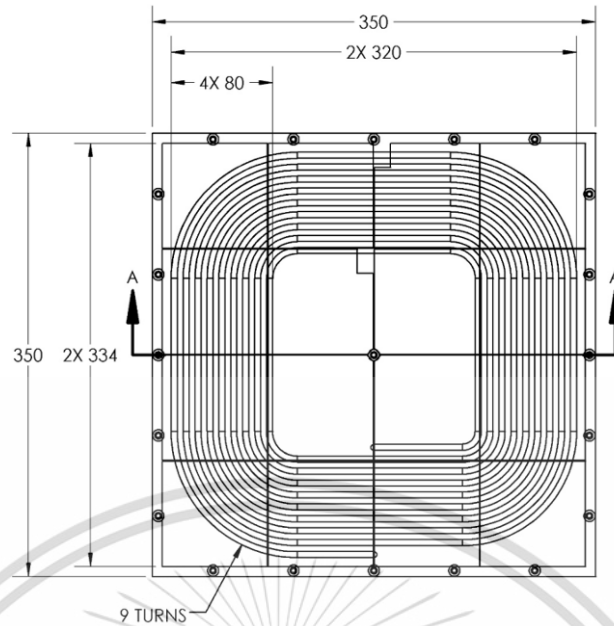


Fig.3-6-1 planar graph of receiving coil [31]

According to the mutual inductance of the coil, the received magnetic flux ( $\Phi$ ) can be defined by the mutual inductance coefficient  $M$  divided by the current  $I$  passing through the transmitting coil. Combined with the above calculation of magnetic flux, the expression of the  $M$  between the receiving coil and the transmitting coil can be obtained as follows.

$$\begin{aligned}
 M = 2 \times \sum_{j=0}^8 \{ \iint_{D_j} \sum_{i=0}^7 \{ & \\
 \frac{\mu_0((W-gi)-y)}{4\pi[z^2+((W-gi)-y)^2]} \left( \frac{(L-gi)-x}{\sqrt{(x-(L-gi))^2+(y-(W-gi))^2+z^2}} \right. & \\
 \left. + \frac{L-gi+x}{\sqrt{(x+(L-gi))^2+(y-(W-gi))^2+z^2}} \right) & \\
 + \frac{\mu_0(L-gi+x)}{4\pi[z^2+(L-gi+x)^2]} \left( \frac{W-gi-y}{\sqrt{(x+L-gi)^2+(y-(W-gi))^2+z^2}} \right. & \\
 \left. + \frac{W-gi+y}{\sqrt{(x+L-gi)^2+(y+W-gi)^2+z^2}} \right) & \\
 + \frac{\mu_0(W-gi+y)}{4\pi[z^2+(W-gi+y)^2]} \left( \frac{L-gi+x}{\sqrt{(x+L-gi)^2+(y+W-gi)^2+z^2}} \right. & \\
 \left. + \frac{L-gi-x}{\sqrt{(x-(L-gi))^2+(y+W-gi)^2+z^2}} \right) & \\
 + \frac{\mu_0(L-gi-x)}{4\pi[z^2+(L-gi-x)^2]} \left( \frac{W-gi+y}{\sqrt{(x-(L-gi))^2+(y+W-gi)^2+z^2}} \right. & \\
 \left. + \frac{W-gi-y}{\sqrt{(x-(L-gi))^2+(y-(W-gi))^2+z^2}} \right) \} dx dy \} & \quad (3-6-2)
 \end{aligned}$$

This material is reserved for educational use only, not allowed for commercial use.

Forbidden to modify the content, and cite the document when use.

where,

$D_j$  is the integral closed region:

$$x_0 - \frac{l}{2} + jr \leq x_j \leq x_0 + \frac{l}{2} - jr \quad (3-6-3)$$

$$y_0 - \frac{h}{2} + jr \leq y_j \leq y_0 + \frac{h}{2} - jr \quad (3-6-4)$$

$M$  is the mutual inductance coefficient of transmitting coil and receiving coil;

$\mu_0$  is the permeability in vacuum,  $\mu_0 = 4\pi \times 10^{-7}$ , unit: T-m/A. The permeability in air is close to vacuum permeability, so vacuum permeability can be directly used in calculation [33].

$L$ 、 $W$  is the length and width of the transmitting coil, unit m; In this thesis, 0.65m and 0.50m are taken respectively.

$g$  is the average interval width of each turn of the transmitting coil, which is taken as 0.0375m in this thesis.

$r$  is the average interval width of each turn of the receiving coil, which is taken as 0.009m in this thesis.

$i, j$  is the cumulative ordinal number, initial value  $i=0$ , step=1,  $i \leq 7$ ,  $j \leq 8$ .

$l, h$  is the length and width of the receiving coil (m), which is taken as 0.35m and 0.35m respectively in this thesis;

$(x_0, y_0)$  is the center of the receiving coil. In order to help understand  $x_0, y_0, j, r$ , a special drawing is drawn to help understand.

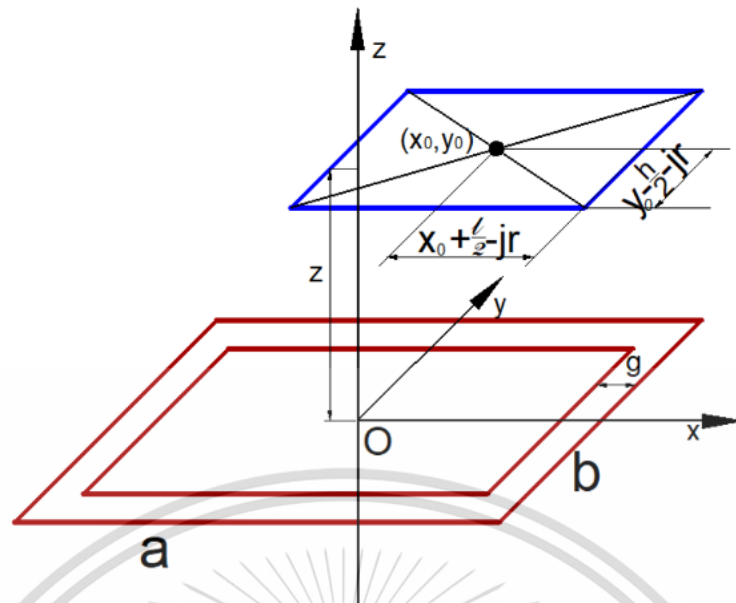


Fig.3-6-2 Illustration of calculation parameters

According to the analysis in the previous section, the value range of  $(x_0, y_0)$  is  $x_0 \in [-0.397, +0.397]$ ,  $y_0 \in [-0.368, +0.368]$ , and the unit is meter "m". When  $(x_0, y_0)$  takes an appropriate value, the mutual inductance  $M$  will have a maximum value.

### 3.7 Calculation of mutual inductance

From Equation (3-6-2), it can be predicted that when the center of the receiving coil  $(x_0, y_0, Z)$  takes any value within the defined range, the mutual inductance  $M$  between the receiving coil and the transmitting coil is very complex. This calculation must be performed using a computer program. The program flowchart is as follows.

The pseudo code of the program is as follows:

---

The pseudocode for calculating the  $M$

---

- 1 Begin
- 2 Scientific computing module
- 3 Define the calculation range, variables and parameters
- 4      $L, W, \text{pai}, u_0, d$
- 5 Define function  $F(x, y)$
- 6 Define function  $\text{FBz}(x, y)$ :
- 7     for  $i$  in range(0,8):
- 8          $\text{Bz} = \text{Bz} + F(x, y)$
- 9          $L = L - 0.0375$

---

This material is reserved for educational use only, not allowed for commercial use.

Forbidden to modify the content, and cite the document when use.

---

```

10         W = W - 0.0375
11     return Bz
12     end for
13     Define integral function INF(x0,y0)
14         l=0.35, h = 0.35, r=0.009
15     # Length, width and step of receiving coil
16     for j in range (0,9):
17         #Superimpose the magnetic flux surrounded
18         by each turn of receiving coil
19         xDlimit=x0-l/2+jr,
20         xUplimit=x0+l/2-jr
21         yDlimit=y0-h/2+jr
22         yUplimit=y0+h/2-jr
23         Fi=Fi+integrate.nquad(FBz (x,y), [[xDlimit,
24         xUplimit], [yDlimit,yUplimit]])
25     Return Fi
26     end for
27     Define the value range of x0 and y0:
28     x0 ∈ [-0.397,+0.397], y0 ∈ [-0.368, +0.368]
29     for p in range(0,100):
30         for q in range (0,100):
31             Fi = INF (x0[p, q],y0[p,q])
32         #Loop call INF function for integral operation
33         Fi_list.append(Fi)
34     end for
35     Fi_array=array(Fi_list)
36     Plot(x0,y0, Fi_array)
37     end

```

---

In this thesis, Python software is utilized to develop a calculation program for determining the distribution diagram of mutual inductance ( $M$ ) between two coils. The calculation is based on the position  $(x_0, y_0)$  of the center point of the receiving coil in the vicinity of the XY plane, located 0.2 m above the transmitting coil.

This material is reserved for educational use only, not allowed for commercial use.

Forbidden to modify the content, and cite the document when use.

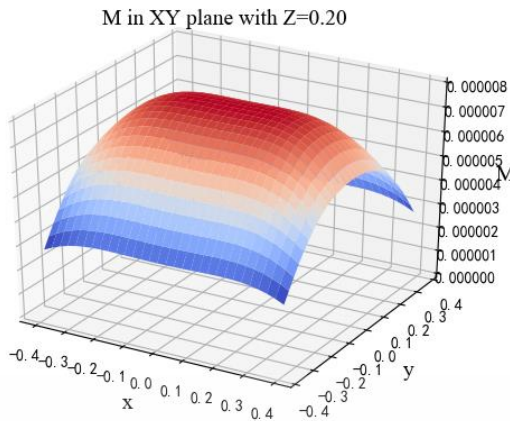


Fig.3-7-1 mutual inductance distribution map

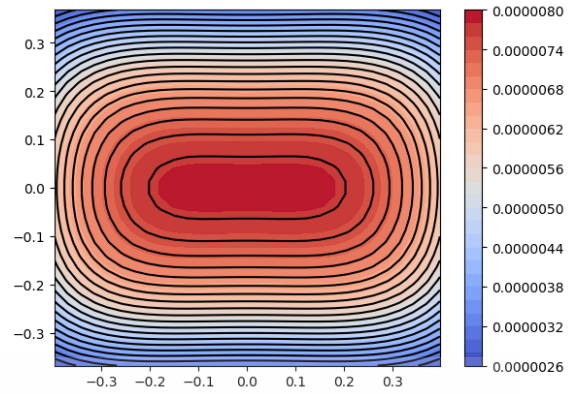


Fig.3-7-2 mutual inductance distribution contour map

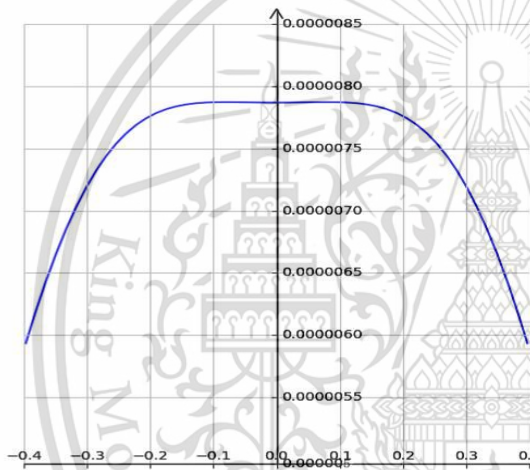


Fig.3-7-3 Y=0, X- mutual inductance graph

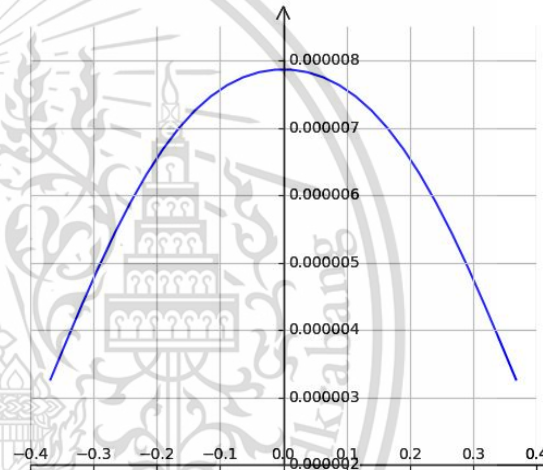


Fig.3-7-4 X=0, Y- mutual inductance graph

Graphic illustration:

The four figures above display the mutual inductance ( $M$ ) between two coils. The XY coordinate represents the location of the center point of the receiving coil, with the coordinate origin at the center point of the transmitting coil. The distance between the receiving coil and the transmitting coil above it is 0.2 m.

Fig. 3-7-1 and Fig. 3-7-2 show the continuous distribution of  $M$  in the area where  $x_0 \in [-0.397, +0.397]$ ,  $y_0 \in [-0.368, +0.368]$ , and  $z = 0.2$ .

Unit, meter, m.

Fig. 3-7-3 shows the M-X distribution curve along the middle segment parallel to the X-axis with  $y = 0$  and  $z = 0.2$  m;

Fig. 3-7-4 shows the  $M$ - $y$  distribution curve along the middle line segment parallel to the  $Y$ -axis with  $x = 0$  and  $z = 0.2$  m;

From the four figures above, it is evident that the mutual inductance ( $M$ ) of the two coils is at its maximum when the receiving coil is directly above the transmitting coil. Even when the receiving coil is slightly shifted about 0.10 m to the left or right along the  $x$ -axis direction, the  $M$  still remains close to its maximum value. However, when the receiving coil is moved in the  $y$ -axis direction while directly above the transmitting coil, the value of  $M$  decreases rapidly. This phenomenon is attributed to the impact of the rectangular structure of the transmitting coil.

By running the computer program using Python software, it was calculated that the maximum value of  $M$  is.

$$M_{max} = 7.87 \times 10^{-6} \text{ H} \quad (3-7-1)$$

This chapter examines the distribution of mutual inductance between the transmitting coil and the receiving coil in space. This analysis provides a theoretical foundation for designing the positioning of MCR-WPT system.

## Chapter 4

### Algorithm for Finding Maximum Mutual Inductance

This chapter creatively proposes a new optimization algorithm, Maritime Search and Rescue Algorithm (MSRA) - and applies the algorithm, along with Slime Mold Algorithm and Genetic Algorithm, to five well-known optimization test functions (Ackley, Rastrigin, Sphere, Schaffer, and Schwefel). The calculation results are compared and analyzed, leading to the conclusion that MSRA demonstrates excellent performance. Firstly, the convergence speed of MSRA is slightly slower, but it can solve the optimization calculation of most problems with a small total number of iterations, especially for complex functions such as Schwefel and Schaffer. Secondly, the optimization trajectory of MSRA is clear and organized, making it suitable for practical engineering optimization problems such as locating radioactive sources in three-dimensional space. Additionally, the convergence speed, visiting density, and cycle operation times of MSRA can be easily adjusted based on the characteristics and complexity of the calculation object, thereby enhancing calculation accuracy and expanding application scope. Finally, this chapter discusses the application of MSRA to WPT-AAD in this thesis to determine the location of the maximum mutual inductance coefficient.

This chapter is structured as follows. In section 4.1, we provided an overview of existing algorithms and determined that none of them were suitable for the WPT-AAD topic. Therefore, we propose a new algorithm called MSRA. In Section 4.2, we analyzed the principle of MSRA and established its mathematical model. In Section 4.3, Introduction to Optimization Algorithm Test Functions. In section 4.4, we compare the performance of MSRA with two other optimization algorithms. In Section 4.5, we apply MSRA to WPT-AAD in this thesis.

#### 4.1 Algorithm overview

In the analysis of the previous chapter, it was found that when Elderly-EV randomly parks within the parking space markings, the center point of the receiving coil randomly falls within the active range shown in Fig. 3-5-2. By programming the

This material is reserved for educational use only, not allowed for commercial use.

Forbidden to modify the content, and cite the document when use.

control system, after each charging cycle is completed, the transmitting coil returns to the center point within its active range, and this center point is used as the coordinate origin.

Therefore, the task of automatic alignment control is to position the transmitting coil so that the receiving coil falls within a defined interval randomly, aiming to maximize the mutual inductance between the two coils.

Since the motion is relative, for ease of calculation and analysis, it is assumed that the transmitting coil is stationary as the reference for motion, and the center point of the transmitting coil is considered as the coordinate origin. The algorithm's task is to calculate the motion vector of the receiving coil and then control the transmitting coil to move in the opposite direction to achieve the same effect as moving the receiving coil.

Among the actual social production projects, some have a common trait: they not only need to solve the location of the optimal point, but also need to plan the optimal route, make the optimal decision, and so on. Examples of these projects include searching for the location of the maximum magnetic mutual inductance in a three-dimensional magnetic field, searching for the location of radioactive sources in three-dimensional space [34], searching for the location of the leakage of hazardous chemicals and toxic volatile substances [35], sea surface search and rescue [36], etc. The equipment in the optimization project is what is explained here, such as the search and rescue helicopter [36] in the sea search and rescue project and the handle-held detector [34] in searching for the location of radioactive sources. To increase labor productivity, this kind of optimization project needs the right optimization method. Numerous optimization techniques are currently in use, including the SMA [37], the sparrow search algorithm [38], and others.

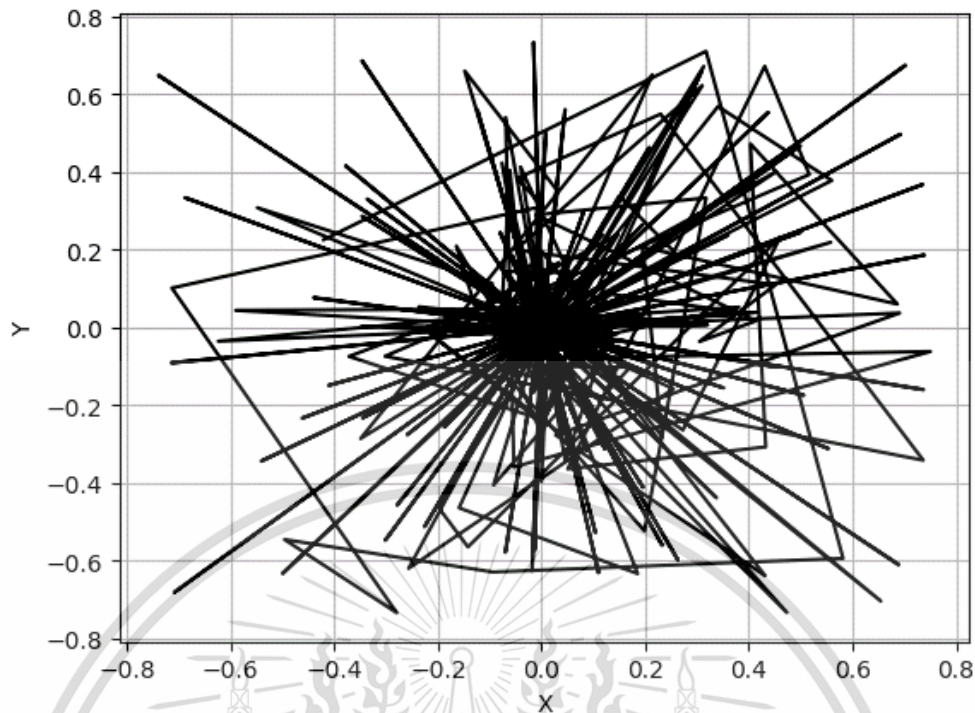


Fig.4-1-1 SMA trajectory route of optimization operation

As seen in Fig.4-1-1, this was a simulation experiment in which we applied the SMA to formula (3-6-2) in order to find the maximum value of  $M$  on a computer. The chaotic curves in the picture are the moving paths taken by the receiving coil. The number of individuals in the population was defined as 20 and the number of cycles as 100. The calculation process created a total of 2020 population members, meaning that there were a total of 2020 iterations. The error value of the computation result was  $8.33 \text{ E}-175$ . The graphic shows that the route design was disorganized. There were a total of 2020 probe position points. Every two adjacent points in time formed a section of the route, and the total route formed many circuitous paths. The majority of intelligent algorithms, like the SMA, are to blame for this. A population made up of dozens of people is defined at the beginning of each algorithm, such as the Mayfly Algorithm [39], the Butterfly Optimization Algorithm [40], the Monarch Butterfly Optimization Algorithm [41], the sparrow search algorithm [38], the Black Widow Optimization Algorithm [42], and so on. Each person in the population represents a random search location point. A batch of the population is created during each iteration. The requirements can be met even though these intelligent algorithms frequently need to define thousands of iterations. The definition of the population



route movement, this thesis proposes a new algorithm: Maritime Search and Rescue Algorithm (MSRA).

## 4.2 Principle of MSRA

The MSRA was inspired by marine search and rescue missions. For example, in the event of a maritime accident, the search rescue organization is given the task, sends search and rescue ships to the designated sea areas [LB, UB], and then, sends shipborne helicopter1, helicopter2, and so forth, to search, as shown in Fig.4-2-1. The algorithm's fundamental idea is then thoroughly explained using the behavior of a single helicopter as an example. As shown in Fig.4-2-2, the search starting point for a single helicopter's search and rescue operations is chosen at random within the delimited area [LB, UB]. The helicopter's arbitrary starting point is indicated by the blue triangle ">" in the illustration. Formula (4-2-1) can be used to describe this behavior:



Fig.4-2-1 Scenario diagram of maritime search rescue [46]

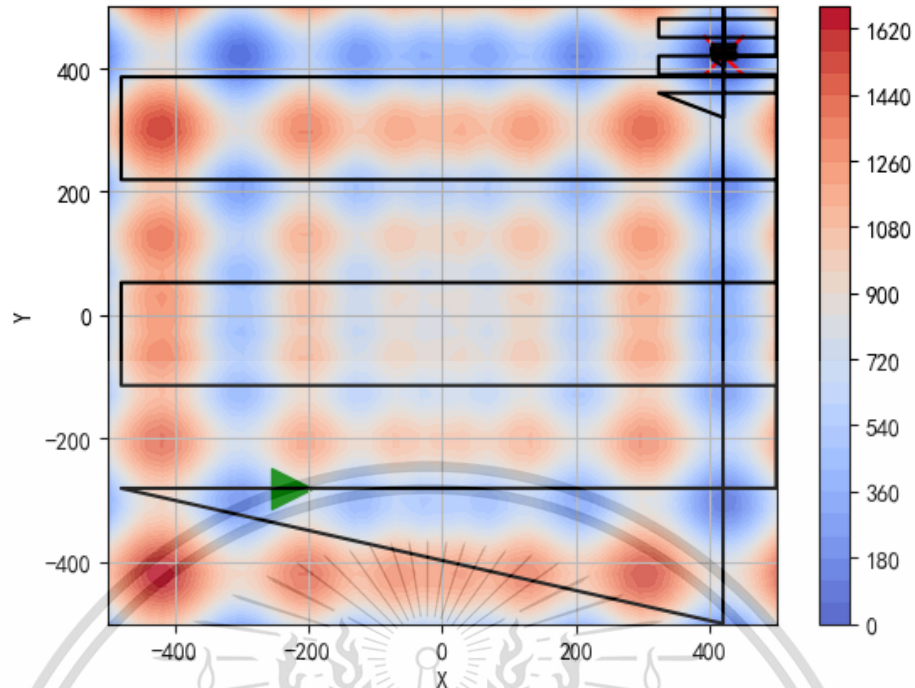


Fig.4-2-2 Schematic diagram of MSRA (The objective function is the Schwefe)

$$\vec{X}_0 = rand * (UB - LB) + LB \quad (4-2-1)$$

where,  $\vec{X}_0$  is the starting position vector,  $UB$  is the upper boundary,  $LB$  is the lower boundary, and "rand" is the random number between (0, 1).  $[LB, UB]$  is the definition area. For this topic in this thesis,  $[UB, LB]$  is the value range of the XYZ coordinates in the magnetic field space to be searched. For the Ackley test function (see Fig.4-3-1), the value range of XY is  $[-5, +5]$ .

Linearly scan the sea surface in the specified X direction (or Y direction) starting from the starting point. The following formula can be used to describe this behavior:

$$\vec{X}_{t+1} = \vec{X}_t + \vec{Y}_{sep} + direction * Xstep \quad (4-2-2)$$

where,  $\vec{X}_t$  is the position of helicopter1 at time "t" from  $\vec{X}_0$ .  $\vec{X}_{t+1}$  is the position update.  $\vec{Y}_{sep}$  is the line spacing between each line of scanning. "direction" is the search direction. " $X_{step}$ " is the search step. These parameters above can be expressed by the following mathematical formula:

$$direction = (-1)^i \quad (4-2-3)$$

This material is reserved for educational use only, not allowed for commercial use.

Forbidden to modify the content, and cite the document when use.

$$Xstep = (UB - LB)/step \quad (4-2-4)$$

$$\vec{Y}_{sep} = (UB - LB)/rows \quad (4-2-5)$$

where, " $i$ " is the scanning order (0, 1, 2, 3 . . . ). It scans in the positive direction at the start of  $i = 0$ . Return to scanning with  $i = 1$  once you have reached the upper boundary. When scanning in the positive direction, " $i$ " is even, and when scanning in the negative direction, it is odd; this cycle is followed. " $step$ " refers to the quantity of visits made while scanning in a positive (or negative) direction and can be interpreted as an integer of the form of 50, 100, 1000, etc. The term " $rows$ " refers to the total number of scanning lines that are anticipated during the entire defined interval and can be represented as an integer such as 5, 6, 7, etc. The distance between planned scanning lines in maritime search and rescue should be as short as possible when encountering complex water conditions and low visibility, which increases the number of scanning lines. The two parameters " $step$ " and " $rows$ " control the sensitivity and error of the MSRA. The sensitivity increases with the value, and this has an impact on the MSRA's computation time as well.

After finishing the x-direction scanning, the aircraft repeatedly scans the suspected area in the y direction. The following formula can be used to describe this behavior.

$$\vec{Y}_{t+1} = \vec{Y}_t + \vec{X}_{bestfitness} + direction * Ystep \quad (4-2-6)$$

where, " $direction$ " and " $Ystep$ " have the same significance as their equivalent counterparts in the x-direction scanning. This is not stated again here.  $\vec{X}_{bestfitness}$  fitness represents the position corresponding to the optimal fitness determined in the previous X-direction scanning. For the minimum problem, the position vector corresponding to the minimum value was obtained. For the maximum problem, the position vector corresponding to the maximum value was discovered.

After completing the previously mentioned all-around rough scanning, the search region was shrunk to concentrate on the ideal suspicious place. With the exception of the smaller search region, the scanning process was the same as the rough scanning method described above. The following mathematical equations can be used to describe this behavior.

$$O_{new} = \vec{Y}_{bestfitness} \quad (4-2-7)$$

$$UB_{new} = O_{new} + \frac{UB-LB}{2 * \max[5, 8 \times (t-2)]} \quad (4-2-8)$$

$$LB_{new} = O_{new} - \frac{UB-LB}{2 * \max(5, 8 \times (t-2))} \quad (4-2-9)$$

where,  $[UB_{new}, LB_{new}]$  is a newly defined narrowing boundary that is allocated to  $[UB, LB]$ , after which the x-direction and y-direction scanning described above is repeated. "t" is the sequence number of this repetition. It is clear from the formula that the convergence speed of the MSRA is governed by  $\max(5, 8 \times t - 1)$  and that this speed has an impact on the calculation inaccuracy of the MSRA. To decrease the convergence speed and increase the calculation accuracy for complicated calculation targets, the convergence parameters can be appropriately changed.

In order to facilitate computer programming, we wrote the pseudo-code of the MSRA.

MSRA pseudo code of the program is as follows.

---

Pseudo-code of the MSRA

---

```

1   Begin.
2   Define the parameters: UB, LB, step, rows, Ysep, Ystep, Mter;
3   Initialize the position of search and rescue aircraft:  $X_0$ ,
4    $X_i (i = 1, 2, \dots, n)$   $X_i (i = 1, 2, \dots, n)$ ;
5   While t in [1, MSRALoop].
6       For i in range (0, step):
7            $\vec{X}_{i+1} = \vec{X}_i + \vec{Y}_{sep} + direction * Xstep$ 
8       End for
9           Calculate the fitness of all  $\vec{X}_i$ 
10          Get the best fitness of  $\vec{X}$ 
11          Assign the Y coordinate corresponding to the best fitness to Yt.
12          For i in range (0, step):
13               $\vec{Y}_{i+1} = \vec{Y}_i + \vec{X}_{bestfitness} + direction * Ystep$ 
14          End for
15          Calculate the fitness of all  $\vec{Y}_i$ 
16          Get the best fitness of  $\vec{Y}$ 

```

---

This material is reserved for educational use only, not allowed for commercial use.

Forbidden to modify the content, and cite the document when use.

---

```

17      Calculate the new UB, LB, and then Update  $UB$ ,  $LB$ 
18       $t=t+1$ 
19      End While
20      Return bestFitness and the corresponding XY coordinates.
      END

```

---

In the pseudo-code of MSRA, line 2 defines several necessary parameters. These parameters were explained in detail in the previous mathematical derivation.

Line 3 writes Formula (4-2-1) as a computer program.

Line 4 sets a loop body. The number of loops is determined by MSRALoop.

Line 5-7 writes Formula (4-2-2) as a computer program.

In line 8-9, the coordinate points scanned in the X direction are substituted into the test function to calculate and take the optimal value. For search the maximum  $M$  in this thesis, this step is to collect the mutual inductance data scanned in the X direction and obtain the optimal value.

In line 10, the Y coordinate corresponding to the best fitness is assigned to  $Y_t$  as the initial value of the Y-direction scan.

Line 11-13 writes Formula (4-2-6) as a computer program.

In line 14-15, the coordinate points scanned in the Y direction are substituted into the test function to calculate and take the optimal value. For Project 1, this step collects the mutual inductance data scanned in the Y direction and obtains the optimal value.

Line 16 writes Formulas (4-2-7) ~ (4-2-9) as a computer program.

In line 17-18, judge whether the loop calculation is completed or not.

In line 19, take the optimal value and the corresponding XY coordinates.

### 4.3 Introduction to optimization algorithm test functions

To verify the effectiveness of the MSRA, this study introduced several promising optimization algorithm test functions. Ackley, Sphere, Schaffer, Schwefe [47], etc., were some of the test functions used for verification. The following is an introduction to the functions.

The Ackley function comes first. Its two-dimensional shape is characterized by an almost flat outer region, as shown in Fig. 4-3-1. The variables' range of limitations is

This material is reserved for educational use only, not allowed for commercial use.

Forbidden to modify the content, and cite the document when use.

[-5, 5]. Many valleys or peaks modulated by cosine waves are superimposed in this nearly flat area, creating an uneven surface and a sizable hole in the center. For optimization algorithms, especially hill-climbing algorithms, this function poses the risk of becoming stuck in one of its numerous local minima. Formula (4-3-1) provides the formulation for this function. [48]

$$f_1(x) = -20 \exp\left(-0.2 \sqrt{\frac{1}{D} \sum_{i=1}^D (x_i^2)}\right) - \exp\left(\frac{1}{D} \sum_{i=1}^D (\cos(2\pi x_i))\right) + 20 + \exp(1) \quad (4-3-1)$$

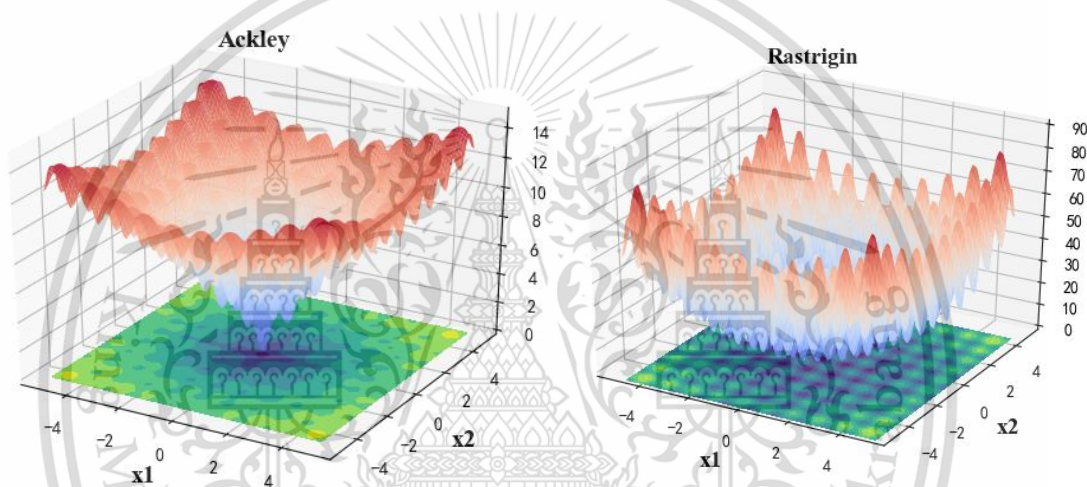


Fig.4-3-1 Ackley function

Fig.4-3-2 Rastrigin function

The second test function is Rastrigin. This function has numerous local minima. It is highly multimodal; the minimum positions are frequently spread out. But the global minimum is 0, located in the middle. The two-dimensional variable value range of this function is [-5, 5], and its graph and formula are as follows.

$$f_2(x) = 10D + \sum_{i=1}^D (x_i^2 - 10 \cos(2\pi x_i)) \quad (4-3-2) [48]$$

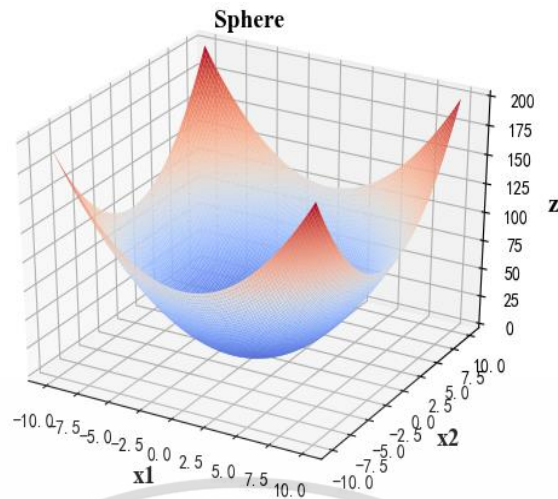


Fig.4-3-3 Sphere function

The third function is the Sphere function. The Sphere function is a unimodal function used for minimization, primarily for verifying algorithms. The two-dimensional variable value range of this function is  $[-10, 10]$ . Its global minimum value is 0, located at  $(0,0)$ . The image is shown below, and its formulation is as follows.

$$f_3(x) = \sum_{i=1}^n x_i^2 \quad (4-3-3) [48]$$

The Schwefe function has many local small peaks and valleys, and the image of its two-dimensional variable resembles a vast series of rolling mountains. The two-dimensional variable value range of this function is  $[-500, 500]$ . The global minimum value of the function is approximately  $2.5455132458773733E-05$ , occurring at  $(420.9687468, 420.96874586)$ . The global maximum value is around  $1675.9315745448675$ , found at  $(-420.96874707, -420.96874634)$ . The function's formulation and graph are presented below.

$$f_4(x) = 418.9829d - \sum_{i=1}^d x_i \sin(\sqrt{|x_i|}) \quad (4-3-4) [48]$$

The Schaffer function is often used to test the performance of optimization algorithms. The function exhibits strong fluctuations and numerous extreme points. The global maximum value is 1, located at  $(0,0)$ , and there are local extreme values surrounded by infinite circles at the periphery of the global optimum. The two-dimensional variable value range of this function is  $[-7.5, 7.5]$ , and its graph is shown

below. The function is formulated as follows.

$$f_5(x) = 0.5 - \frac{\left[ \sin\left(\sqrt{x_1^2 + x_2^2}\right) \right]^2 - 0.5}{\left[ 1 + 0.001 \times (x_1^2 + x_2^2) \right]^2} \quad (4-3-5) [48]$$

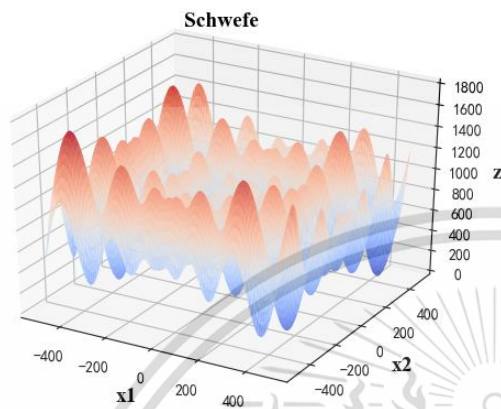


Fig.4-3-4 Schwefel function

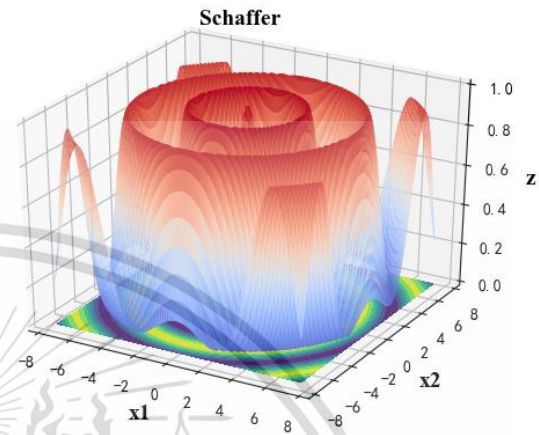


Fig.4-3-5 Schaffer function

In addition, there are numerous optimization algorithm test functions, such as the Griewank function [49], the Rastrigin function, the Levy function, the Langermann function, and others, that are commonly used for testing optimization algorithms [50]. Due to space constraints, detailed descriptions of these functions and datasets were not provided here.

#### 4.4 Performance comparison between MSRA and other two algorithms

To verify the effectiveness of the MSRA, this study introduced several promising optimization algorithm test functions above and compared the test results with the classical Genetic Algorithm (GA) [51] and the SMA.

In the 1970s, the GA was first advocated by John Holland in the United States of America [52]. The algorithm was created and put forth in accordance with the natural rules of evolution that apply to creatures. It is a computer simulation of the biological evolution process that replicates the genetic and natural selection mechanisms described in Darwin's theory of biological evolution [53]. This technique mimics the natural evolution process in order to find the best answer. The method changes the process of problemsolving into one that is analogous to the crossing and mutation of chromosomes and genes in biological evolution through mathematics and

This material is reserved for educational use only, not allowed for commercial use.

Forbidden to modify the content, and cite the document when use.

computer simulation [52]. When compared to other traditional optimization techniques, it typically produces better optimization outcomes more quickly when handling complex combinatorial optimization issues. The GA has been made extensive use of in combinatorial optimization, machine learning, signal processing, adaptive control, and artificial life [54].

The SMA was proposed by Li et al. in 2020 [37]. It was inspired by the diffusion and foraging behavior of slime molds. The SMA mainly simulates the behavior and morphological changes of slime molds during the foraging process without modeling the complete life cycle. The weight index was used to simulate the three correlations between the morphological changes of the myxomycete venous duct and the contraction mode. The algorithm is a meta-heuristic algorithm, which has the characteristics of fast convergence and strong optimization ability.

To unify the assumptions, the number of iterations was defined as one operation by substituting independent variables into the objective function each time, which was counted as one iteration.

The following describes the performance comparison analysis of the MSRA, SMA, and GA applied to the four aforementioned test functions.

Three optimization algorithms are applied to the aforementioned five test functions, with a maximum of 5000 iterations set. As mentioned above, the term "number of iterations" refers to counting each operation of substituting the independent variable representing the position into the test function as one iteration. The four functions Ackley, Rastrigin, Sphere, and Schwefel utilize all three optimization algorithms to calculate the minimum value. In the case of the Schaffer function, the three optimization algorithms calculate the maximum value. By conducting these operations, the iterative curve depicted in Fig. 4-4-1~Fig. 4-4-5, and the error value of the calculation result is shown in table 4-4-1.

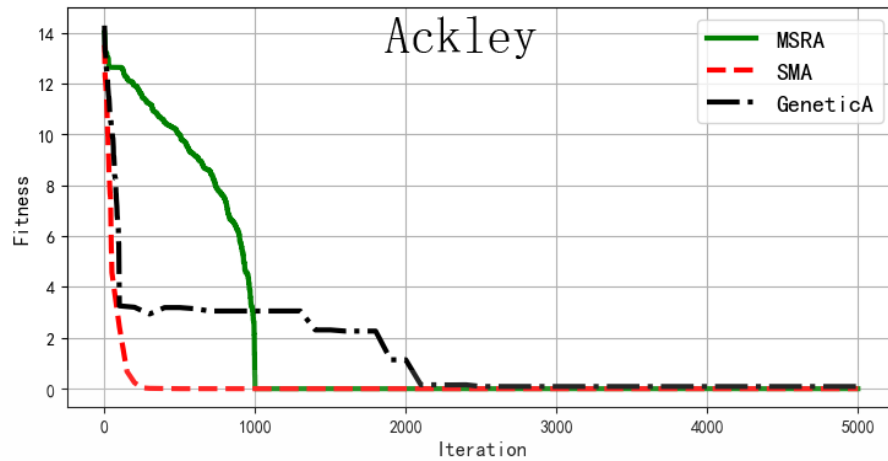


Fig.4-4-1 Algorithm iteration curve (Ackley function)

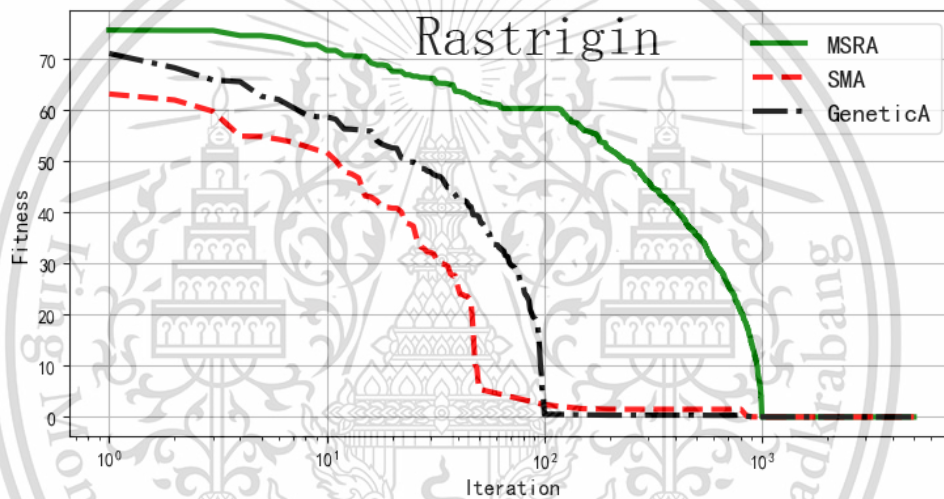


Fig.4-4-2 Algorithm iteration curve (Rastrigin function)

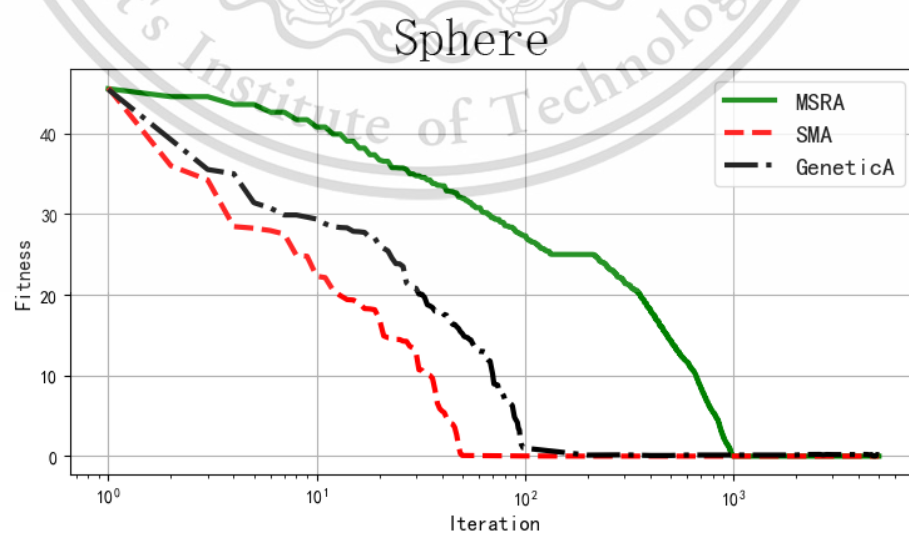


Fig.4-4-3 Algorithm iteration curve (Sphere function)

This material is reserved for educational use only, not allowed for commercial use.

Forbidden to modify the content, and cite the document when use.

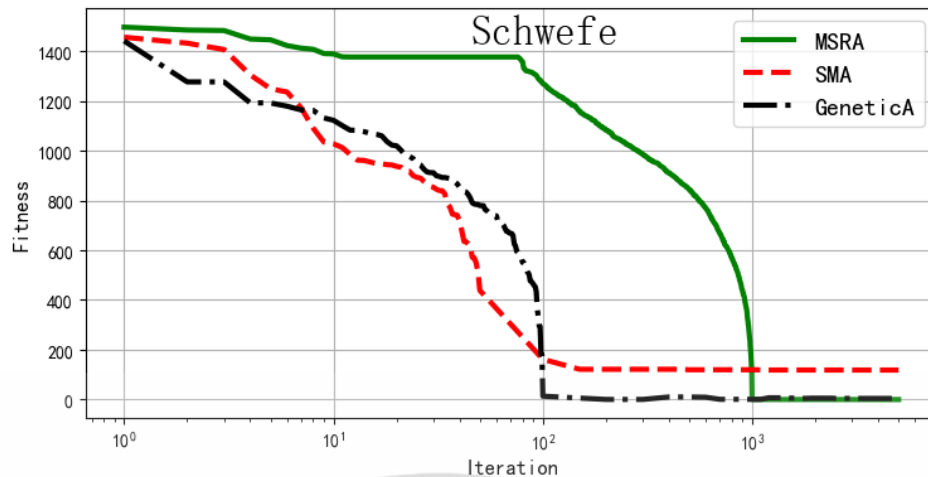


Fig.4-4-4 Algorithm iteration curve (Schwefe function)

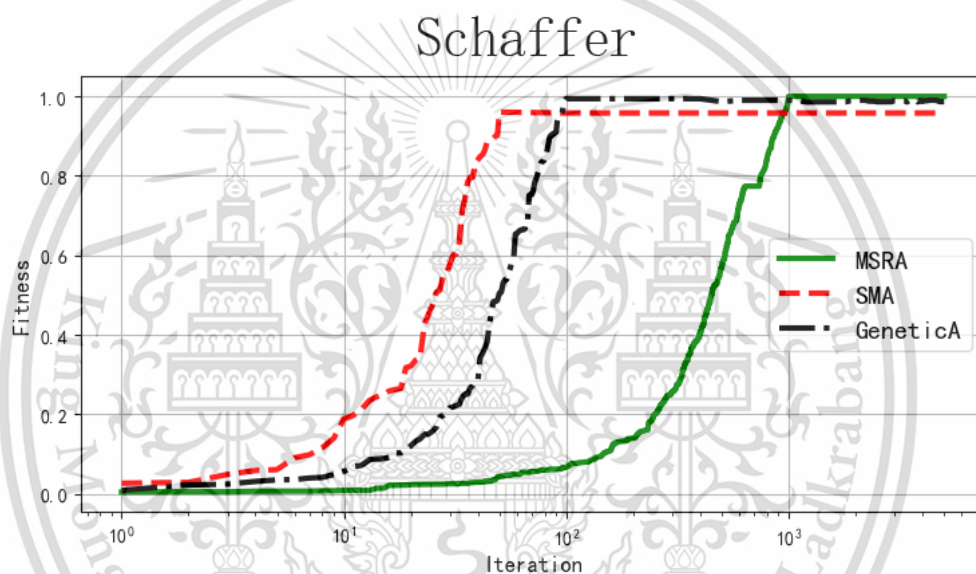


Fig.4-4-5 Algorithm iteration curve (Schaffer function)

By analyzing the iterative curve and error table, it is found that the convergence speed of SMA is the fastest, followed by GeneticA, and finally MSRA. For the three test functions of Ackley, Rastrigin, and Sphere, the three algorithms demonstrate excellent optimization performance. Among them, SMA has the smallest error value and the highest accuracy, followed by MSRA. However, the error value of MSRA also reaches the level of  $10^{-15}$ , making it suitable for most applications. On the other hand, GeneticA has the largest error value, reaching the level of  $10^{-2}$ , which may not meet the requirements of most applications. For the relatively complex Schaffer and Schwefe test functions, MSRA still demonstrates excellent optimization performance, while SMA and GeneticA perform much worse. It is estimated that these two algorithms reach local extremum in complex test functions.

This material is reserved for educational use only, not allowed for commercial use.

Forbidden to modify the content, and cite the document when use.

**Table4-4-1 5000 iterations error analysis table (5 functions)**

Test function	Ackley	Rastrigin	Sphere	Schaffer	Schwefe
iteration	5000	5000	5000	5000	5000
MSRA Error	3.55e-15	1.53e-15	2.59e-31	6.49e-15	2.55e-05
SMA Error	2.31e-86	7.55e-73	2.39e-176	4.19e-2	118.438
GeneticA Error	8.71 e-2	3.51 e-4	1.45 e-1	1.34	4.343

In the classical GeneticA, the natural selection process employs the roulette method, where individuals with high fitness have a greater chance of being selected to pass on their genes and phenotypes, while those with low fitness are more likely to be eliminated. However, due to the randomness of the roulette method, individuals with optimal fitness may also be eliminated, leading to variations in results obtained by the classical genetic algorithm across multiple runs, which may only approximate the optimal solution. Therefore, when GeneticA is applied to a simple function such as Sphere, the results of each operation vary greatly, and the error value is also large, which is a limitation of the classical genetic algorithm.

Adjust the number of iterations for the three algorithms to 20,000 times. The adjustment method is MSRA. For functions with many local extremum, increase the number of scanning lines and visitation density, and appropriately reduce the number of cyclic operations. For functions similar to a sphere or cone, reduce the number of scanning lines and increase the visitation density and cyclic operations accordingly. For SMA and GeneticA, in functions with many local extremums, increase the number of populations and appropriately reduce the number of cyclic operations. For functions such as spheres or cones, the number of iterations can be reduced, while the number of cyclic operations can be appropriately increased. After setting the iteration times for the three algorithms, they are also applied to the aforementioned five test functions. The operation results are shown in Table 4-4-2.

**Table4-4-2 20000 iterations error analysis table (5 functions)**

Test function	Ackley	Rastrigin	Sphere	Schaffer	Schwefe
iteration	20000	20000	20000	20000	20000

MSRA Error	3.553e-15	0	4.4036e-30	0	3.3164e-05
SMA Error	0	0	0	0.00972588	4.1154e-05
GeneticA Error	0.0630238	0.08175796	-0.0342940295	0.00971834	0.28997843

For the data in the table, the error value of 0 only indicates the calculation results under the default accuracy conditions of the running software python.

By analyzing the table data, it can be seen that for functions similar to spherical, conical, or disk terrain, such as Ackley, Rastrigin, and Sphere, when the number of iterations is limited to 20,000, the performance of SMA is slightly better than MSRA, while GeneticA performs the worst. For mountain-shaped functions like Schaffer and Schwefe functions, MSRA demonstrates the best performance, SMA estimation gets trapped in local extreme points, and GeneticA shows the worst performance.

By comparing and analyzing the data in Table 4-4-1 and Table 4-4-2, it is evident that, irrespective of the number of iterations, the performance of the GeneticA was the poorest among the three algorithms. For functions with a simple shape, when the number of iterations was 5000, the performance of the SMA was obviously better than the MSRA. However, when the number of iterations was increased to 20,000, the performance of the SMA and MSRA became very similar. For functions with complex shapes, regardless of the number of iterations, the performance of the MSRA was significantly better than the SMA.

The following focuses on the performance of MSRA and SMA algorithms in complex test functions.

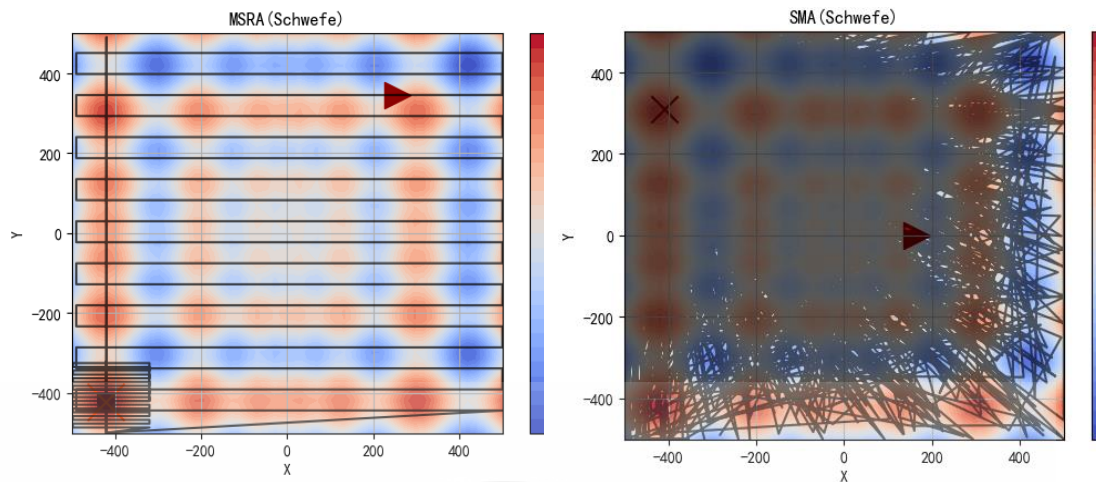


Fig.4-4-6 MSRA and SMA Search track (Schwefe function)

In order to visualize the performance of MSRA and SMA algorithms when applied to complex test functions like Schwefe from the perspective of a search and rescue aircraft, the starting point ">" of the search and rescue operation and the optimal fitness position point "X" are computer-programmed. These points are then marked on the contour map of the test function, as illustrated in Fig. 4-4-6. Subsequently, these points are connected with line segments based on the search order to depict the flight route of the search and rescue aircraft. Similarly, the search position points, search starting points, and optimal fitness positions during SMA operation are marked on the contour map of the test function. These points are also connected with line segments according to the search order. In the case of MSRA, the contour map of the test function can be interpreted as the search and rescue sea surface of the specified area. In search and rescue operations, the highest or lowest point in an area is the target point. In the context of Spatial Movement Automaton (SMA), the contour map of the test function can be likened to the foraging area of a specified region, with the highest or lowest point representing the location with the most abundant food resources. For the Schwefe function, in order to clearly identify the location of food abundance, the iteration times of generation optimization trajectory cannot be set too large. The MSRA and SMA algorithms set the iteration times to  $1 \times 10^4$  to perform all operations to obtain the maximum value. Each algorithm is run three times, and the optimal position and error value are calculated, as shown in Table 4-4-3. Figure 4-4-6 above displays the optimization trajectory diagram of one of the two algorithms.

Table4-4-3 Error and optimization target point location (Schwefe function)

Running sequence	1th		2th		3th	
Iteration	10000		10000		10000	
	Error	Location	Error	Location	Error	Location
MSRA	3.64e-12	(-420.96875, -420.96875)	5.06e-08	(-420.9692, -420.9692)	9.4e-08	(-420.9680277, -420.9692)
SMA	368.0	(-453.7, 500)	392.6	(-432.5, -241.1)	137.7	(-409.3, 306.9)

By analyzing the table data, it can be seen that MSRA can calculate the optimal position accurately each time, with very small error values. On the other hand, the optimal location points obtained by each SMA operation vary significantly and tend to fall into local extreme points randomly.

By analyzing the trajectory diagram, it can be seen that the trajectory of MSRA is clear and orderly, which is suitable for engineering projects requiring actual mobile optimization equipment, such as sea search and rescue, searching for the position of maximum magnetic induction intensity in three-dimensional magnetic field space, and locating electromagnetic wave emission sources in three-dimensional space. On the other hand, the trajectory of SMA is chaotic and exhibits significant overlap. It is not suitable for engineering projects that require actual mobile optimization equipment. It is only suitable for optimizing the objective function on a computer.

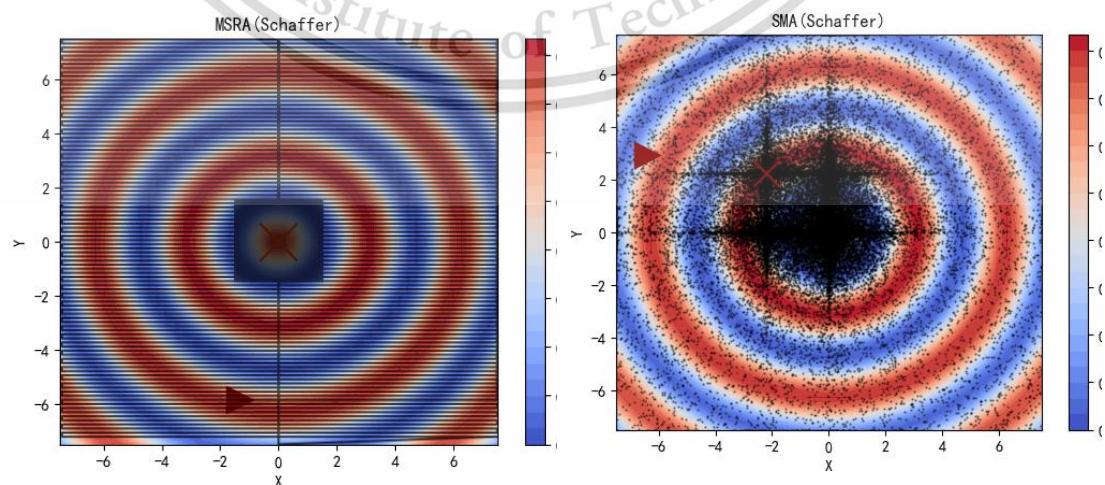


Fig.4-4-7 MSRA and SMA Search track (Schaffer function)

This material is reserved for educational use only, not allowed for commercial use.

Forbidden to modify the content, and cite the document when use.

For the Schaffer function, its maximum value lies on a small cusp. MSRA and SMA both set the number of iterations to 10000 and then operated 10 times, respectively. The two algorithms inevitably fall into local extreme points at random. To address this issue, consider increasing the scanning line density and visiting point density of MSRA, as well as boosting the population number and cycle operation times of SMA. Additionally, set the iteration times of both algorithms to  $1 \times 10^5$  and then operated 10 times, respectively. The trajectory diagram of an optimization operation is depicted in Figure 4-3-12. Since the trajectory diagram of the SMA is a chaotic line segment and lacks meaning, only the iterative position points are depicted on the diagram. The two algorithms are applied to the Schaffer function. The error value and optimization target point location of the operation result are shown in Table 4-3-4. The data in the table is only selected three times.

**Table4-4-4 Error and optimization target point location (Schaffer function)**

Running sequence	1th		2th		3th	
Iteration	100000		100000		100000	
	Error	Location	Error	Location	Error	Location
MSRA	0	(-1.212E-14, 1.212E-14)	0	(-1.212E-14, 1.212E-14)	0	(-1.185E-14, 1.213E-14)
SMA	9.717E-3	(3.13559095, 0.11067923)	9.716E-3	(2.31053, -2.12505)	9.721 E-3	(-2.204, 2.238)

By analyzing the values in the table, it can be seen that under the default calculation accuracy of Python software, the MSRA method is applied to the Schaffer function to determine the maximum value, resulting in an error value of 0. Such excellent results can be obtained after multiple operations. Under the condition that the number of scanning rows is 99 and the number of scanning columns is 1, with 200 visits per row or column, the number of cycles is reduced from 6 to 2, resulting in a total of 20,000 iterations. After running MSRA more than 10 times, none of the runs reached a local extreme point, and the error value of the results was 0. This demonstrates the excellent performance of MSRA on complex test functions. In

This material is reserved for educational use only, not allowed for commercial use.

Forbidden to modify the content, and cite the document when use.

contrast, SMA still occasionally gets stuck in local extreme points, as evidenced by its iterative trajectory and relatively large calculation errors. To address this, the number of myxomycetes was increased from 1000 to 5000, and the number of iterations from 100 to 1000, resulting in a total of 5 million iterations. After more than 10 operations, the SMA is analyzed based on its output iterative trajectory and the error value of calculation results. It still randomly converges to the local optimum value.

For the complex function optimization problem, the SMA will arbitrarily land in the local extreme values. Investigating the cause is essential. According to the SMA principle, the slime mold population is initially globally distributed at random at the beginning of the first cycle. At this point, it is inevitable that some areas would have a significant amount of slime mold, while other areas would be empty. The portrayal of its repetitive journey lends credence to this. Beginning with the second series of procedures, the search region is swiftly constrained around the best point identified during the previous search. Reaching local extreme points for functions as complex as the Schwefe and Schaffer functions is simplified by this algorithmic concept. Likewise, any algorithm that relies on a random population distribution, such as the sparrow search algorithm [27], inherently possesses these shortcomings.

The MSRA principle states that exploration points are uniformly distributed globally during the first cycle of operation. Subsequently, starting from the second cycle of operation, the search range is gradually reduced at a certain convergence speed to enhance output accuracy. In problem optimization calculations, unlike swarm intelligence optimization algorithms such as the SMA, which rely on a randomly distributed population principle, the MSRA does not have this limitation. According to this principle, the MSRA can be used to solve the majority of optimization calculation issues.

Another notable benefit of the MSRA is its ability to utilize a direct search route trajectory to locate the optimal position point for functions such as the Sphere function. These functions are akin to spherical or conical surfaces but do not have local extrema. According to Figure 4-4-7, which uses the Sphere function as an example, ">" represents the search's randomly chosen starting point; the black line denotes the search route's trajectory, and "X" denotes the best fitness position that was sought. Three scanning lines, one column, one thousand visits per line, five cyclic operations, and twenty thousand iterations make up the MSRA's parameter settings. The margin of

This material is reserved for educational use only, not allowed for commercial use.

Forbidden to modify the content, and cite the document when use.

error for the calculated result was  $2.87 \times 10^{-26}$ . The figure illustrates how the MSRA can achieve such accuracy with a simple and clear track route.

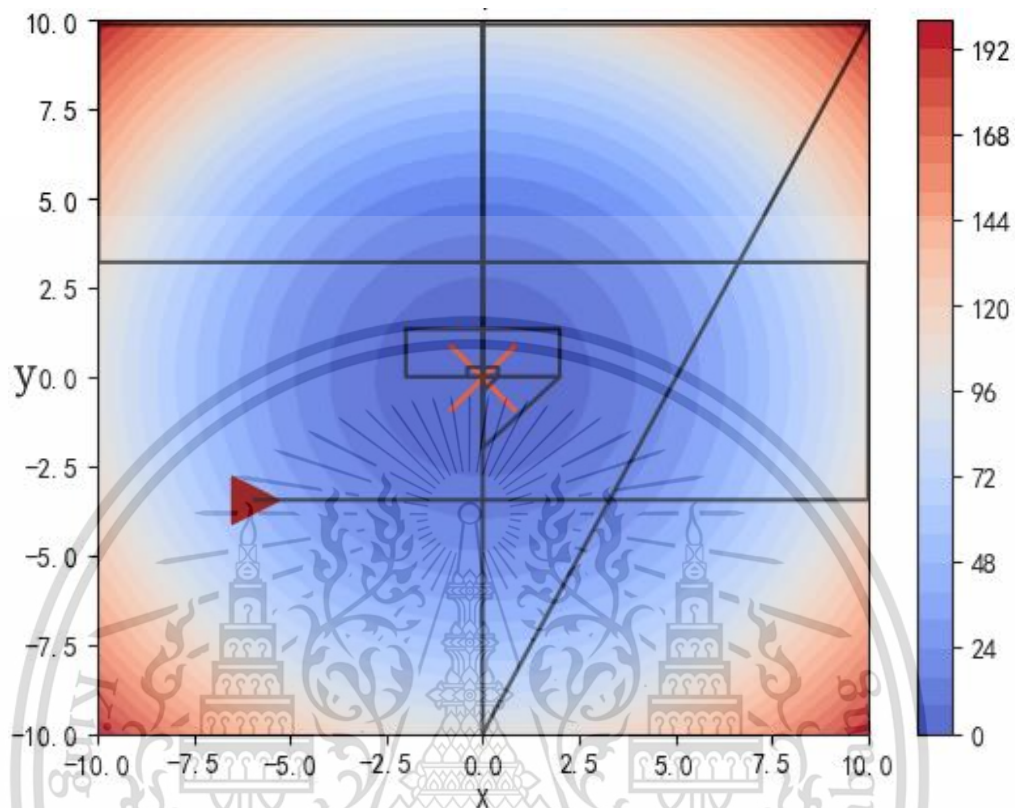


Fig.4-4-8. MSRA trajectory to find the optimal value (Sphere function).

In addition, we also tested and compared all the other test functions mentioned in Reference [50], totaling 47. We arrived at the same conclusion as above, but due to space constraints, we will not describe them in detail here.

The research mentioned above makes it clear that the MSRA performs optimization operations effectively, and its optimization process is straightforward and well-structured. It is expected that the MSRA will have a promising future in terms of applications.

Several problems remain unresolved. Firstly, for the social production projects mentioned in the previous section of the thesis, we utilized the MSRA for WPT-AAD and conducted experiments to validate it. For the other three projects (searching for the location of the leakage of hazardous chemicals and toxic volatile substances, sea surface search and rescue), we did not have the conditions for experimental verification. Secondly, it is necessary to optimize the MSRA's mathematical model and

study the mathematical models and test analyses that the MSRA applies to higher-dimensional optimization problems. Third, when planning the route, the MSRA does not include obstacle avoidance functionality. This function needs further development.

#### 4.5 MSRA is applied to find the maximum mutual inductance

Primary research focuses on a wireless power transfer automatic alignment device, abbreviated as WPT-AAD.

In this thesis, the control of WPT-AAD involves optimizing the objective function defined by formulas (5-4-1) and (5-5-1). In the theoretical analysis of the algorithm, since the actual input and output power of the WPT system are not measured, the objective function of the algorithm uses formula (3-6-2). Through the analysis of the experimental data in the third chapter, we can observe that in the WPT system, the distribution of the magnetic field, the coefficient of mutual inductance, and the positional relationship between the two coils are in line with practical applications. Therefore, the theoretical analysis of the algorithm using formula (3-6-2) does not affect the applicability of the algorithm itself.

In this thesis, the calculation process of the mutual inductance coefficient involves two cumulative calculations and one integral calculation. The calculation formula is very long, resulting in a complex calculation process and extended calculation time. MSRA requires a significant amount of time for each iteration of the mutual inductance coefficient formula. Therefore, the MSRA parameters were adjusted to a smaller value of 2500. After 10 iterations, the same results were achieved. As shown in Fig. 4-5-1, several broken line segments represent the search route. The ">" symbol indicates the random search starting point, while "X" represents the optimal fitness position searched, which is the position point with the maximum mutual inductance coefficient to be searched in this thesis. The depth of the cold and warm colors in the figure represents the magnitude of the mutual inductance coefficient. "Obviously, this is consistent with the theoretical analysis and estimation in Chapter 4 of this thesis." The position of the maximum mutual inductance coefficient should be at the center of the transmitting coil. Moreover, the maximum mutual inductance coefficient calculated based on the positive central coordinate is  $7.8702842E-06$  with deviation. The optimal position point identified by MSRA is  $(8.0885E-02, 0)$  or  $(-8.0885E-$

This material is reserved for educational use only, not allowed for commercial use.

Forbidden to modify the content, and cite the document when use.

02, 0), with an optimal value of  $7.8741988776E-06$ . It is evident that the optimal value found by MSRA is superior, and the optimal position point is slightly offset to the left or right of the central point. Analyze the impact of the transmitting coil's structure.

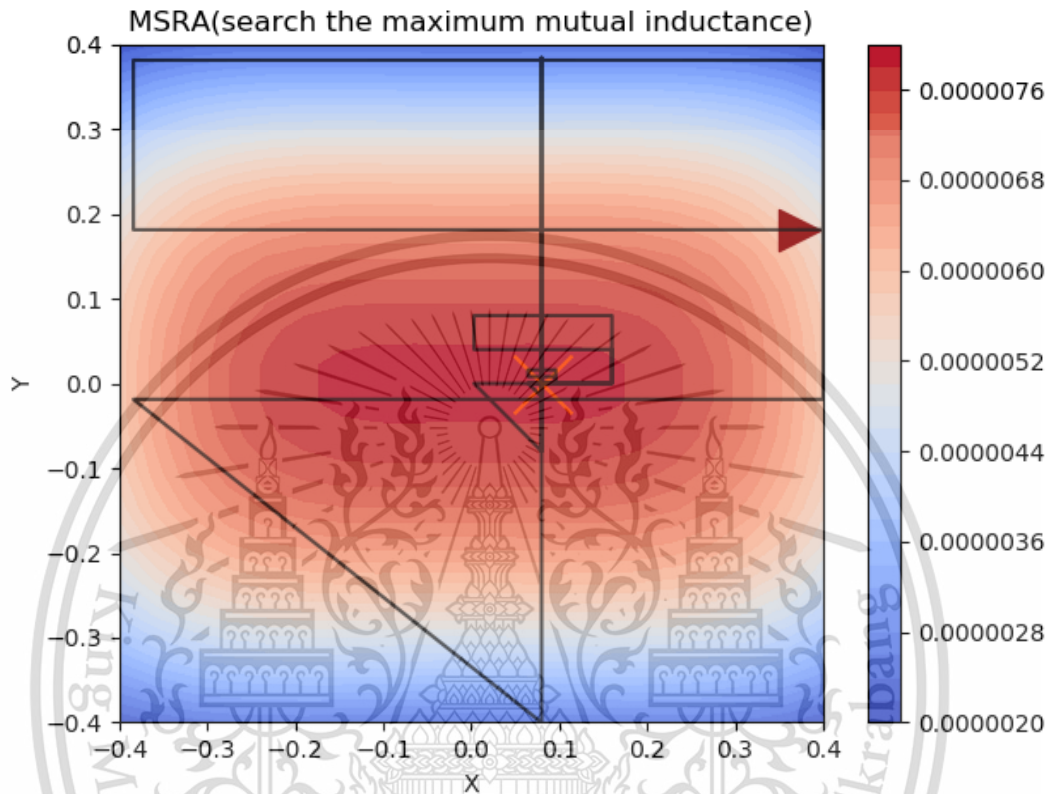


Fig.4-5-1 Trajectory diagram of MSRA search the maximum mutual inductance

This chapter analyzes and discusses a new optimization algorithm, MSRA, and applies it to the topic of WPT-AAD, providing a theoretical basis for the subsequent research. It can be predicted that MSRA has good universal applicability, and its application prospects are very broad.

## Chapter 5

### WPT-AAD of Design and Experiment

According to the theoretical analysis and control requirements discussed in the previous chapter regarding the application of the Maritime Search and Rescue Algorithm (MSRA) to WPT-AAD (Wireless Power Transmission Automatic Alignment Device), this chapter focuses on designing the hardware system of WPT-AAD and writing the control program for MSRA applied to WPT-AAD. Then, the WPT-AAD experimental bench is designed, and five experiments with different parameters of MCR-WPT are conducted on this bench. Subsequently, the WPT-AAD experiment is performed using appropriate parameters of MCR-WPT. In these six experiments, detailed experimental data were recorded and analyzed. As a result, it was concluded that the experimental data essentially aligned with the previous theoretical analysis.

This chapter is structured as follows. In Section 5.1, we designed the hardware of WPT-AAD. In Section 5.2, we designed the MCU (Microcontroller) control program for WPT-AAD. In Section 5.3, we set up the experimental bench for WPT-AAD. In sections 5.4, 5.5, and 5.6, we conducted six experiments and analyzed the experimental data.

#### 5.1 Structural design for WPT-AAD

From the above analysis, the WPT-AAD can utilize MSRA to determine the location of the maximum mutual inductance and plan the search route.

Next, it analyzes how to use MSRA for WPT-AAD control and hardware design.

According to the above analysis, the control of WPT-AAD can be achieved through an automatic control system consisting of a stepper motor, screw slide, and a single-chip microcomputer. As shown in Figure 5-1-1, the transmitting coil is fixed on the x-axis slide, and the entire set of x-axis screw slides is fixed on two synchronously moving Y-axis slides. In this way, an "H"-type XY two-axis motion unit is constructed, composed of three sets of screw slides. The motion control is mainly achieved by the MCU through the stepper motor driver to control the stepper motors in two directions, enabling the motion control of the transmitting coil in the XY directions. The overall installation layout of the WPT-AAD system is illustrated in Figure 5-1-2.

This material is reserved for educational use only, not allowed for commercial use.

Forbidden to modify the content, and cite the document when use.

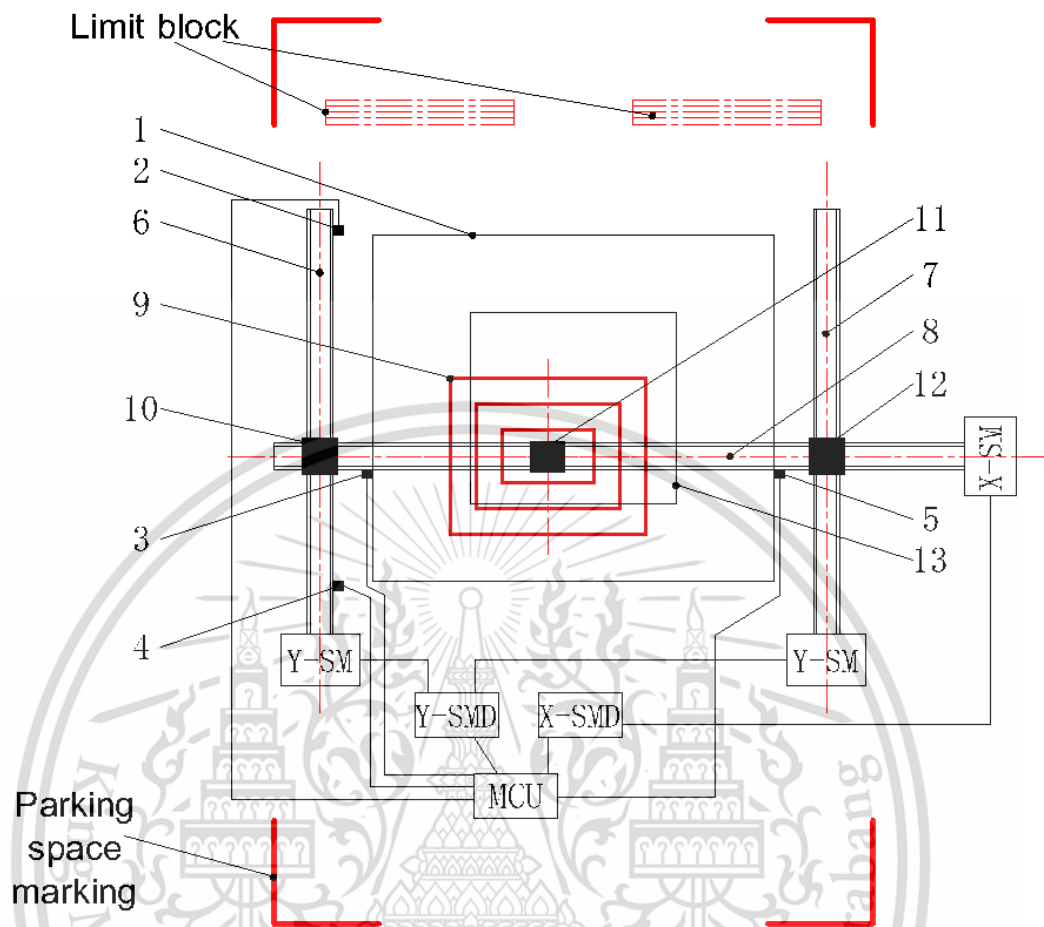


Fig.5-1-1 Diagram of the WPT-AAD

1. Active range for Transmite coi.
- 2.Y-axis positive direction limit position sensor.
3. X-axis negative direction limit position sensor.
4. Y-axis negative direction limit position sensor
5. X-axis positive direction limit position sensor
6. Y-axis screw rod one;
7. Y-axis screw rod two;
8. X-axis screw rod;
9. Transmitting-coil;
10. Y-axis sliding-table-one;
11. X-axis sliding table;
12. Y-axis sliding-table-two;
13. Active range for center point of receiving-coil;
14. receiving-coil;

This material is reserved for educational use only, not allowed for commercial use.

Forbidden to modify the content, and cite the document when use.

15. Glass cover;

16. Parking space ground;

MCU. Microcontroller Unit.

Y-SM. Stepper motor in Y-axis;

VC-SM. Voltage and current sampling module;

X-SM. Stepper motor in X-axis;

Y-SMD. Stepper motor driver in Y-axis;

X-SMD. Stepper motor driver in X-axis;



This material is reserved for educational use only, not allowed for commercial use.

Forbidden to modify the content, and cite the document when use.

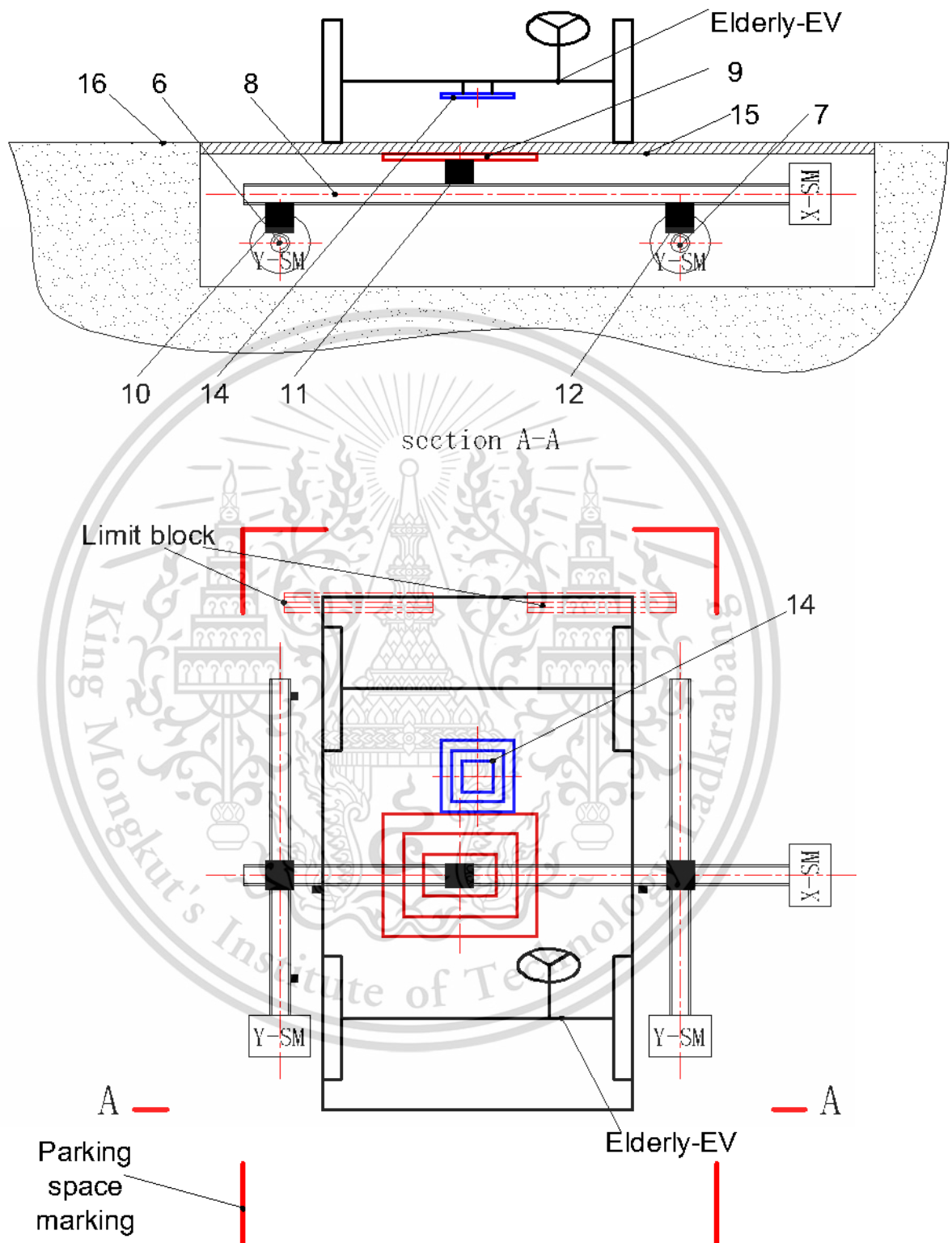


Fig.5-1-2 Overall installation layout of the WPT-AAD

This material is reserved for educational use only, not allowed for commercial use.

Forbidden to modify the content, and cite the document when use.

## 5.2 Design of MCU control program

The Microcontroller Unit flow chart of the control procedure is as follows

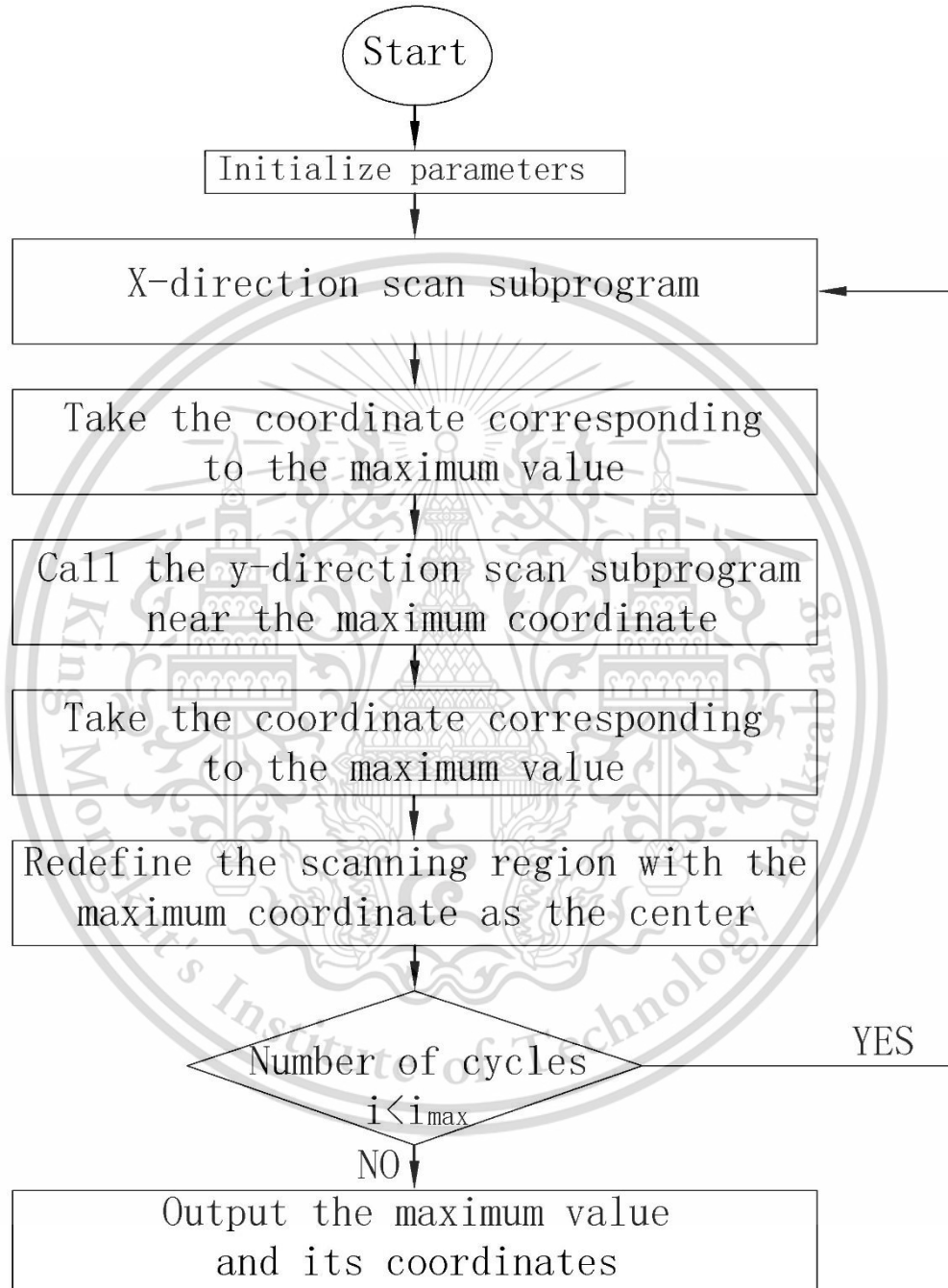


Fig.5-2-1 Main program flow chart of MCU

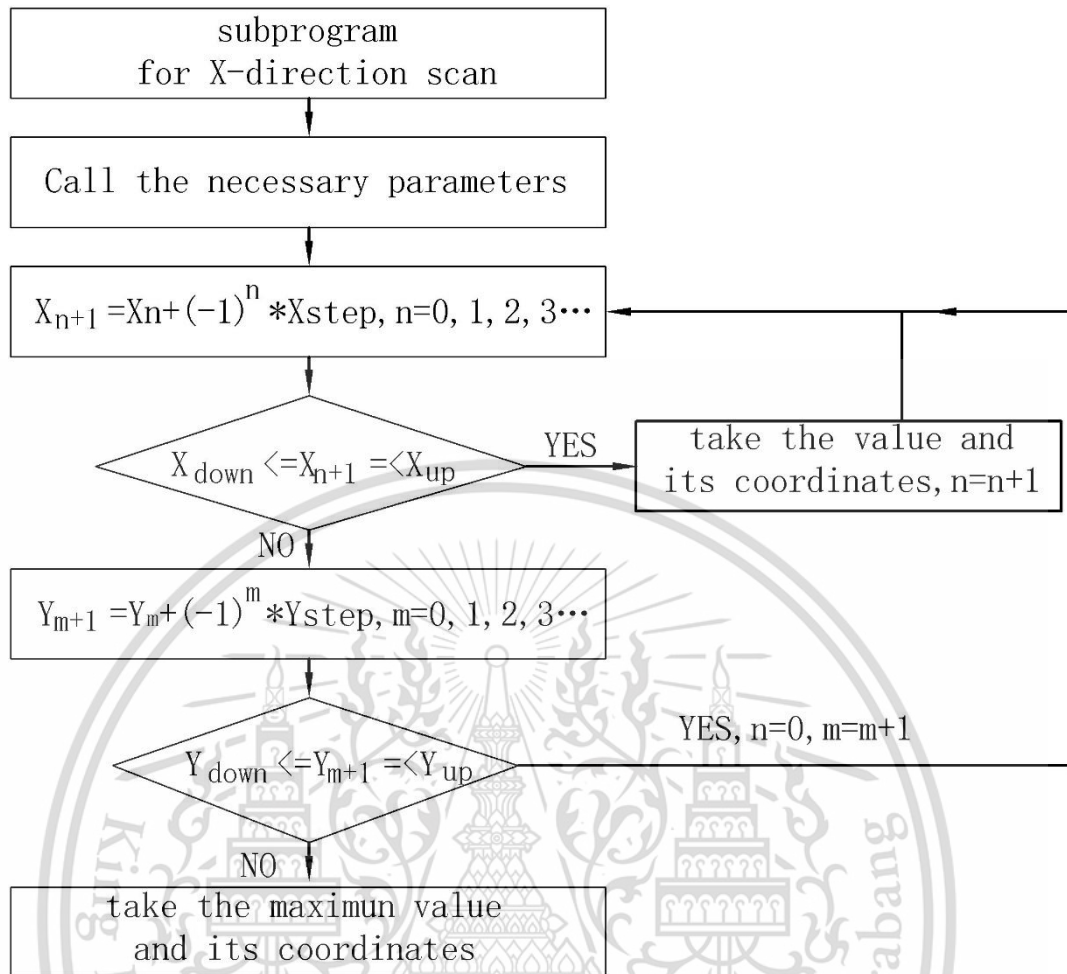


Fig.5-2-2 X-direction subprogram flow chart of MCU

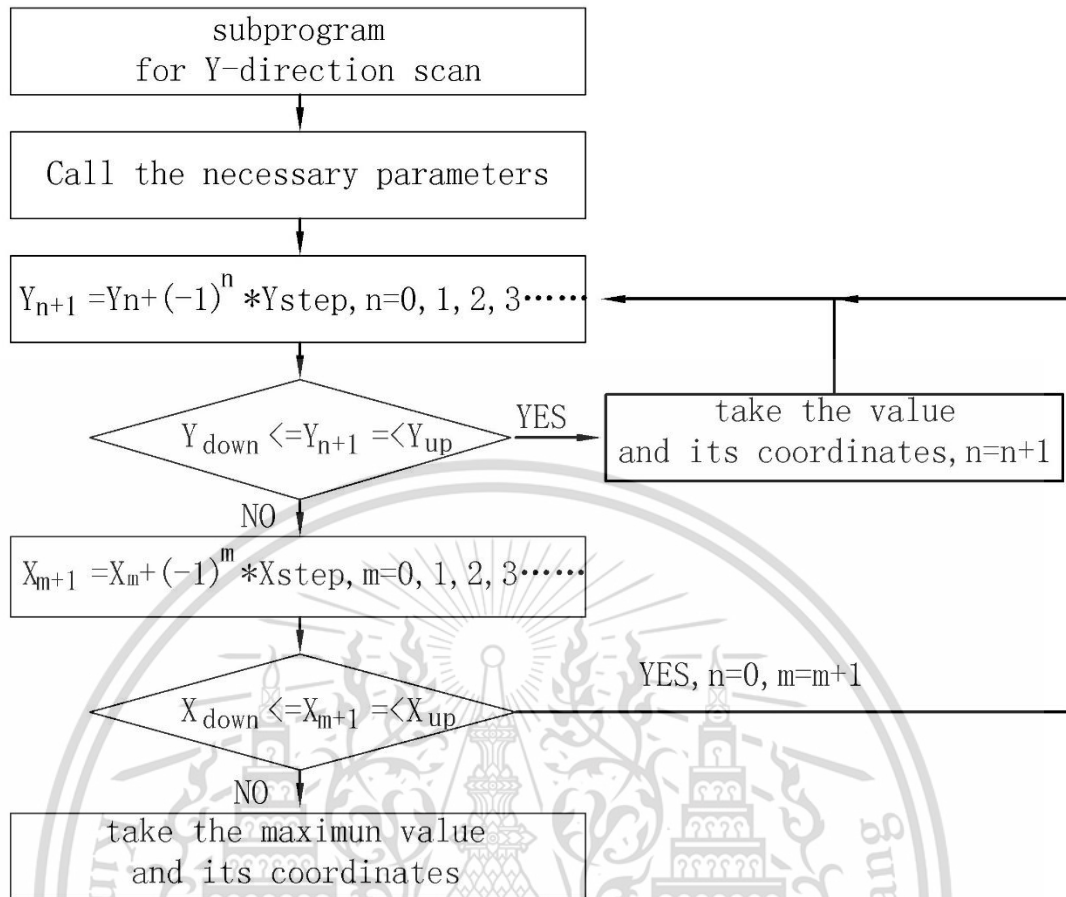


Fig.5-2-3 Y-direction subprogram flow chart of MCU

The MCU program based on the C language is shown in Attachment 1, Table 5-2-1. This program can be compiled directly, burned into the MCU, and then executed.

### 5.3 Setup of WPT-AAD experimen bench

Through the calculations and analysis in Chapter 2, it can be seen that the total power storage capacity of the power battery of the elderly EV designed in this thesis is 38 kWh. According to the requirement of completing 90% of the charging capacity in 8 hours, a wireless charging system with a charging power of 4.75 kW needs to be designed to meet this criterion.

The overall design of MCR-WPT consists of the main circuit module ② and two driving circuit modules ① and ③, as shown in Fig. 5-3-1. The main circuit module ② comprises the rectifier filter circuit, high-frequency inverter circuit, resonant unit, high-frequency rectifier, and load. The resonant unit is divided into the

transmitter resonant unit and the receiver resonant unit. The transmitter resonant unit consists of the transmitter coil L1 and the resonant capacitor C22. The receiver resonant unit is composed of the receiver coil L2 and the resonant capacitor capacitor C23. The resonant capacitors are connected in series with the coil.

The transmitter of the system converts the DC output from the DC power supply ④ into a high-frequency square wave AC through the high-frequency inverter to drive the transmitter resonant unit. The L1 and C22 in the system exhibit high-frequency resonance. When the driving frequency of the high-frequency inverter matches the resonant frequency, the impedance of the transmitter is in a purely resistive state. The transmitting coil is excited by the output current of the inverter and generates a magnetic field around it. The receiving end resonant circuit, composed of the receiving coil L2 and the resonant capacitor C23, is positioned in the magnetic field. It generates induced electromotive force, facilitating the wireless transmission of electric energy from the transmitting end to the receiving end. The induced AC voltage is rectified into DC through the rectifier. Subsequently, the switch ripple is filtered out by the output filter capacitor to provide stable DC power for the load. The resonant unit module ⑥ is formed by the transmitting end resonant circuit and the receiving end resonant circuit working together.

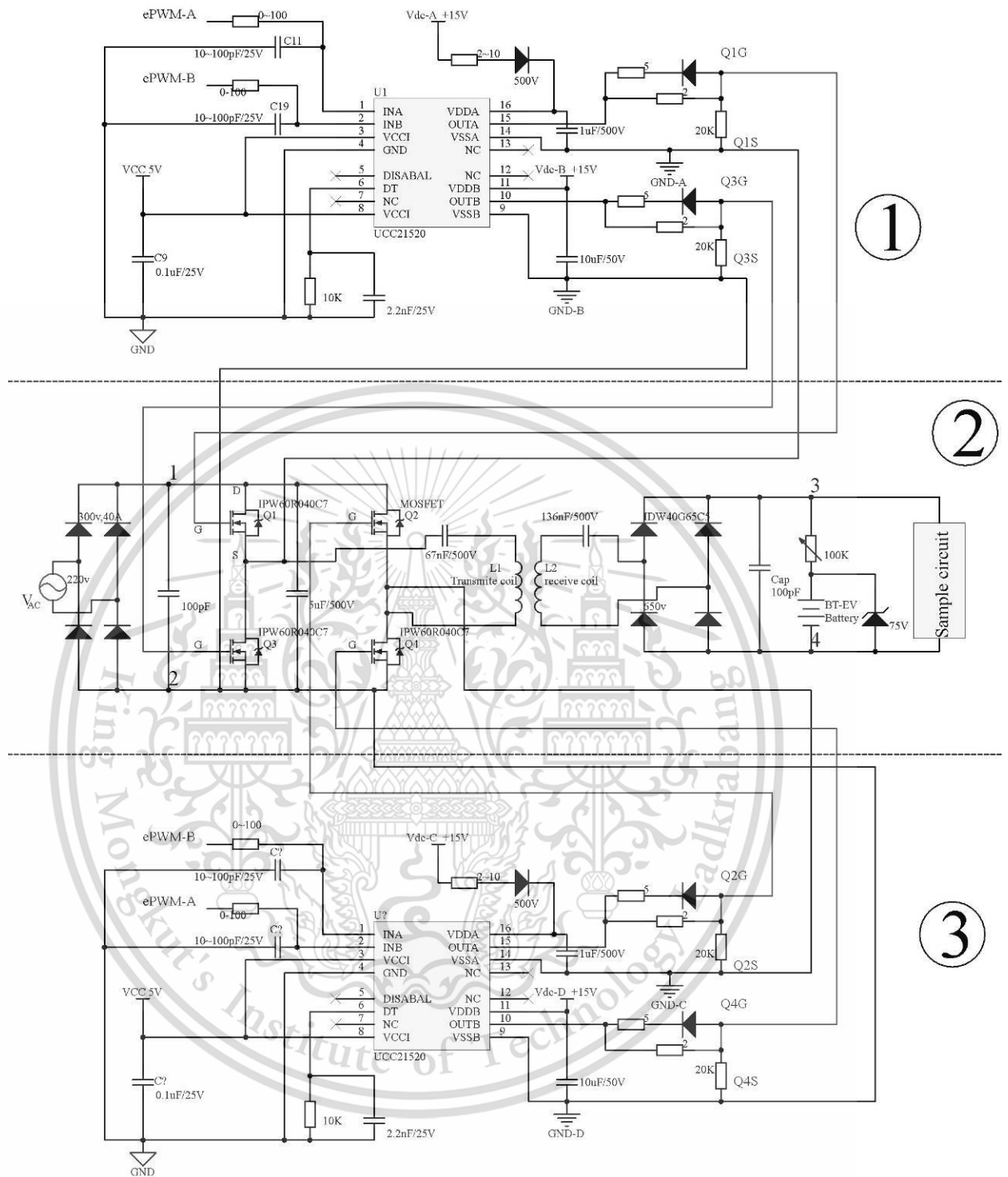


Fig.5-3-1 MCR-WPT System circuit diagram

The main circuit module ②, with circuit details shown in Fig. 5-3-2, converts the AC power supply  $V_{AC}$  into DC after passing through the rectifier filter circuit ④. The DC is then converted into AC with controllable frequency after passing through the full bridge inverter circuit module ⑤, and subsequently loaded into the

transmitter resonant circuit consisting of the transmitter coil L1 and the resonant capacitor C22.

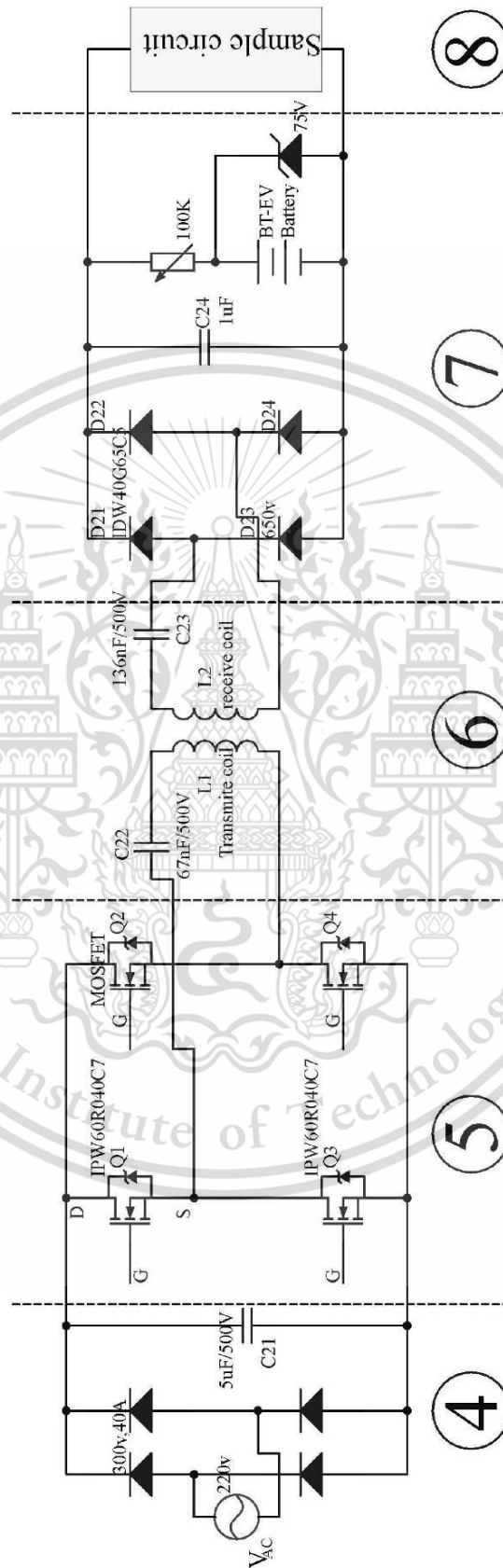


Fig.5-3-2 Detailed diagram of main circuit ②

This material is reserved for educational use only, not allowed for commercial use.

Forbidden to modify the content, and cite the document when use.

The full-bridge inverter circuit module ⑤ is mainly composed of four MOSFET transistors. MOSFET is selected, and the model chosen is ipw60r040c7. The rated working voltage and current are 650V and 50A, respectively. The dead time and the working frequency can reach up to 500kHz. The reason for choosing MOSFET over IGBT is that while IGBT has a higher withstand voltage capacity and can handle more current, its operational frequency is generally limited to tens of kHz. The operating frequency of a MOSFET is much higher than that of an IGBT, reaching up to MHz.

Module ⑦ is an output module, mainly consisting of a rectifier filter circuit, a voltage regulation circuit, and a load.

Among modules ⑦, D21~D24 are high-frequency rectifier diodes that must have a rated working voltage and current of 650V and 40A, respectively, and a rated working frequency of less than 1MHz. The model of the silicon carbide Schottky diode made by Infineon Technology Co. Ltd. in Germany is IDW40G65C5.

In module ④, VAC is single-phase mains power at 220V and 50Hz. The four rectifying diodes in the figure are required to have a rated working voltage of 300V, a current of 40A, and a frequency of 50Hz. In order to facilitate the purchase of components, this thesis selects a diode suitable for the high-frequency rectifying circuit: the Infineon Technology Co., Ltd. model IDW40G65C5, a silicon carbide Schottky diode made in Germany.

Sampling circuit ⑧ is used to collect the values of output voltage, current, and electric power.

Module ① and module ③ are grid driving circuits. Their main function is to amplify the signal transmitted from the control circuit so that it has enough power to drive the full bridge and generate high-frequency AC. The circuit design of the two modules is entirely consistent. The main chip used is UCC21520. This chip is characterized by complete isolation between input and output. It is an excellent gate drive chip. The difference is that the input signal of EPWM is switched. The output control signals are respectively connected to different MOSFET tubes of the inverter circuit ⑤. It should be noted that the two modules require a total of four completely independent 15V DC power supplies. There should be no connection between the four DC power supplies, and the grounding points should not be shared. Otherwise, it will cause an internal short circuit of the chip and burn it. For example, in Figure 5-3-

This material is reserved for educational use only, not allowed for commercial use.

3 of module ①, the signal output terminals q1s and q3s are respectively connected to the source of MOSFET 1 and 3 of the inverter circuit. During the operation of the inverter circuit, there is a potential difference between the two sources. If the grounding points of the two 15V DC power supplies are connected, it will cause a short circuit inside the chip and damage the chip.

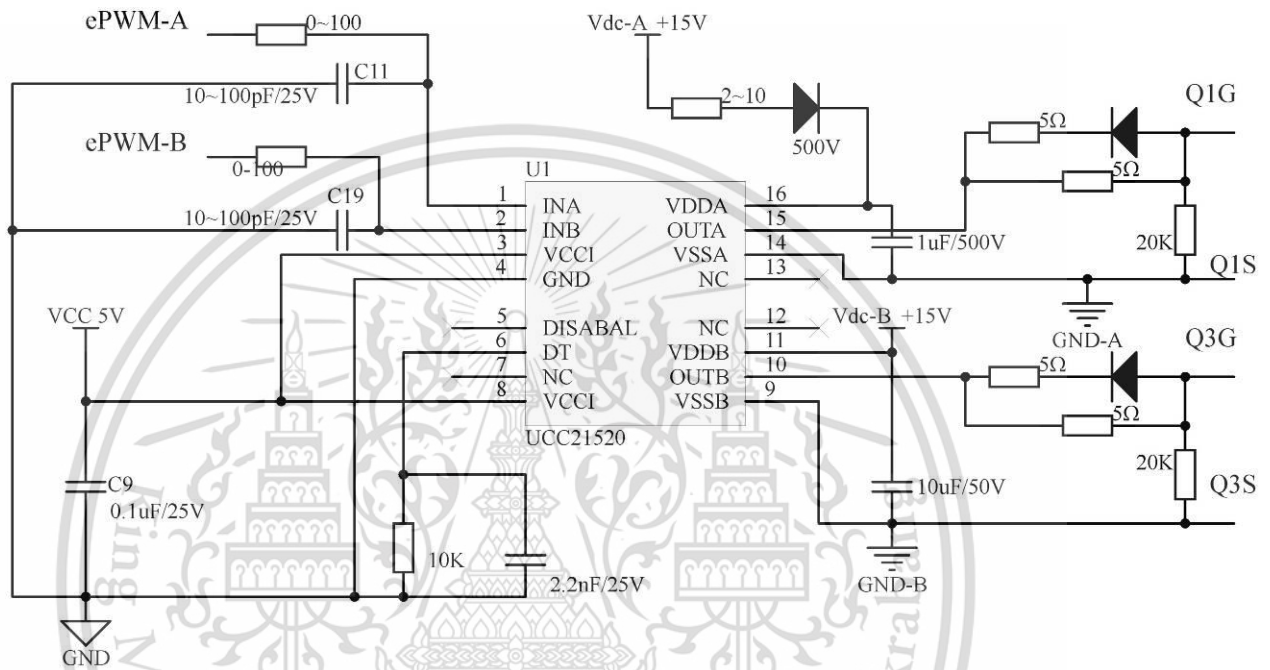


Fig.5-3-3 Detailed diagram of driving circuit ①

The input signals ePWM-A and ePWM-B are two complementary pulse signals with dead time, which are generated by the DSP (digital signal processing) module. The program in the DSP is developed by the upper computer and then loaded into the DSP chip TMS320F28335 (Texas Instruments, America).

The L1 and L2 in module ⑥ are designed in reference [31], as shown in the figure.

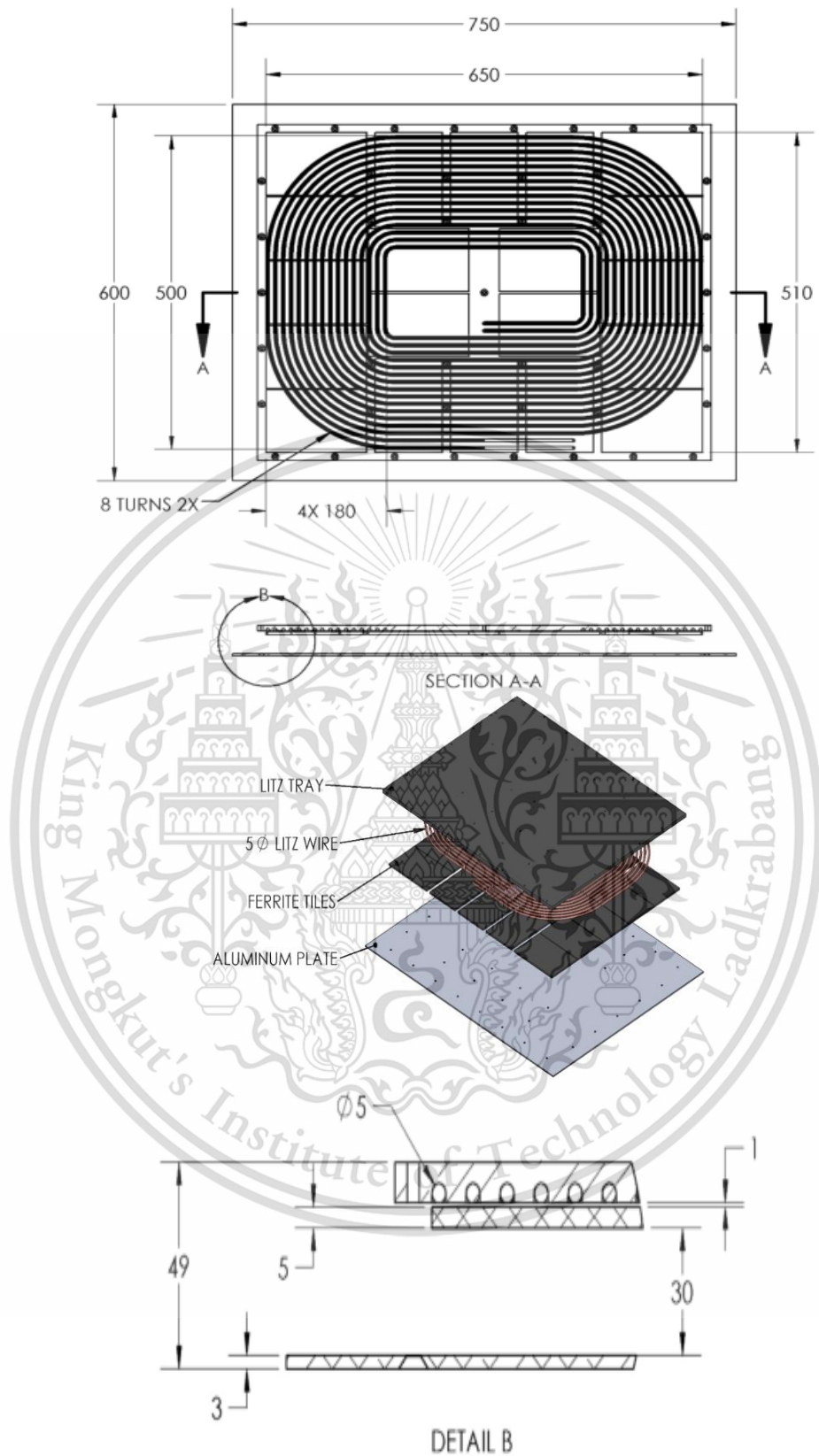


Fig.5-3-4 Structure diagram of transmitting coil [31]

This material is reserved for educational use only, not allowed for commercial use.

Forbidden to modify the content, and cite the document when use.

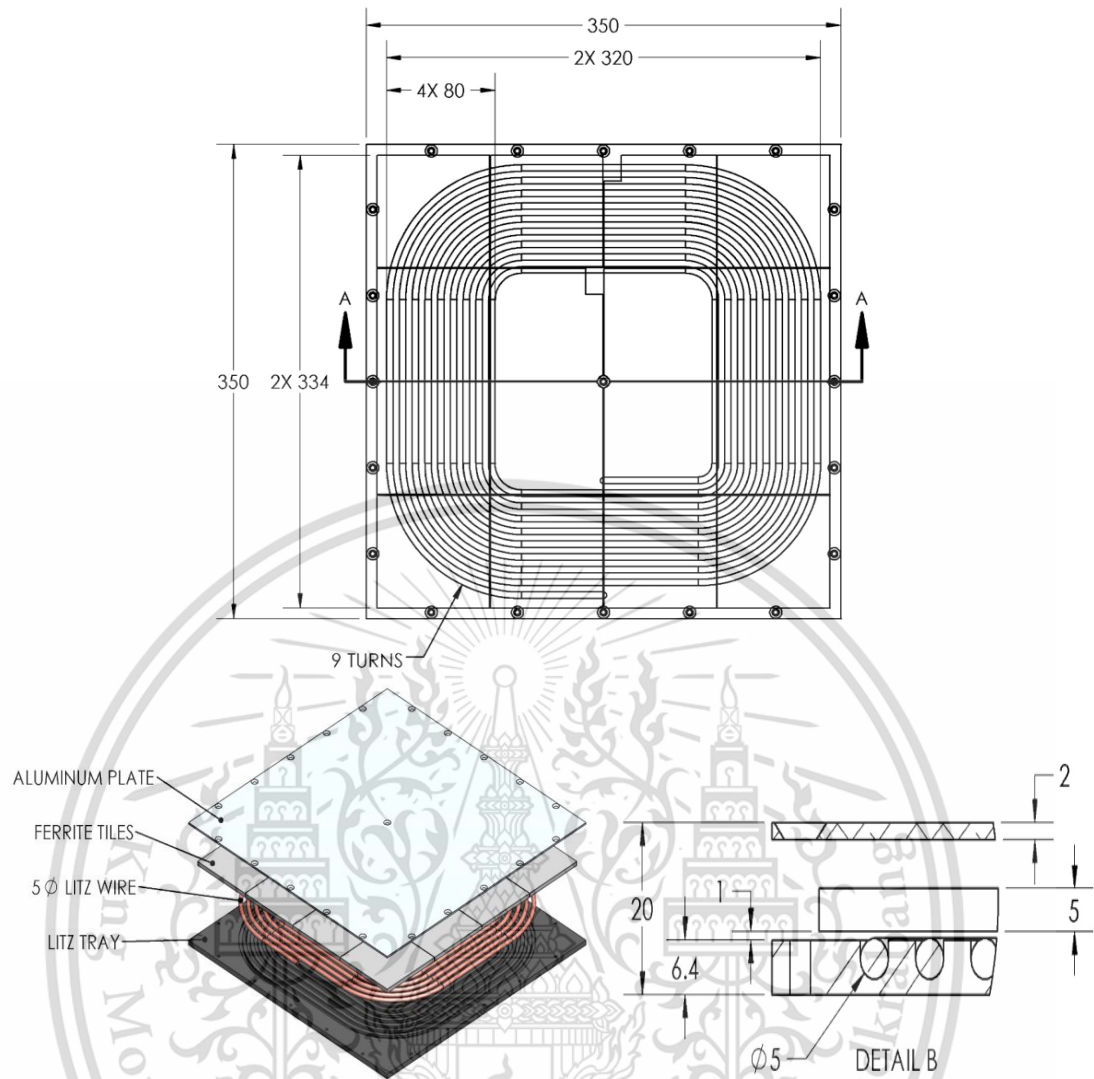


Fig.5-3-5 Structure diagram of transmitting coil [31]

According to the design of WPT-AAD and MCR-WPT in this chapter, the experimental test bench is illustrated in Fig. 5-3-6 and Fig. 5-3-7.

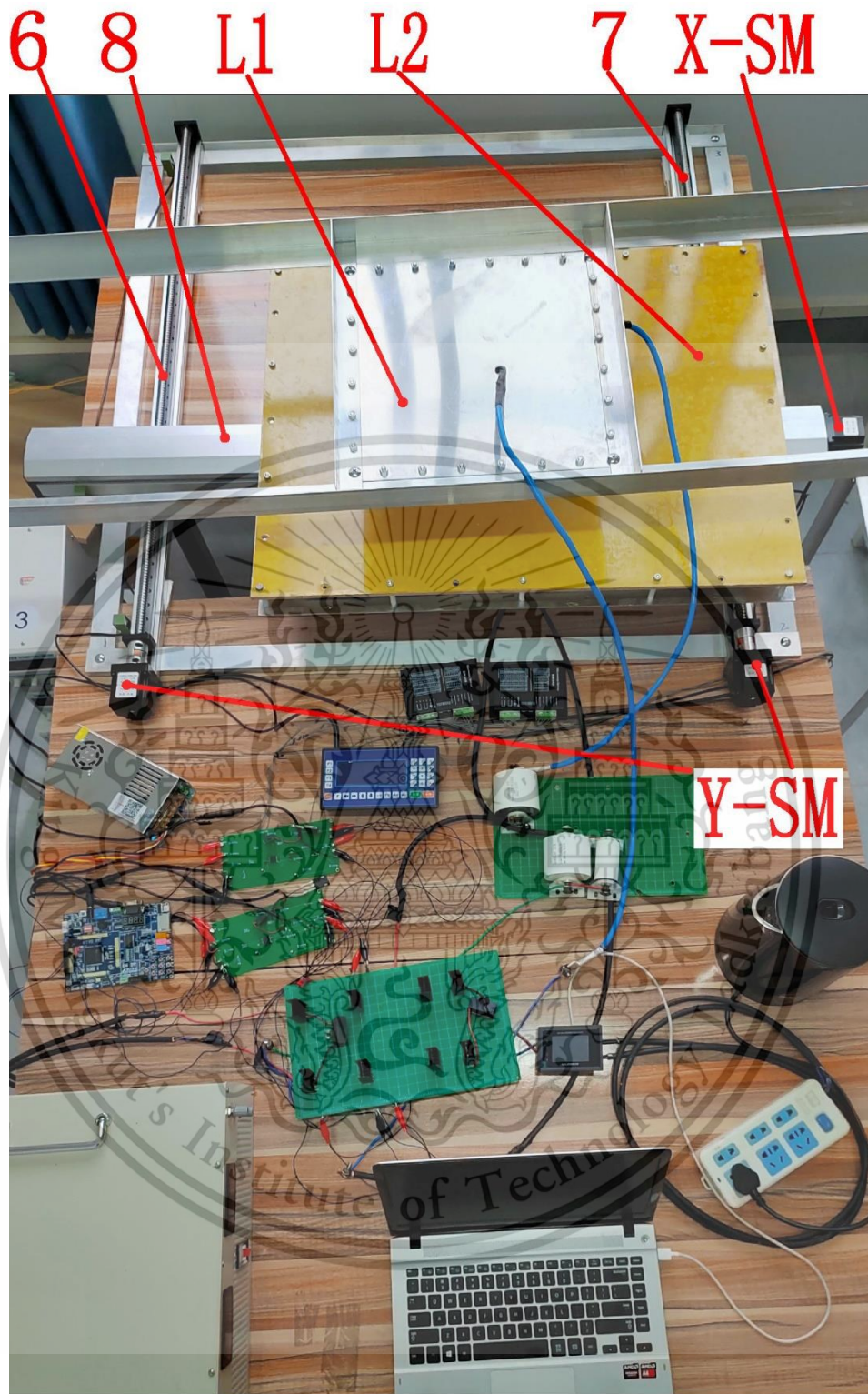


Fig.5-3-6 Photos of the WPT-AAD experimental bench

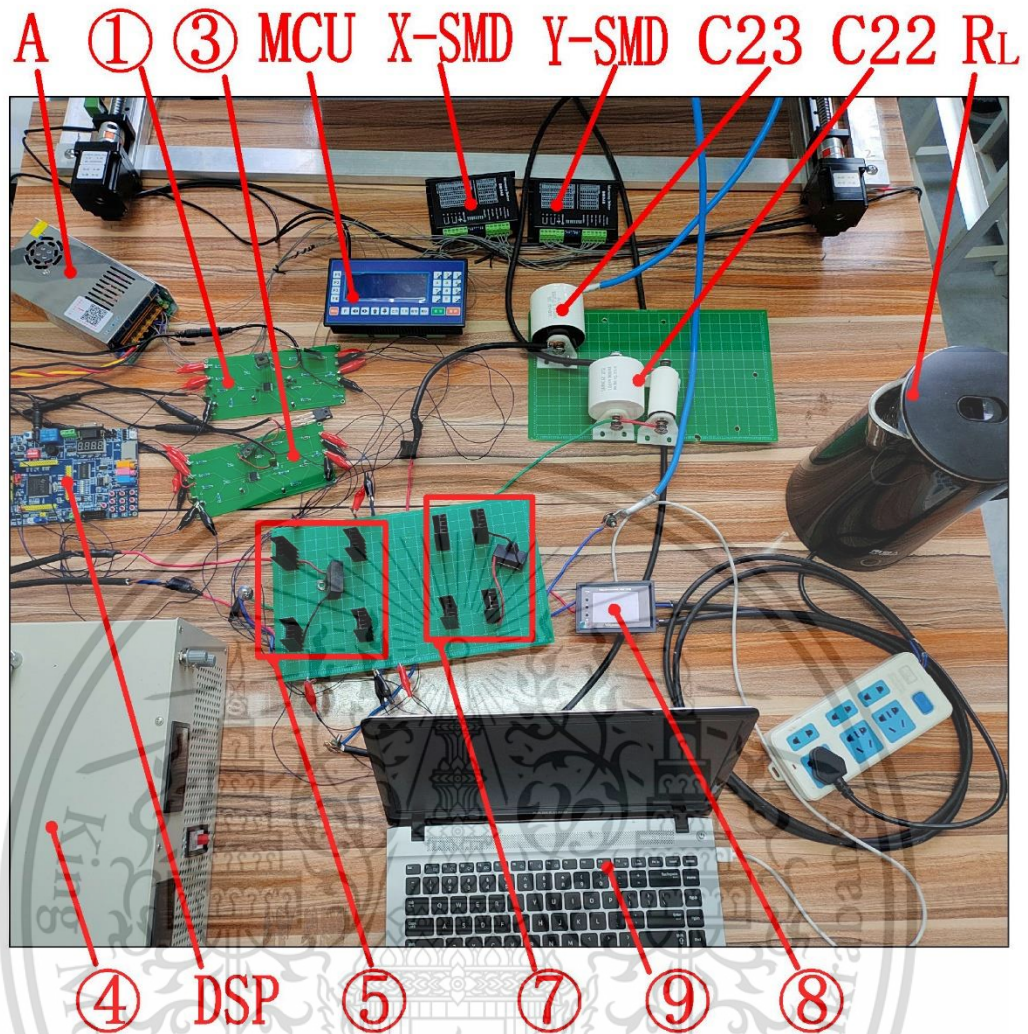


Fig.5-3-7 Partial detail of the WPT-AAD experimental bench

Fig.5-3-1 ~ Fig.5-3-7, notes:

- ① gate driving circuit one;
- ② the main circuit module for MCR-WPT
- ③ gate driving circuit two.
- ④ high power DC regulated power supply
- ⑤ Full bridge inverter circuit module;
- ⑥ the resonant circuit composed of L1, L2, C22, and C23.
- ⑦ Full bridge rectifier filter circuit in output module;
- ⑧ Output voltage and current sampling circuit;
- ⑨ Upper computer;
6. Y-axis screw rod one. (Numbers 6, 7, and 8 correspond to Fig.5-1-1)

This material is reserved for educational use only, not allowed for commercial use.

Forbidden to modify the content, and cite the document when use.

- 7. Y-axis screw rod two;
- 8. X-axis screw rod;
- L1. Transmitting-coil;
- L2. receiving-coil;
- C22. Resonant capacitance at the transmitter;
- C23. Resonant capacitance at the receiver;
- Y-SM. Stepper motor in Y-axis;
- X-SM. Stepper motor in X-axis;
- Y-SMD. Stepper motor driver in Y-axis;
- X-SMD. Stepper motor driver in X-axis;
- MCU. Microcontroller Unit;
- DSP. Digital Signal Processing
- RL. Load resistance in the output module;
- A.15V Four independent DC regulated power supplies

Direct measurement of coil inductance and calculation of resonant capacitance:

Use the induction meter to measure the transmitting coil L1 and receiving coil L2 three times each, and then calculate the average value. The measurements of each of the two coils are shown in Fig. 5-3-8 and Fig. 5-3-9.

The values obtained from three measurements of L1 are: 52.515  $\mu\text{H}$ ; 52.576  $\mu\text{H}$ ; 52.462  $\mu\text{H}$ . The average value is 52.518  $\mu\text{H}$ .

The values obtained from three measurements of L2 are 25.672  $\mu\text{H}$ , 25.642  $\mu\text{H}$ , and 25.728  $\mu\text{H}$ . The average value is calculated as 25.681  $\mu\text{H}$ .

After the inductance value of the coil is obtained, the matching resonant capacitance can be calculated by the following formula:

$$C_{22} = \frac{1}{(2\pi f)^2 L_1} \quad C_{23} = \frac{1}{(2\pi f)^2 L_2} \quad (5-3-1) [55]$$

where,

$C_{22}$ , is the resonant capacitance of the transmitting coil.

$C_{23}$  is the resonant capacitance of the receiving coil.

$f$ , resonant frequency, 85kHz; [55]

$L_1$  and  $L_2$  are the inductance coefficients of the transmitting coil and the receiving coil respectively; Substitute the directly measured value for calculation:

$$C_{22} = \frac{1}{(2 \times 3.14 \times 85000)^2 \times 52.518 \times 10^{-6}} = 66.757 \times 10^{-9} \quad (F)$$

$$C_{23} = \frac{1}{(2 \times 3.14 \times 85000)^2 \times 26.681 \times 10^{-6}} = 136.518 \times 10^{-9} \quad (F)$$

That is,  $C_{22}$ , which should be taken as 66.8nF;  $C_{23}$  should be 136.5nF



Fig.5-3-8 L1 inductance measurement Fig.5-3-9 L2 inductance measurement

#### 5.4 Analysis of MCR-WPT experimental data

As shown in Fig. 5-3-2, the DC voltage and current output by module ④ (rectifier and filter module) are equivalent to the input voltage and current of the entire WPT system, as recorded in Fig. 5-1-2. Similarly, in Fig. 5-3-7, module ⑧ represents the same sampling module, with the collected voltage and current being the output of the entire MCR-WPT system, as recorded in the same figure. In Fig. 5-3-7, adjust the position of L1 to align it with the center point of L2. This material is reserved for educational use only, not allowed for commercial use.

Forbidden to modify the content, and cite the document when use.

are 10 cm, 15 cm, 20 cm, 25 cm, and 30 cm, respectively. Adjust the input voltage of WPT and adjust the frequency of the EPWM output using a DSP. This frequency is actually the driving frequency ( $f$ ) of the high-frequency inverter circuit in module ⑤. The data from several experiments are presented in the following tables.

**Table5-4-1. MCR-WPT experiment 1**

( $D=20$  cm,  $U_i=200$  V,  $R_L=70 \Omega$ )

Drive frequency $f$ , (kHz)	Input voltage $U_i$ , (V)	Input current $I_i$ , (A)	Output voltage $U_o$ , (V)	Output current $I_o$ , (A)	WPT efficiency $\eta$ , (%)
80.0	200	3.53	173.9	2.5	61.21
81.0	200	3.66	177.9	2.5	61.74
82.0	200	3.74	182.2	2.6	63.39
83.0	200	3.89	188.2	2.7	65.07
84.0	200	4.13	196.4	2.8	66.69
85.0	200	4.47	205.8	2.9	67.66
85.1	200	4.49	206.6	3.0	67.91
85.2	200	4.55	208.5	3.0	68.22
85.3	200	4.83	215.3	3.1	68.54
85.4	200	4.52	208.0	3.0	68.34
85.5	200	4.46	206.0	2.9	67.99
85.6	200	4.39	203.8	2.9	67.57
86.0	200	4.21	198.4	2.8	66.77
87.0	200	4.08	193.2	2.8	65.33
88.0	200	3.91	186.4	2.7	63.44
89.0	200	3.79	181.1	2.6	61.82

Data in the table, except WPT efficiency  $\eta$ . All the other data were directly recorded during the experiment; WPT efficiency  $\eta$ , is calculated by the following formula:

$$\eta = \frac{P_o}{P_i} = \frac{U_o I_o}{U_i I_i} \quad (5-4-1)$$

where,  $P_i$  input power,  $P_o$  output power,  $U_i$  input voltage,  $I_i$  input current,  $U_o$  output voltage,  $I_o$  output current.

**Table5-4-2. MCR-WPT experiment 2**

( $D=20$  cm,  $U_i = 300$  V,  $R_L = 70 \Omega$ )

Drive frequency $f$ , (kHz)	Input voltage $U_i$ , (V)	Input current $I_i$ , (A)	Output voltage $U_o$ , (V)	Output current $I_o$ , (A)	WPT efficiency $\eta$ , (%)
80.0	300	5.10	269.3	3.8	67.70
81.0	300	5.18	272.4	3.9	68.23
82.0	300	5.28	278.3	4.0	69.89
83.0	300	5.40	284.7	4.1	71.56
84.0	300	5.67	295.2	4.2	73.19
85.0	300	6.01	305.9	4.4	74.15
85.1	300	6.01	306.5	4.4	74.41
85.2	300	6.08	308.8	4.4	74.72
85.3	300	6.41	317.7	4.5	75.04
85.4	300	6.09	309.4	4.4	74.85
85.5	300	6.02	306.9	4.4	74.48
85.6	300	5.95	304.3	4.3	74.07
86.0	300	5.77	297.9	4.3	73.26
87.0	300	5.65	292.0	4.2	71.83
88.0	300	5.48	283.7	4.1	69.94
89.0	300	5.34	276.9	4.0	68.32

**Table5-4-3. MCR-WPT experiment 3**

( $D=20$  cm,  $U_i = 400$  V,  $R_L = 70 \Omega$ )

Drive frequency $f$ , (kHz)	Input voltage $U_i$ , (V)	Input current $I_i$ , (A)	Output voltage $U_o$ , (V)	Output current $I_o$ , (A)	WPT efficiency $\eta$ , (%)
80.0	400	6.69	369.9	5.3	73.09
81.0	400	6.68	371.2	5.3	73.61

This material is reserved for educational use only, not allowed for commercial use.

Forbidden to modify the content, and cite the document when use.

82.0	400	6.83	379.5	5.4	75.28
83.0	400	6.93	386.5	5.5	76.95
84.0	400	7.27	399.9	5.7	78.58
85.0	400	7.59	411.1	5.9	79.54
85.1	400	7.54	410.5	5.9	79.79
85.2	400	7.65	414.2	5.9	80.11
85.3	400	8.00	424.6	6.1	80.43
85.4	400	7.61	413.6	5.9	80.24
85.5	400	7.61	412.4	5.9	79.87
85.6	400	7.45	407.2	5.8	79.45
86.0	400	7.35	402.4	5.7	78.65
87.0	400	7.16	393.4	5.6	77.21
88.0	400	7.01	384.5	5.5	75.33
89.0	400	6.93	378.1	5.4	73.71

Take the above three experimental data as abscissa with drive frequency  $f$  and WPT efficiency  $\eta$  is the vertical coordinate, and is drawn as a curve, as shown in Fig.5-4-1

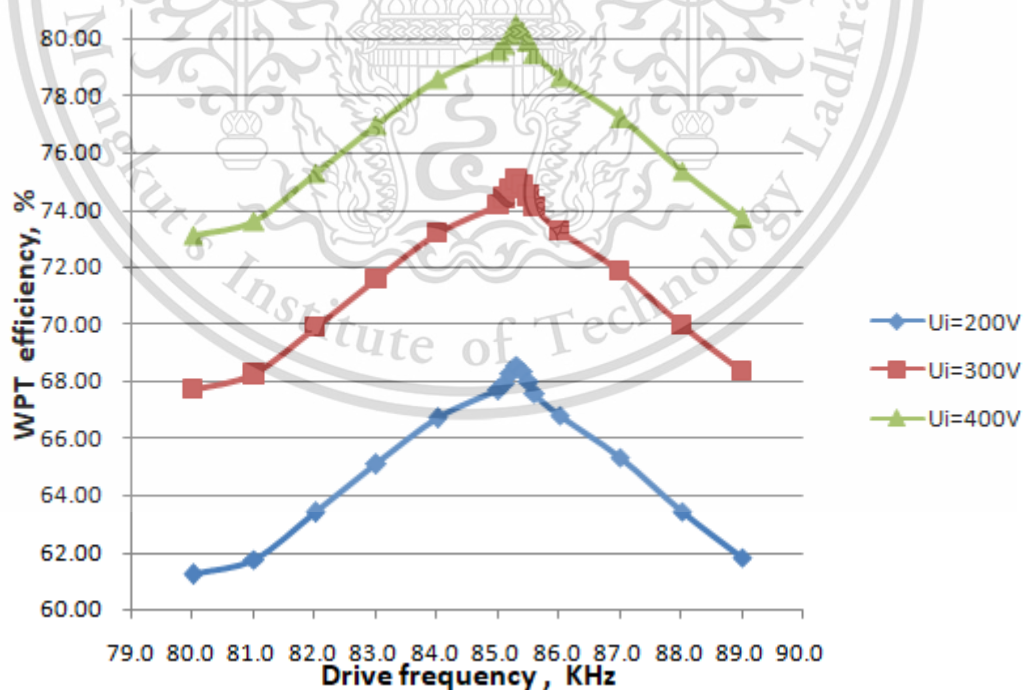


Fig.5-4-1 Diagram for WPT drive frequency, input voltage and efficiency

Combining Fig. 5-4-1 and analyzing the experimental data from 1 to 3, it can be  
This material is reserved for educational use only, not allowed for commercial use.

Forbidden to modify the content, and cite the document when use.

observed that the energy transmission efficiency of WPT follows a normal distribution between the driving frequencies of 80 kHz and 90 kHz. The maximum transmission efficiency is achieved at a driving frequency of 85.3 kHz. This driving frequency can be considered the actual resonant frequency of the system, which is consistent with the theoretical design resonant frequency of 85.0 kHz, with only a 0.3 kHz error. This discrepancy may be attributed to measurement errors in the inductance of the transmitting coil L1 and the receiving coil L2, as well as errors between the nominal and actual values of the resonant capacitance C22 and C23. This error is not significant and is still within the acceptable range for the project.

In these three experiments, a positive correlation was observed between the transmission efficiency and the input voltage. The higher the input voltage, the greater the transmission efficiency. Next, the experiment on the relationship between input voltage and transmission efficiency is conducted with a driving frequency of 85.3 kHz.

**Table5-4-4. MCR-WPT experiment 4**

(D=20 cm,  $f=85.3$  kHz,  $R_L =70 \Omega$ )

Drive frequency $f$ , (kHz)	Input voltage $U_i$ , (V)	Input current $I_i$ , (A)	Output voltage $U_o$ , (V)	Output current $I_o$ , (A)	WPT efficiency $\eta$ , (%)
85.3	200	4.83	215.3	3.1	68.54
85.3	225	5.21	239.4	3.4	69.87
85.3	250	5.58	263.9	3.8	71.34
85.3	275	5.96	289.9	4.1	73.23
85.3	300	6.33	315.8	4.5	75.04
85.3	325	6.71	343.1	4.9	77.12
85.3	350	7.12	371.1	5.3	78.93
85.3	375	7.63	399.7	5.7	79.78
85.3	400	7.94	422.9	6.0	80.43
85.3	425	8.32	446.1	6.4	80.41
85.3	450	8.72	469.9	6.7	80.40
85.3	475	9.10	493.3	7.0	80.41
85.3	500	9.49	516.8	7.4	80.41

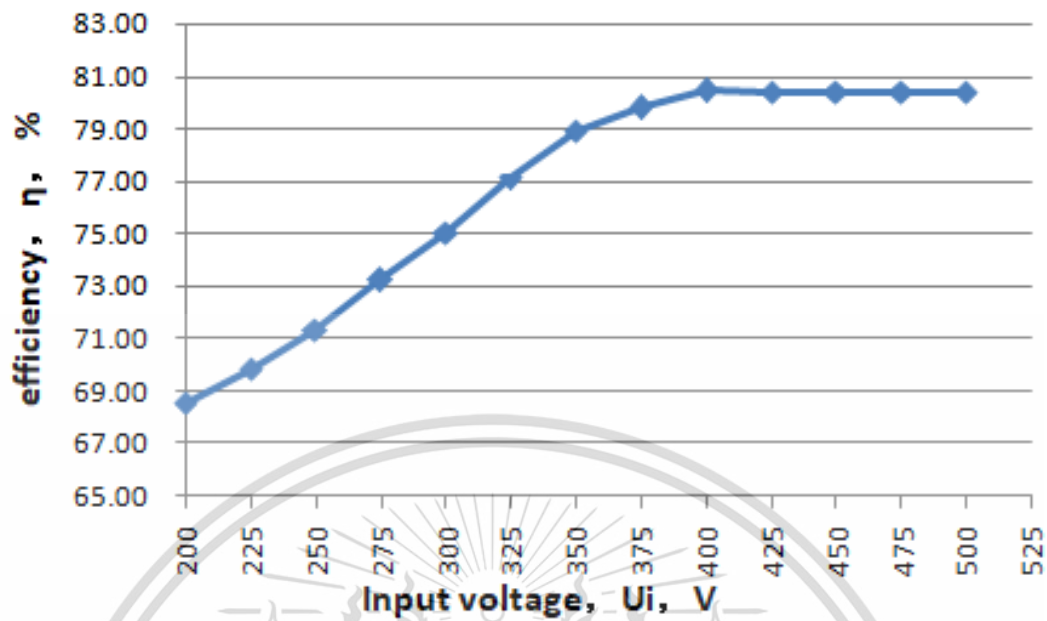


Fig.5-4-2 Diagram for input voltage and efficiency

Combining Fig. 5-4-2 with the data from Experiment 4, it is evident that when the drive frequency equals the resonant frequency, the input voltage is positively correlated with system efficiency. However, as the input voltage exceeds 400V, the enhancement of system efficiency slows down significantly. When the input voltage ranges between 450V and 500V, the system efficiency remains almost unchanged and stable at about 80.4%. This observation deviates somewhat from the theoretical analysis presented in Chapter 3. The theoretical analysis in Chapter 3 suggests that the efficiency of the resonant unit is not influenced by the input DC voltage but is instead linked to the coil mutual inductance, equivalent resistance, load resistance, and driving frequency. The efficiency of the MCR-WPT system is primarily impacted by the efficiency of the resonant unit, the power loss of the high-frequency inverter unit, and the power loss of the rectifier filter unit. However, the latter two factors account for a small proportion and can be ignored; therefore, the efficiency of the MCR-WPT system can be considered to be mainly affected by the efficiency of the resonant unit. The reason may be related to the structure of the transmitting coil and the receiving coil. Only when the input voltage is relatively high can power be transmitted wirelessly with high efficiency within a distance of 20 cm. When the input voltage is lower than 400V, the magnetic induction intensity generated by the transmitting coil is relatively small.

Consequently, the wireless transmission distance of power is limited, leading to a decrease in the overall efficiency of the system.

Analyzing the data from the MCR-WPT Experiment 5, Table 5-4-5 and Fig. 5-4-3 also confirmed this conclusion: the distance between the two coils is within the range of  $D=10\text{ cm}\sim 25\text{ cm}$ . When the input voltage ( $U_i$ ) is lower than 400V, the efficiency ( $\eta$ ) of the MCR-WPT system is significantly influenced by both  $D$  and  $U$ . When the input voltage reaches 400V, the efficiency ( $\eta$ ) of the MCR-WPT system is almost independent of the input voltage ( $U_i$ ), which aligns with the theoretical analysis in Chapter 3.

**Table5-4-5. MCR-WPT experiment 5**

( $D=10\sim 25\text{ cm}$ ,  $f=85.3\text{ kHz}$ ,  $R_L = 70\ \Omega$ )

Distance between two coils $D$ , (cm)	Input voltage $U_i$ , (V)	Input current $I_i$ , (A)	Output voltage $U_o$ , (V)	Output current $I_o$ , (A)	WPT efficiency $\eta$ , (%)
10	200	4.83	227.0	3.2	76.21
15	200	4.83	224.7	3.2	74.66
20	200	4.83	215.3	3.1	68.54
25	200	4.83	197.8	2.8	57.87
10	300	6.33	324.3	4.6	79.12
15	300	6.33	322.1	4.6	78.04
20	300	6.33	315.8	4.5	75.05
25	300	6.33	299.1	4.3	67.29
10	400	7.94	423.2	6.0	80.55
15	400	7.94	422.9	6.0	80.44
20	400	7.94	422.9	6.0	80.44
25	400	7.94	409.9	5.9	75.58
10	500	9.49	518.9	7.4	81.07
15	500	9.49	518.2	7.4	80.86
20	500	9.49	516.9	7.4	80.46
25	500	9.49	509.8	7.3	78.26

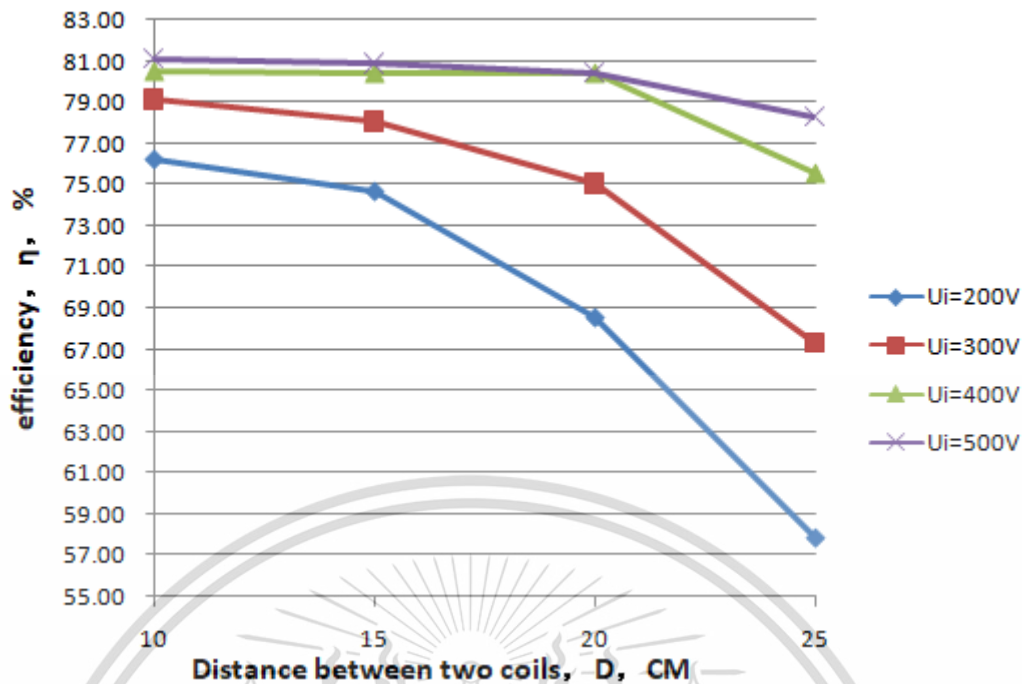


Fig.5-4-3 Diagram for Distance between two coils and efficiency

Analyzing the data in Table 5-4-5 of MCR-WPT experience 5, when the input DC voltage is 500V and the distance between the receiving coil and the transmitting coil is 20cm, the output power is 3.82 kW, and the efficiency of the wireless charging system is 80.46%. This fully meets the requirement that the total power storage capacity of the power battery of the elderly EV designed in this thesis is 38 kWh, and it can complete the charging from the original 20% to 90% in 8 hours (a wireless charging system with a charging power of 3.33 kW is required).

### 5.5 Analysis of mutual inductance experimental data

As depicted in Fig. 5-3-7 and Fig. 5-3-7, by programming the MCU, it can meticulously record the data of each coordinate point of the receiving coil along with the corresponding input and output voltage and current values during the experiment. The center point of the initial position of the transmitting coil is the origin of the coordinates. The data is organized in Table5-5-1.

**Table5-5-1. Mutual induction distribution experiment**(D=20 cm,  $U_i=400$  V,  $f=85.3$  kHz,  $R_L =70 \Omega$ )

X coordinate (m)	Y coordinate (m)	Input voltage $U_i$ , (V)	Input current $I_i$ , (A)	Output voltage $U_o$ , (V)	Output current $I_o$ , (A)	WPT efficiency $\eta$ , (%)	Mutual Inductance $M$ , (H)
-0.397	-0.368	400	7.94	267.97	3.83	32.30	2.64E-06
-0.370	-0.368	400	7.95	278.59	3.98	34.87	2.80E-06
-0.342	-0.368	400	7.94	287.22	4.10	37.09	2.94E-06
-0.315	-0.368	400	7.94	292.55	4.18	38.52	3.03E-06
-0.287	-0.368	400	7.94	296.67	4.24	39.59	3.10E-06
-0.260	-0.368	400	7.95	299.47	4.28	40.30	3.14E-06
-0.233	-0.368	400	7.93	300.47	4.29	40.66	3.17E-06
-0.205	-0.368	400	7.94	302.13	4.32	41.06	3.19E-06

Data in Table 5-5-1, except for WPT efficiency ( $\eta$ ) and mutual induction ( $M$ ), were directly collected during the experiment. WPT efficiency ( $\eta$ ) is calculated using equation (5-4-1), similar to several experiments mentioned above. The  $M$  is determined by substituting formula (5-5-1) into the data collected from the experiment.

Formula (5-5-1) is derived from the formula (3-2-6) in Chapter 3 by performing the necessary calculations. For easier reference, the formula (3-2-6) is restated below: {3-2-6}.

$$\eta = \frac{\omega_d^2 M^2 R_L}{(R_2 + R_L)(\omega_d^2 M^2 + R_1 R_L + R_1 R_2)} \quad (3-2-6)$$

$$M = \sqrt{\frac{\eta R_1 (R_2 + R_L)^2}{\omega_d^2 R_L - \omega_d^2 \eta (R_2 + R_L)}} \quad (5-5-1)$$

Since there is a large amount of data in Table 5-5-1, to analyze the data more intuitively, the data from the table is visualized using Python software, as depicted in Fig. 5-5-1 and Fig. 5-5-2. Simultaneously, to aid in the analysis, the data on the distribution of  $M$  near the XY coordinate axis in Table 5-5-1 is represented in a two-dimensional curve using Microsoft Excel software, as illustrated in Fig. 5-5-3 and Fig. 5-5-4.

This material is reserved for educational use only, not allowed for commercial use.

Forbidden to modify the content, and cite the document when use.

Fig. 5-5-1 to Fig. 5-5-4 depict the experimental data from Table 5-5-1, generated using computer software. It is not difficult to see that the four figures are very similar to Figure 3-7-1~Fig. 3-7-4 from the theoretical analysis in Chapter 3 above.

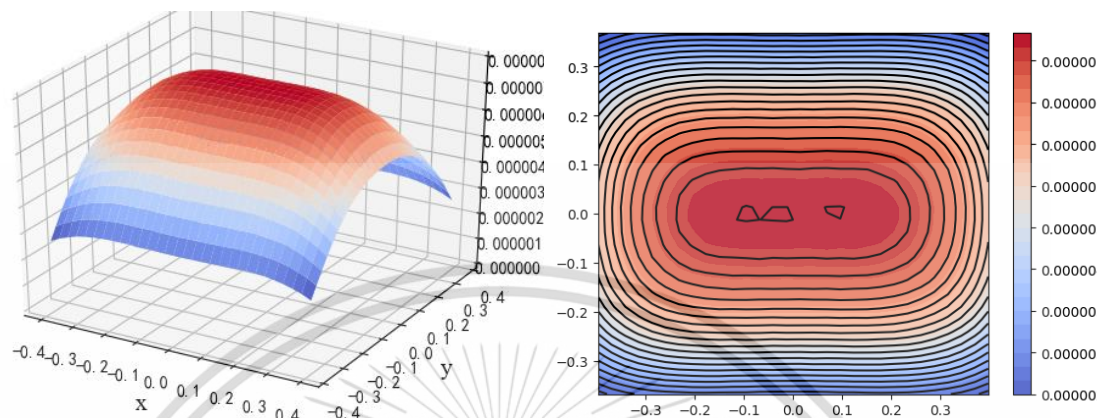


Fig.5-5-1 mutual inductance distribution map

Fig.5-5-2 mutual inductance distribution contour map

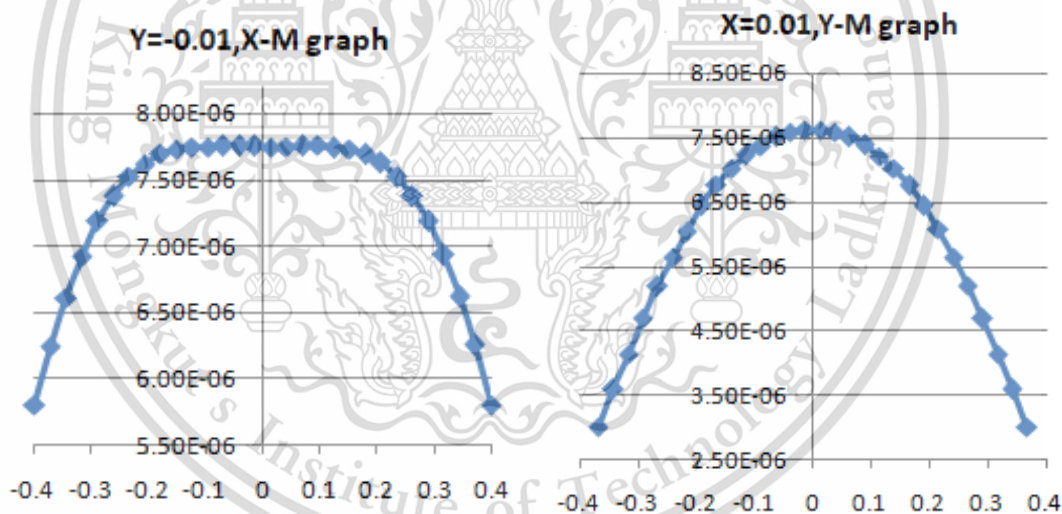


Fig.5-5-3 Y=0, X- mutual inductance graph

Fig.5-5-4 X=0, Y- mutual inductance graph

Looking up Table5-5-1, the maximum value of mutual induction  $M$  is as follows:

$$M_{max} = 7.76 \times 10^{-6} \quad \text{H} \quad (5-5-2)$$

The maximum value of  $M$  corresponds to WPT efficiency,  $\eta$ . The maximum value  $\eta$  is 80.38%. This maximum value of  $M$ , and the maximum value calculated by This material is reserved for educational use only, not allowed for commercial use.

Forbidden to modify the content, and cite the document when use.

theoretical analysis in Chapter 3 ( $M_{max}=7.87 \times 10^{-6}$  H), differs by  $0.11 \times 10^{-6}$  H. The reason for the error may be attributed to imperfections in the design structure of the transmitting coil and the receiving coil, or inadequate magnetic field shielding. However, the error ratio is approximately 1.4%, which is small and does not significantly impact the research on this topic.

Therefore, the theoretical analysis of mutual induction distribution in Chapter 3 of this thesis can be considered validated by the experimental data presented in this chapter.

## 5.6 Analysis of WPT- AAD experimental data

Next, the following experiments are carried out, applying the MSRA proposed in Chapter 4 to the WPT-AAD designed in Chapter 5 to find the location of the maximum mutual inductance coefficient.

In order to reduce the amount of data, only 600 iterations were performed during the experiment, resulting in 600 sets of data, as shown in Table 5-6-1.

Table5-6-1 MSRA be applied to WPT-AAD for finding the position of the maximum mutual inductance

X coordinate (m)	Y coordinate (m)	Input voltage $U_i$ , (V)	Input current $I_i$ , (A)	Output voltage $U_o$ , (V)	Output current $I_o$ , (A)	WPT efficiency $\eta$ , (%)	Mutual Inductance $M$ , (H)
-0.312	-0.139	400	7.94	405.97	5.80	74.13	6.48E-06
-0.292	-0.139	400	7.94	408.53	5.84	75.07	6.65E-06
-0.272	-0.139	400	7.94	410.51	5.86	75.80	6.78E-06
-0.252	-0.139	400	7.95	412.22	5.89	76.37	6.89E-06
-0.232	-0.139	400	7.95	413.49	5.91	76.82	6.97E-06
-0.212	-0.139	400	7.93	414.05	5.91	77.18	7.04E-06
-0.192	-0.139	400	7.94	414.90	5.93	77.39	7.09E-06
-0.172	-0.139	400	7.94	415.11	5.93	77.51	7.11E-06

Data in Table 5-6-1, except for WPT efficiency ( $\eta$ ) and mutual induction ( $M$ ), was directly collected during the experiment. WPT efficiency ( $\eta$ ), as in the above

experiments, is calculated using formula (5-4-1). The  $M$  is calculated by substituting formula (5-5-1) into the data collected in the experiment.

Due to the large amount of data in Table 5-6-1, to facilitate a more intuitive analysis, the XY coordinates from the table are plotted into a two-dimensional curve using Microsoft Excel software. This visualization helps to clearly depict the path followed by MSRA in search of the location with the highest output power, representing the trajectory of MSRA in search of the point with the maximum mutual induction  $M$ , as illustrated in Figure 5-6-1.

In Fig. 5-6-1, the yellow ">" indicates the starting point of the MSRA search, while "X" indicates the target point searched by MSRA, which is also the endpoint of the search. According to Table 5-6-1, the target point location searched by MSRA is (-0.057, 0.002). The corresponding MCR-WPT efficiency is 80.41%, and the mutual induction  $M$  is 7.76E-06. From the previous experiments, it can be seen that these values fall within the defined interval  $\eta$  or  $M_{max}$ .

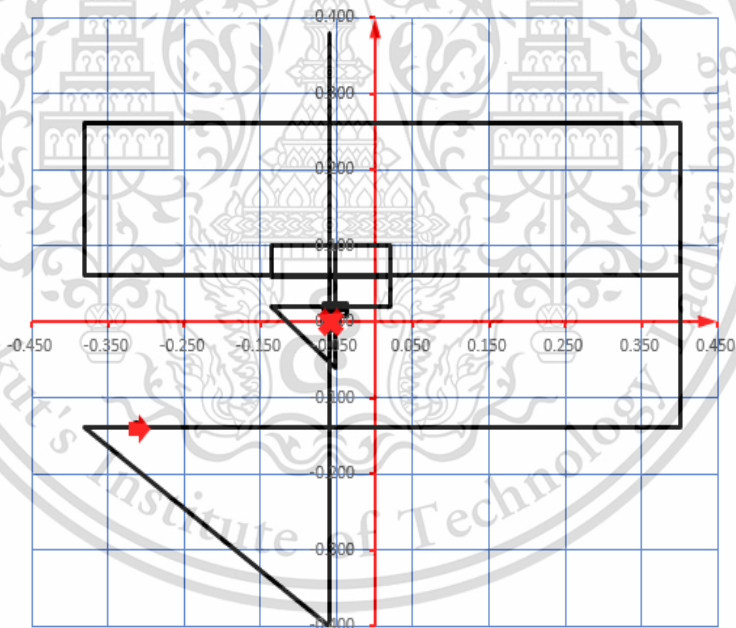


Fig.5-6-1 Track Roadmap of MSRA being applied to WPT-AAD for Finding the position of the maximum mutual inductance

Through experiments, it has been proven that the application of MSRA in WPT-AAD is reasonable and reliable. Simultaneously, it also validates that the design of all hardware and software in this project is correct.

## Chapter 6

### Conclusion and Suggestion

The focus of this thesis is to study and design the Wireless Power Transfer with Automatic alignment Device (WPT-AAD) for elderly EV. First, this thesis describes the current market products in the elderly EV industry. It is understood that the current elderly EV products in the market do not meet the transportation needs of the elderly in urban areas. The process of charging these vehicles is considered unsafe and inconvenient for the elderly. Therefore, it is proposed to research and design a car specifically tailored for the elderly, capable of navigating city streets and equipped with an automatic positioning wireless charging system. This thesis focuses on the field of the WPT-AAD, discussing the current research status all over the world. It argues that studying an elderly car with WPT-AAD is necessary, feasible, and innovative. The primary focus of this thesis is WPT-AAD.

Secondly, the fundamental parameters of the chassis of an elderly EV are preliminarily selected in this thesis. This selection serves as a reference for the detailed design of an elderly EV to meet the travel requirements of the elderly in urban areas. Subsequently, the driving force, selection of the driving motor, and power battery capacity of the elderly EV are meticulously calculated. These calculations lay the groundwork for designing a wireless charging system with an automatic alignment function.

Thirdly, this thesis briefly introduces the structure and working principle of the electric vehicle magnetic coupling resonant radio energy transmission system. According to Biot-Savart's law, the magnetic field generated by the energy transmitting coil in the wireless charging system is carefully analyzed, reasoned, and calculated in detail. The mathematical expression for the magnetic induction intensity generated by the transmitting coil at any point in space is derived. Then, the distribution map of the magnetic induction intensity in the magnetic field space is created using the computer software Python. This map serves as the foundation for analyzing the mutual inductance between the transmitting coil and the receiving coil.

Fourth, this thesis analyzes the range of random parking positions of elderly EV in parking spaces and determines the range of random positions of MCR-WPT receiving coils. Subsequently, the distribution of mutual inductance between the transmitting

This material is reserved for educational use only, not allowed for commercial use.

coil and the receiving coil is calculated in detail as the relative position of the transmitting coil and the receiving coil changes within this range. Finally, the position of maximum mutual inductance distribution is derived. The research on the distribution of mutual inductance between the transmitting coil and receiving coil in space provides a theoretical basis for the design of MCR-WPT system.

Fifthly, this thesis innovatively proposes a new optimization algorithm, namely, the Maritime Search and Rescue Algorithm (MSRA), and applies this algorithm, together with SMA and GeneticA, to five well-known optimization algorithm test functions (Ackley, Rastrigin, Sphere, Schaffer, Schwefel), and compares and analyzes the operational results. It is concluded that MSRA has excellent performance. The thesis then discusses the application of MSRA to WPT-AAD to determine the position of the maximum mutual inductance  $M$  and achieve the automatic alignment function of wireless charging.

Sixth, based on the theoretical analysis and control requirements of the MSRA applied to WPT-AAD, this thesis designs the hardware system of WPT-AAD and compiles the control program for MSRA applied to WPT-AAD.

Finally, this thesis constructed the WPT-AAD experimental bench and conducted five MCR-WPT experiments with various parameters on the bench. Subsequently, the WPT-AAD experiment was performed using appropriate parameters from the MCR-WPT experiments. In these six experiments, the experimental data were recorded in detail and analyzed.

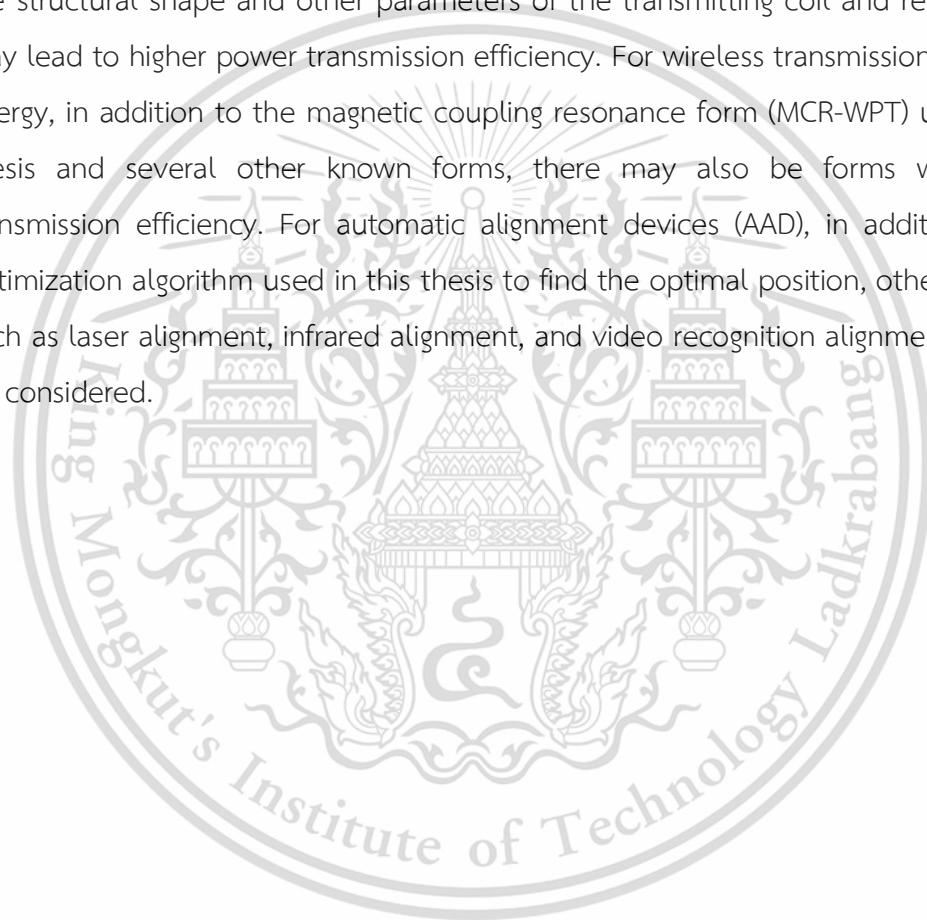
In general, in this thesis, through theoretical analysis and experiments, the correctness of MSRA was verified. The rationality of applying MSRA to WPT-AAD control was verified, and the correctness of the theoretical analysis of mutual inductance distribution between the transmitting coil and receiving coil in the WPT system was confirmed. It was demonstrated that the WPT system with AAD meets the requirements of an elderly EV. The WPT-AAD hardware system designed in this thesis is deemed entirely correct and feasible. Moreover, it is foreseeable that the MSRA will have good prospects for promotion and application.

Several problems remain unresolved. First, due to lack of funds, we do not have the conditions to actually manufacture a prototype elderly EV for the based on the design of this thesis. Without any conditions, the WPT designed in this thesis is installed on the prototype vehicle for debugging. Second, for the MSRA proposed in this thesis, This material is reserved for educational use only, not allowed for commercial use.

Forbidden to modify the content, and cite the document when use.

we do not have the experimental verification conditions for other promotion and application projects such as searching for the location of the leakage of hazardous chemicals and toxic volatile substances, sea surface search and rescue. Third, it is necessary to optimize the mathematical model of MSRA and study the mathematical model and verification analysis of MSRA applied to high-dimensional optimization problems. Fourth, while planning the route, the MSRA does not have the function of avoiding obstacles and this feature needs to be further developed.

For in-depth research on this topic, we give some suggestions. For WPT, changing the structural shape and other parameters of the transmitting coil and receiving coil may lead to higher power transmission efficiency. For wireless transmission of electric energy, in addition to the magnetic coupling resonance form (MCR-WPT) used in this thesis and several other known forms, there may also be forms with higher transmission efficiency. For automatic alignment devices (AAD), in addition to the optimization algorithm used in this thesis to find the optimal position, other solutions such as laser alignment, infrared alignment, and video recognition alignment can also be considered.



## References

- [1]. Hu Nannan. "Design and Esearch Of Electric Walking Tools for The Elderly". M.Eng. Master's Degree Thesis of Hebei University of Technology, China, 2015.
- [2]. Muhammad Amjad, Muhammad Farooq-i-Azam, et al. "Wireless Charging Systems for Electric Vehicles". **Renewable and Sustainable Energy Reviews**, Vol 167, October 2022. <https://doi.org/10.1016/j.rser.2022.112730>.
- [3]. André Kurs, Aristeidis Karalis, Robert Moffatt, et al. "Wireless Power Transfer Via Strongly Coupled Magnetic Resonances". **Science**, 2007, Vol 317 Issue 5834, pp83-86. <https://doi.org/10.1126/science.1143254>.
- [4]. Biao Hu, Hao Li, et al. "A Long-Distance High-Power Microwave Wireless Power Transmission System Based on Asymmetrical Resonant Magnetron and Cyclotron-Wave Rectifier". **Energy Reports**, Vol 7, November 2021, pp 1154-1161. <https://doi.org/10.1016/j.egy.2020.12.026>.
- [5]. Ji-Xiang Wang, Yun-Ze Li, et al. "Investigation of A Gravity-Immune Chip-Level Spray Cooling for Thermal Protection of Laser-Based Wireless Power Transmission System". **International Journal of Heat and Mass Transfer**. Vol 114, November 2017, pp 715-726. <https://doi.org/10.1016/j.ijheatmasstransfer.2017.06.111>.
- [6]. Yuvrajsinh Rathod, Larry Hughes. "Simulating the Charging of Electric Vehicles by Laser". **Procedia Computer Science**, Vol 155, 2019, Pp 527-534. <https://doi.org/10.1016/j.procs.2019.08.073>.
- [7]. Jiajie Chen, Jin Xu. "A New Coil Structure for Implantable Wireless Charging System" **Biomedical Signal Processing and Control**, Vol 68, July 2021. <https://doi.org/10.1016/j.bspc.2021.102693>.
- [8]. Luo Yanting. "Research on Efficiency Optimization Method and Key Technology of Magnetically Coupled Resonant Wireless Power Transfer System" Ph.D. Thesis of National University of Defense Technology, China, 2018.
- [9]. Matjaz Rozman, Augustine Ikpehai, et al. "Smart Wireless Power Transmission System for Autonomous EV Charging", **IEEE Access**, Volume 7, 2019. <https://doi.org/10.1109/ACCESS.2019.2912931>.
- [10]. Lionel Pichon. "Electromagnetic Analysis and Simulation Aspects of Wireless Power Transfer in The Domain of Inductive Power Transmission Technology".

This material is reserved for educational use only, not allowed for commercial use.

Forbidden to modify the content, and cite the document when use.

- Journal of Electromagnetic Waves and Applications**, 2020, vol. 34, no. 13, pp 1719 – 1755 [HTTPS://DOI.ORG/10.1080/09205071.2020.1799870](https://doi.org/10.1080/09205071.2020.1799870).
- [11].Rui Feng, Nina Roscoe, et al. "Magnetic Field Distribution in a WPT System for Electric Vehicle Charging". **Progress In Electromagnetic Research Symposium (PIERS)**, Shanghai, China, 8-11th August 2016, [HTTPS://DOI.ORG/10.1109/PIERS.2016.7735864](https://doi.org/10.1109/PIERS.2016.7735864)
- [12].Yang Yang, Jinlong Cui, et al. "Design and Analysis of Magnetic Coils for Optimizing the Coupling Coefficient in an Electric Vehicle Wireless Power Transfer System". **Energies**. 2020, vol 13. [HTTPS://DOI.ORG/10.3390/en13164143](https://doi.org/10.3390/en13164143).
- [13].Kafeel Ahmed Kalwar, Saad Mekhilef, et al. "Coil Design for High Misalignment Tolerant Inductive Power Transfer System for EV Charging". **Energies**. 2016, vol 9. [HTTPS://DOI.ORG/10.3390/en9110937](https://doi.org/10.3390/en9110937).
- [14].Sangwook Park. "Evaluation of Electromagnetic Exposure During 85 kHz Wireless Power Transfer for Electric Vehicles". **IEEE Transactions on Magnetics**, vol. 54, No. 1, January 2018. [HTTPS://DOI.ORG/10.1109/tmag.2017.2748498](https://doi.org/10.1109/tmag.2017.2748498).
- [15].Haris Gulzar, Noor ul Ain, Talha Zahid, et al. "A Comprehensive Electromagnetic Design, Simulation and Analysis of Wireless Charging Coils for Large Power Applications". **Progress in Electromagnetics Research Symposium (PIERS - Toyama)**, Japan, 1–4th August, 2018. [HTTPS://DOI.ORG/10.23919/PIERS.2018.8598241](https://doi.org/10.23919/PIERS.2018.8598241).
- [16].Rupesh Kumar Jha, et al. "Performance Comparison of the One-Element Resonant EV Wireless Battery Chargers". **IEEE Transactions on Industry Applications**, Vol.54 No.4 May/June 2018. <https://doi.org/10.1109/TIA.2018.2796058>.
- [17].Ihssen Jabri, Adel Bouallegue, Fethi Ghodbane, "Misalignment Controller in Wireless Battery Charger for Electric Vehicle Based on MPPT Method and Metaheuristic Algorithm". **Wireless Netw**, 2018, vol. 24, pp. 2375–2396, <https://doi.org/10.1007/s11276-017-1474-5>.
- [18].Winges J., Rylander T., Petersson C., et al. "Multi-Objective Optimization of Wireless Power Transfer Systems with Magnetically Coupled Resonators and Nonlinear Loads". **Progress in Electromagnetics Research**, 2019, vol 83, pp. 25-42. <https://doi.org/10.2528/PIERB18111507>

- [19].Autohome Inc. "SAIC-GM-Wuling, Baojun E100 Parameter Configuration" [Online] <https://car.autohome.com.cn/config/series/3993-14494.html>. (accessed on December 26, 2023).
- [20].Yu Zhisheng, Xia Qunsheng. **Automobile Theory**. China Machinery Industry Press. ISBN:9787111602392. 2019.
- [21].Huang Chaosheng. "Research on Vertical Step Passability of Wheeled Vehicle". **China Mechanical Engineering**, 2015, vol 26. <https://doi.org/10.3969/j.issn.1004-132X.2015.09.023>
- [22].Ministry of Housing and Urban-Rural Development of the People's Republic of China. **Chinese code for design of urban road engineering**, [Online]. [https://www.mohurd.gov.cn/gongkai/zhengce/zhengcefilelib/201808/20180824\\_237283.html](https://www.mohurd.gov.cn/gongkai/zhengce/zhengcefilelib/201808/20180824_237283.html). 2018.
- [23].Shang Lun. "Popular Passenger Car and Light Truck Tires in The United States". **Chinese Journal of Rubber Technology Market**, 2012, vol 10, no. 4. pp. 58-58 <https://doi.org/10.3969/j.issn.1672-125X.2012.04.043>.
- [24].Minghua Zheng, Heng Zhou and Jingtang Zheng, "Pure Electric Vehicle Power System Matching Design and Simulation". **Journal of Physics: Conference Series**. Volume 2418, September 25th, 2022. <https://doi.org/10.1088/1742-6596/2418/1/012050>.
- [25].Liu Xinlei, Cheng Zengmu. "Research on Pure Electric Vehicle Battery Technology Match", **Chinese journal of power sources**, 2018, vol 42 c-3, pp 367-368,376. <https://doi.org/10.3969/j.issn.1002-087X.2018.03.015>.
- [26].Miller J M, Jones P T, Li J M, et al. "ORNL Experience and Challenges Facing Dynamic Wireless Power Charging of EV's". **IEEE Circuits & Systems Magazine**, 2015, vol. 15, C-2, pp 40-53. <https://doi.org/10.1109/MCAS.2015.2419012>.
- [27].Tan Juhua, Li Xiaofang, Guo Xiaochun. "Design and Optimization Analysis of Wireless Charging Coil for Magnetically Coupled Resonance Electric Vehicle". **Journal of Shenyang University of Technology**, China. Jan. 2020, vol 42, no. 1. pp 84-89. <https://doi.org/10.7688/j.issn.1000-1646.2020.01.16>.
- [28].Liu Tao. "Circuit Research of Magnetically Coupled Resonance Wireless Charging System for Electric Vehicle". M.Eng. Master's Degree Thesis of Southwest University of Science and Technology, China. May 2021.

- [29].L Zhai, G Zhong, et al. "Research on Magnetic Field Distribution and Characteristics of a 3.7 kW Wireless Charging System for Electric Vehicles under Offset". **Energies**, 2019, vol. 12, issue 3, pp. 1-21. [HTTPS://DOI.ORG/10.3390/en12030392](https://doi.org/10.3390/en12030392).
- [30].I.S. Grant, W.R. Phillips. **Electromagnetism** (2nd Edition). Published by John Wiley. August 1991. ISBN: 978-0-471-92712-9.
- [31].USA Society of Automotive Engineers. "**Wireless Power Transfer for Light-Duty Plug-In/ Electric Vehicles and Alignment Methodology**". J2954\_201605. Issued 2016-05. [Online]. [https://www.sae.org/standards/content/j2954\\_201605/](https://www.sae.org/standards/content/j2954_201605/). (accessed on December 28, 2023).
- [32].Kuang Xiangjun, "Calculation of Space Magnetic Field for Any Quadrilateral Current-Carrying Coil". **China Journal of College Physics**, Vol.36, No.4, Apr. 2017. <https://doi.org/10.16854/j.cnki.1000-0712.2017.04.007>.
- [33].Yang Defu, Song Bei, Wang Yuqing, "Analysis of Problems in Measuring Air Permeability". **China Journal of Yanan University**, Sept.2005. vol. 24, C-3. Pp 43-44. <https://doi.org/10.3969/j.issn.1004-602X.2005.03.017>.
- [34].Xu, P. Fu, C. Li, J.-J. Dong, L. Zhao, S.-P. "The Research of Estimating the Location of Radioactive Sources Using the Bayesian Estimation". **Nuclear Instruments and Methods in Physics Research Section A: Accelerators, Spectrometers, Detectors and Associated Equipment**. August 2021, vol. 1006. <https://doi.org/10.1016/j.nima.2021.165405>.
- [35].Ma, D. Mao, W. Tan, W. Gao, J. Zhang, Z. Xie, Y. "Emission Source Tracing Based on Bionic Algorithm Mobile Sensors with Artificial Olfactory System". **Robotica**, 2022, vol. 40, pp. 976--996. <https://doi.org/10.1017/S0263574721000904>.
- [36].Serra, M. Sathe, P. Rypina, I. Kirincich, A. Ross, S.D. Lermusiaux, P. "Search and Rescue at Sea Aided by Hidden Flow Structures". **Nature Communications**. 2020, vol. 11, 2525. <https://www.nature.com/articles/s41467-020-16281-x>.
- [37].Li, S. Chen, H. Wang, M. Heidari, A.A. Mirjalili, S. "Slime Mould Algorithm: A New Method for Stochastic Optimization". **Future Generation Computer Systems**. 2020, vol. 111, pp. 300--323. <https://doi.org/10.1016/j.future.2020.03.055>.
- [38].Xue, J. Shen, B. "A Novel Swarm Intelligence Optimization Approach: Sparrow Search Algorithm". **Systems Science & Control Engineering**, Volume 8, 2020 - Issue 1, pp. 22--34. <https://doi.org/10.1080/21642583.2019.1708830>.

- [39].Zervoudakis, K. Tsafarakis, S. "A Mayfly Optimization Algorithm". **Computers & Industrial Engineering**, 2020, vol. 145. <https://doi.org/10.1016/j.cie.2020.106559>.
- [40].Arora, S. Singh, S. "Butterfly Optimization Algorithm: A Novel Approach for Global Optimization". **Soft Computing**. 2019, vol. 23, pp. 715--734. <https://doi.org/10.1007/s00500-018-3102-4>.
- [41].Feng, Y. Deb, S. Wang, G.G. Alavi, A.H. "Monarch Butterfly Optimization: A Comprehensive Review". **Expert Systems with Applications**. Vol. 168, 15 April 2021. <https://doi.org/10.1016/j.eswa.2020.114418>.
- [42].Peña-Delgado, A.F. Peraza-Vázquez, H. et al. "A Novel Bio-Inspired Algorithm Applied to Selective Harmonic Elimination in a Three-Phase Eleven-Level Inverter". **Mathematical Problems in Engineering**. Dec 2020, pp. 1--10. <https://doi.org/10.1155/2020/8856040>.
- [43].Lin, Z. Yue, M. Chen, G. Sun, J. "Path Planning of Mobile Robot With PSO-Based APF And Fuzzy-Based DWA Subject to Moving Obstacles". **Transactions of the Institute of Measurement and Control**. 2022, vol. 44, no. 1, pp. 121-132. <https://doi.org/10.1177/01423312211024798>.
- [44].Song, B. Wang, Z. Zou, L. "An Improved PSO Algorithm for Smooth Path Planning of Mobile Robots Using Continuous High-Degree Bezier Curve". **Applied Soft Computing**. 2021, vol. 100, 106960. <https://doi.org/10.1016/j.asoc.2020.106960>.
- [45].Li, X. Wu, D. "An Improved Method of Particle Swarm Optimization for Path Planning of Mobile Robot". **Journal of Control Science and Engineering**. 25th May 2020, pp. 1--12. <https://doi.org/10.1155/2020/3857894>.
- [46].Hu Liu, Zikun Chen, Yongliang Tian, Bin Wang, Hao Yang, Guanghui Wu. "Evaluation Method for Helicopter Maritime Search and Rescue Response Plan with Uncertainty". **Chinese Journal of Aeronautics**. April 2021, vol 34, Issue 4, Pp. 493-507. <https://doi.org/10.1016/j.cja.2020.07.008>.
- [47].Jamil, M. Yang, X.S. Zepernick, H. J. "8-Test Functions for Global Optimization: A Comprehensive Survey". **Swarm Intelligence and Bio-Inspired Computation**, 2013, pp. 193--222. <https://doi.org/10.1016/B978-0-12-405163-8.00008-9>.
- [48].Marcin Molga, Czesaw Smutnicki. "Test Functions for Optimization Needs". [Online]. <https://robertmarks.org/Classes/ENGR5358/Papers/functions.pdf>. (accessed on Jan. 20, 2024). 2005.

- [49].Locatelli, M. "A Note on the Griewank Test Function". **Journal of Global Optimization**. 2003, vol. 25, pp. 169–174.  
<https://doi.org/10.1023/A:1021956306041>.
- [50].Surjanovic, S. Bingham, D. "Virtual Library of Simulation Experiments: Test Functions and Datasets". Canada Simon Fraser University. [Online]. Available: <http://www.sfu.ca/~ssurjano> (accessed on 15 November 2023).
- [51].Giovanni Acampora, Roberto Schiattarella, Autilia Vitiello. "Using Quantum Amplitude Amplification in Genetic Algorithms". **Expert Systems with Applications**, 2022, vol. 209, 118203. <https://doi.org/10.1016/j.eswa.2022.118203>.
- [52].Goldberg, D.E. **Genetic Algorithms in Search, Optimization and Machine Learning**; Addison-Wesley Professional: Boston, MA, USA, 1989. ISBN-13: 978-0-201-15767-3.
- [53].Darwin, C. **The Origin of Species**, 1st ed. Prakash Books India Pvt Ltd, New Delhi, India, 2013. ISBN: 13 978-8172344887.
- [54].Zhong, R.Y. Xu, X. "Intelligent Manufacturing in the Context of Industry 4.0: A Review". **Engineering**, October 2017, Vol. 3, Issue 5, Pp. 616-630.  
<https://doi.org/10.1016/J.ENG.2017.05.015>.
- [55].Chen Chen, Huang Xueliang, Tan Linlin, et al. "Electromagnetic Environment and Security Evaluation for Wireless Charging of Electric Vehicles". **Transactions of China Electrotechnical Society**, Oct. 2015, Vol. 30, No. 19.  
<https://doi.org/10.19595/j.cnki.1000-6753.tces.2015.19.010>.

## Related Publications

1. Junlong ZHENG. Chaiyan JETTANASEN. Analysis Of Mutual Inductance Between Transmitter And Receiver Coils In Wireless Power Transfer System Of Electric Vehicle. Advances in Electrical And Electronic Engineering (ISSN 1804-3119). Sept. 2023. <https://doi.org/10.15598/aeer.v21i3.4991>

(The main content of this paper comes from the third chapter of this thesis)

2. Junlong Zheng, Chaiyan Jettanasen and Pathomthat Chiradeja, Performance and Application Analysis of a New Optimization Algorithm. Computation, (ISSN: 2079-3197), December 2023, <https://doi.org/10.3390/computation12010001>

(The main content of this paper comes from Chapter 4 of this thesis)

The following two pictures are the screenshots from the first page of the two papers.



# ANALYSIS OF MUTUAL INDUCTANCE BETWEEN TRANSMITTER AND RECEIVER COILS IN WIRELESS POWER TRANSFER SYSTEM OF ELECTRIC VEHICLE

Junlong ZHENG<sup>1,2</sup> , Chaiyan JETTANASEN<sup>1</sup> 

<sup>1</sup>School of Engineering, King Mongkut's Institute of Technology Ladkrabang, Bangkok 10520, Thailand;

<sup>2</sup> Guangxi Electrical Polytechnic Institute, Nanning, Guangxi, China;

long8889@126.com, chaiyan.je@kmitl.ac.th

DOI: 10.15598/aece.v21i3.4991

Article history: Received Dec 24, 2022; Revised Mar 20, 2023; Accepted Sep 08, 2023; Published Sep 30, 2023.  
This is an open access article under the BY-CC license.

**Abstract.** In the electric vehicle wireless power transfer (WPT) system, the mutual inductance ( $M$ ) between the transmitting and receiving coils is an important factor influencing overall system efficiency. The  $M$  is affected by various factors such as the physical structure of the coils diagram, the distance and relative position between the transmitting and receiving coils, and so on. Our work here has two outstanding contributions. First, the detailed mathematical model of the  $M$  was developed. Second, the three-dimensional spatial distribution diagram of the  $M$  was drawn using Python software, the maximum value of the  $M$  and its corresponding position coordinates were calculated. Then, the theoretical analysis of the  $M$  distribution was proven correct through experiments. The theoretical analysis and experimental verification of the  $M$  distribution provided a theoretical reference for the positioning requirements between the transmitting and receiving coils in the electric vehicle WPT system.

## Keywords

Electric vehicle, Wireless power transfer; Magnetic field, Mutual inductance.

## 1. Introduction

The wireless charging technology for electric vehicles transmits electric energy in the form of high-frequency alternating magnetic energy to the electric energy pickup mechanism at the receiving end via the electric energy transmitting coil, and then supplies power

to the on-board energy storage equipment; wherein the power transmitting coil is buried under the ground or installed on the ground; and the electric energy pickup mechanism at the receiving end is installed on the automobile chassis.

Magnetic coupling resonance wireless power transmission system (abbreviated as MCR-WPT) is the most prevalent type of electric vehicle wireless charging technology. The overall system composition is depicted in Fig.1-1. The system is made up of a rectifier filter circuit. ①, high-frequency inverter circuit ②, drive circuit, sampling circuit, resonant capacitors C1 C2, transmitting coil L1, receiving coil L2, high-frequency rectifier circuit ④ and load circuit ⑤. Among these, the 220V mains power input rectifier filter circuit ① generates direct current  $U_i$   $I_i$ , which is then delivered to the high-frequency inverter circuit ② to generate a specified frequency of AC power. The frequency of this alternating current power can be regulated by the driving circuit; this AC power is given to the resonant circuit module ③, allowing for wireless transfer of electrical energy. Module ③ is made up of two LC resonant circuits, L1 and L2, as well as corresponding resonant capacitors C1 and C2 [1].

The MCR-WPT's energy transmission performance is largely dependent on the position connection between the emitter and receiver coils, according to its working principle [3]. The primary focus of MCR-WPT system research, as well as the major factor that directly effects MCR-WPT system use and promotion, is how to ensure the successful transmission of electric energy in MCR-WPT system.

Article

# Performance and Application Analysis of a New Optimization Algorithm

 Junlong Zheng <sup>1,2,†</sup>, Chaiyan Jettanasen <sup>1,†</sup> and Pathomthat Chiradeja <sup>3,\*,†</sup>
<sup>1</sup> Department of Electrical Engineering, School of Engineering, King Mongkut's Institute of Technology Ladkrabang, Bangkok 10520, Thailand; 63601014@kmitl.ac.th (J.Z.); chaiyan.je@kmitl.ac.th (C.J.)

<sup>2</sup> Guangxi Electrical Polytechnic Institute, Nanning 530007, China

<sup>3</sup> Faculty of Engineering, Srinakharinwirot University, Bangkok 10110, Thailand

\* Correspondence: chiradeja@hotmail.com; Tel.: +66-2329-8330

† These authors contributed equally to this work.

**Abstract:** Our research focused on an optimization algorithm. Our work makes three contributions. First, a new optimization algorithm, the Maritime Search and Rescue Algorithm (MSRA), is creatively proposed. The algorithm not only has better optimization performance, but also has the ability to plan the path to the best site. For other existing intelligent optimization algorithms, it has never been found that they have both of these performances. Second, the mathematical model of the MSRA was established, and the computer program pseudo-code was created. Third, the MSRA was verified by experiments.

**Keywords:** maritime search and rescue; mutual inductance; optimization algorithm; test function

## 1. Introduction

Among the actual social production projects, some have a common trait: they not only need to solve the location of the optimal point, but also need to plan the optimal route, make the optimal decision, and so on. Examples of these projects include searching for the location of the maximum magnetic mutual inductance in a three-dimensional magnetic field [1] (Project 1), searching for the location of radioactive sources in three-dimensional space [2], searching for the location of the leakage of hazardous chemicals and toxic volatile substances [3], sea surface search and rescue [4], etc. The equipment in the optimization project is what is explained here, such as the search and rescue helicopter [4] in the sea search and rescue project and the handle-held detector [2] in searching for the location of radioactive sources. To increase labor productivity, this kind of optimization project needs the right optimization method. Numerous optimization techniques are currently in use, including the SMA [5], the sparrow search algorithm [6], and others.

As seen in Figure 1, this was a simulation experiment in which we applied the SMA to Project 1 on a computer. The chaotic curves in the picture are the moving paths taken by the receiving coil. The number of individuals in the population was defined as 20 and the number of cycles as 100. The calculation process created a total of 2020 population members, meaning that there were a total of 2020 iterations. The error value of the computation result was  $8.33 \times 10^{-175}$ . The graphic shows that the route design was disorganized. There were a total of 2020 probe position points. Every two adjacent points in time formed a section of the route, and the total route formed many circuitous paths. The majority of intelligent algorithms, like the SMA, are to blame for this. A population made up of dozens of people is defined at the beginning of each algorithm, such as the Mayfly Algorithm [7], the Butterfly Optimization Algorithm [8], the Monarch Butterfly Optimization Algorithm [9], the sparrow search algorithm [6], the Black Widow Optimization Algorithm [10], and so on. Each person in the population represents a random search location point. A batch of the population is created during each iteration. The requirements can be met even though these



Citation: Zheng, J.; Jettanasen, C.; Chiradeja, P. Performance and Application Analysis of a New Optimization Algorithm. *Computation* **2024**, *12*, 1. <https://doi.org/10.3390/computation12010001>

Academic Editor: Demos T. Tsahalis

Received: 20 November 2023

Revised: 11 December 2023

Accepted: 12 December 2023

Published: 20 December 2023



**Copyright:** © 2023 by the authors. Licensee MDPI, Basel, Switzerland. This article is an open access article distributed under the terms and conditions of the Creative Commons Attribution (CC BY) license (<https://creativecommons.org/licenses/by/4.0/>).

## AUTHOR BIOGRAPHY AND PROCEDURES FOR THESIS WRITING

Name Mr. Zheng Junlong

Date of Birth Dec 12, 1978, in GuangXi of China

Address: Guangxi Electrical Polytechnic Institute, Nanning 530007, Guangxi, China.

Educational Background:

2002: Bachelor's Degree Thermal Engineering, Guangxi University. Nanning, Guangxi, China.

2010: Master's degree in Power Systems and Automation, Guangxi University. Nanning, Guangxi, China.

Work Experience:

2011 – 2024 Guangxi Electrical Polytechnic Institute.

